UNIVERSIDAD
DE MÁLAGA

Dpto. Lenguajes y Ciencias de la Computación

Tesis Doctoral

EXPERIMENTAL MEASUREMENT SYSTEM AND NEURAL NETWORK MODEL TO SIMULATE PHOTOVOLTAIC MODULES

Autor:
Michel Piliougine Rocha

Directora:
Llanos Mora López

2011

AUTOR: Michel Piliougine Rocha

http://orcid.org/0000-0002-8169-9727

EDITA: Publicaciones y Divulgación Científica. Universidad de Málaga

La Dra. Llanos Mora López, Titular de Universidad en el Departamento de Lenguajes y Ciencias de la Computación de la Universidad de Málaga

Certifica

Que Michel Piliougine Rocha, Ingeniero en Informática, ha realizado bajo su dirección la tesis doctoral titulada EXPERIMENTAL MEASUREMENT SYSTEM AND NEURAL NETWORK MODEL TO SIMULATE PHOTOVOLTAIC MODULES, que se recoge en la presente memoria, cumpliendo todos los requisitos legales para optar al grado de Doctor, por lo que autoriza su lectura y defensa pública.

Y para que así conste y tenga los efectos oportunos, firmo este certificado en

Málaga, a 28 de julio de 2011

Dra. Llanos Mora López

A mi abuela, Isabel Salas Fernández ...

Este trabajo de investigación ha sido financiado por el "Ministerio de Ciencia e Innovación" del Gobierno de España (proyecto No. ENE07–67248) y por la "Junta de Andalucía" (proyecto No. P07–RNM–02504).

This research work was funded by the Spanish "Ministerio de Ciencia e Innovación" (grant No. ENE07–67248) and the "Junta de Andalucía" (grant No. P07–RNM–02504).

Agradecimientos

A Llanos Mora López, directora de esta tesis doctoral, por sus explicaciones, indicaciones y directrices, que constituyen el esqueleto físico sobre el que se sustenta todo el trabajo realizado. También quiero agradecer toda la ayuda que me han ofrecido Mariano Sidrach de Cardona, Jesús Carretero y David Elizondo. Sin ellos no hubiera sido posible la realización de este trabajo.

También merecen una mención especial todos los compañeros del laboratorio que me han apoyado moralmente durante estos años, en especial Antonio, Pedrillo, José Carlos y Pepe Zorrilla. También quiero saludar desde estas líneas a amigos como Javier Guijarro, Juan Romero, Sergio Recio, Reme Partal y muchos otros.

Finalmente el mayor de todos los agradecimientos es para mi madre, para mi hermano Óscar y para mi padre.

Contents

List of Figures

List of Tables

Chapter 1

Introduction

1.1 A brief survey on PV technology

The number of photovoltaic solar plants has increased significantly in recent years, mainly due to the following factors: the need to use energy sources that contribute to reducing carbon emissions, the establishment of support policies to introduce this technology, the improvement of the efficiency and the significant reduction in the price of all the components that make up those systems.

The use of photovoltaic energy for large–scale power generation began in the late 1980s. The solar photovoltaic market has been growing at an average rate of 35 % annually from 1998. In 2010, 15000 MW were installed so that the global photovoltaic capacity later that year was approximately 40000 MW. This high growth has resulted in a significant and continuing decline in prices, so this technology will become competitive in some countries by 2015. This growth is particularly important in Europe and represents 70 % of the global market. The large plants are important for the future development of photovoltaic generation as they involve an up–scaling in power and require strong quality control, which attract the interest of the electricity utilities.

An important factor that is helping to establish energy policies to support photovoltaic solar systems is that this type of energy prevents the emission of billions of tons of CO_2 into the atmosphere. It would reduce CO_2 emissions by substituting of fossil fuels, creating jobs and increasing the security of energy supplies.

The key needs for the future are to raise confidence in the use of photovoltaic for power generation and to cut cost. Scaling–up the levels of photovoltaic use and promoting R&D are important to achieve these goals.

Photovoltaic systems are based on the use of cells that convert sunlight

directly into the electricity. Photovoltaic cells are formed by layers of semiconductor materials. They can be classified according to the technology used in cells of first, second and third generation. The first generation technologies include cells based on mono and polycrystalline silicon; the second generation includes the thin–film cells and third-generation includes concentration cells, organic cells and other new technologies in experimental phase.

The photovoltaic market has traditionally been dominated by silicon cell technologies and in fact virtually all production was from these technologies until 2006. In 2008 thin–film technologies started to emerge strongly in the market. According to the latest report of the European Photovoltaic Industry Association [1], the 40 % of world production is expected to be developed using these new module technologies by 2020, as shown in Figure 1.1.

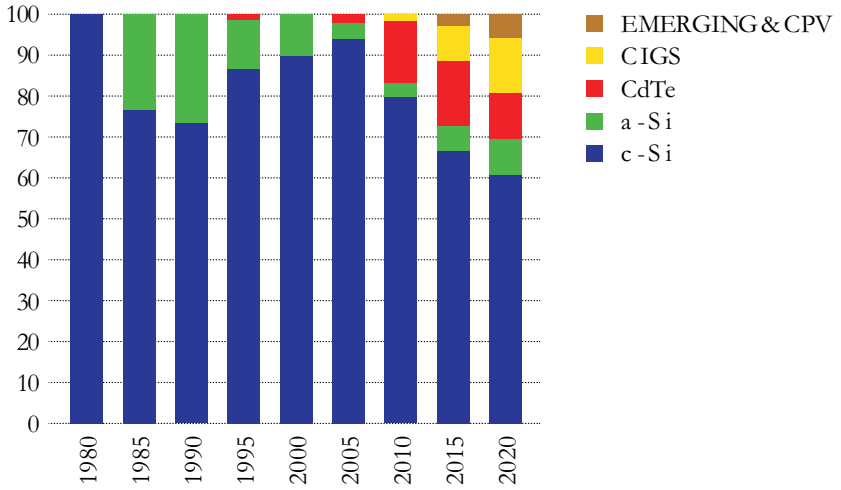

Figure 1.1: Historical development of the photovoltaic technology market and expected future trends

Thin–film cells are a reality in the photovoltaic market among the new emerging technologies. These cells are basically the deposition of thin films of semiconductor materials on various substrates, usually glass, but also on other flexible media. The four commercial types of these cells are:

- Amorphous Silicon
- Cadmium Telluride (CdTe)
- Copper Indium Gallium Selenide (CIGS) and Copper Indium Selenide (CIS)
- Multi–junction thin–film Silicon

The appearance on the market of these new module technologies means that researchers face the challenge of establishing their electrical characteristics and their variability under different meteorological parameters. The difficulty to accurately predict the energy produced by a photovoltaic system in different climatic conditions is one of the most important unresolved issues.

Manufacturers, designers, installers, and investors in photovoltaic systems require a reliable prediction of solar electricity production of these systems. The difficulty to predict the energy produced by a photovoltaic system is that manufacturers express the output power of a module in standard conditions, which are different from the actual module operating conditions. This difficulty is increased with the emergence of new and different technologies of photovoltaic modules on the market. Solving this problem will contribute to:

- More accurately predicting the energy that these systems will produce over their lifetime, which is of great importance when evaluating profitability.
- Comparing the efficiency of systems with different module technologies, depending on meteorological parameters.
- The development of models for short–term prediction of the energy produced by these systems. This is of great importance when developing large power plants connected to the grid. The integration of these systems into the conventional grid requires knowing in advance how much electricity will be generated.

Nowadays, the energy produced by a photovoltaic system is calculated using the system's efficiency, performance ratio (PR) and Yield (kWh/kWp). Various loss factors must be taken into account in this calculation. Solar radiation and temperature values are used as input data for these estimations.

The different proposals [2] are based on statistical models (measure–correlate–predict) using parameters previously obtained in the laboratory. Some authors use physical models to study the influence of temperature on the behaviour of the module. These methods estimate the annual energy produced by a photovoltaic system with an error of about 10 %.

This error can be reduced by analyzing and considering the electrical characteristics of the modules and their dependence on climatic parameters. The accuracy and usefulness of the characterization of the maximum power of PV modules under standard conditions of measurement is beginning to be questioned, [3]. Only the maximum power does not allow the evaluation

and comparison of the production of solar electricity under different climatic conditions.

The Joint Research Centre of the European Commission in Ispra (Italy) has proposed a methodology for crystalline silicon, based on the determination of three–dimensional diagrams which represent the maximum output of a module (as a percentage of its maximum power at standard condition) depending on the incident irradiance and global temperature. Combining this information with histograms of the incident global irradiance and air temperature of the enclave of the future installation, a prediction of the energy performance for the photovoltaic generator can be estimated, [4]. The application of this methodology (energy rating) on new technologies is yet to be satisfactorily resolved.

As for the aforementioned electrical characterization in standard conditions performed by laboratories, the following disadvantages should be mentioned:

- Some dependency on measurements of the solar simulator used.
- The expensive test and measurement instrumentation required for this characterization is out of the reach of many laboratories and research centres.
- The aging problem posed by solar simulators.
- Difficult to simulate the real solar spectrum.

The international comparison of the calibration results within cells and modules undertaken by the PEP initiative (Photovoltaic Solar Energy Project) in 1985, 1987, 1989 and 1993, [5], [6], shows with very different results among different laboratories. More recently, there have been efforts to characterize the electrical behaviour of photovoltaic modules to real sun.

The Solar Energy Institute (Madrid, Spain) has successfully proposed to carry out, in the line with the measurements performed, similar tests on a primary standard module characterized by an approved laboratory, [7]. These new measurements will correct both the influence of the spectral composition of irradiance and the possible uncertainty in the measurement of cell temperature. In this sense, some authors have made a recent contribution that allows the uncertainty associated with the electrical parameters to be estimated, [8]. The extension of this technique to both CIS modules and those based on HIT cells and EFG has not yet explored.

Additionally, the characterization of photovoltaic generators under standard conditions is not satisfactorily resolved yet. After solving the problem

of determining the power of a module under standard conditions, the next step is to determine the maximum power point for specific climatic conditions. Recent published work suggests that it is necessary to quantify the effect of the incident radiation spectrum in the energy of the modules, [9], [10].

De Soto et al. [11] has proposed a new methodology that takes into account the influence of the radiation spectrum and its angle of incidence in the power modules. One way to deal with this problem is by developing of physical models that simulate the optical and thermal performance of solar cells, and therefore the modules. So, the light absorption spectrum can be measured taking into account the angle of incidence and the different module materials: glass, encapsulant, surface texture and antireflective coatings. These models so far have been used for the design of concentration, where the lens plays a critical role. Such tools are of special importance to explain the influence of the solar spectrum in its electrical behaviour. This may be particularly important in the case of thin–film cells.

The different spectral response of these type of cells, their stability against irradiance and temperature, the determination of their performance under different conditions of operation and the energy that will be produced over their useful life, are aspects that should be studied.

Photovoltaic laboratories are provided with different equipment to measure the electrical characteristic curve of modules that contribute to this type of study. Reference laboratories in Spain are the Photovoltaic Laboratory of the Centre for Energy Environment and Technology (CIEMAT) in Madrid and the National Renewable Energy Centre (CENER) in Navarra.

At these centres, the electrical characterization of modules is performed in two ways, using a solar simulator or by measurements under real sun. The measurements using the solar simulator have the advantage of the measurements being easy to repeat. However the parameters obtained cannot be related with changing weather conditions; moreover, the spectrum of the lamp is not exactly equal to the solar spectrum. As a result, the different spectral response of the module can lead to significant errors.

Outdoor measurements are increasingly used for electrical characterization of photovoltaic modules as they allow measuring to take place under different climatic conditions and the behaviour of modules under real operating conditions to be determined. The results also enable models to be constructed, different technologies to be compared and the results extrapolated to other climatic conditions. The drawback to the outdoor measurements is that equipment capable of measuring all the I–V curve in a short period of time is necessary, so that the climatic conditions for all points of the curve are identical.

A recent addition to the measurement system is the possibility of acquiring the spectrum of the incident solar radiation. This measurement facilitates the interpretation of previous results and enables the influence of the spectrum in the behaviour of the modules to be quantified. This influence is more important in thin–film modules. In any case, the knowledge of the spectrum of the incident radiation allows better methods to be proposed for extrapolating results to different climatic conditions with any type of technology.

1.2 Objectives of this thesis

This thesis seeks to provide researchers and workers in the field of photovoltaic solar energy with the tools and models to characterize and simulate photovoltaic modules. To this end, this thesis puts forward two proposals. The first one is related to measuring these devices and the second one considers their simulation.

As far as the first objective is concerned, a new system and methodology for measuring the I–V curve for photovoltaic modules has been developed. This curve is necessary to accurately establish the electrical parameters of a photovoltaic device. This measurement provides highly relevant information for the design, installation and maintenance of photovoltaic systems. The proposed methodology likewise enables the outdoor measurement of such devices. Indoor testing is usually used to measure the electrical parameters of photovoltaic modules. However, outdoor testing offers significant advantages, such as no expensive artificial light sources being required, there is no limitation on the size of the samples and the illumination of the samples is more homogeneous.

Moreover, we define a standard to format the recorded data when measuring photovoltaic devices, including cells, modules and arrays, in order to contributing to the defining of a unified and accepted methodology that facilitates the *communication* among different laboratories and enterprises. The technology that can be used for accessing and processing the stored data is also presented. This could be very useful for allowing the exchange of data among different agents interested in this type of measuring, that is: manufacturers, laboratories and researchers, among others. The goal is to define a file format to easily interchange I–V curve data.

With regard to the second objective of the thesis, a methodology based on artificial neural networks is proposed as an alternative to algebraic and numerical procedures in order to determine the I–V curve of a module under different conditions. An important contribution of this thesis compared to other previously used methods is the incorporation of the solar spectrum to

simulate the electrical behaviour of photovoltaic modules. This has been performed by using this measurement as an input to the neural network in order to determine the I–V curve. In addition, a suitable selection of the training set is fundamental in order to obtain an operating model. A pattern selection based on a Kohonen self–organizing map instead a random selection is proposed. Thanks to this previous step, the performance of the network trained using spectral information improves the performance of the network trained without spectral information.

1.3 Thesis structure

The thesis has been divided into five chapters, including this Introduction, and two Appendices.

In Chapter 2 an experimental system to measure the current–voltage characteristic curve of photovoltaic modules is described. The I–V curve provides highly relevant information about the module and allows us to determine its electrical parameters. We start by reviewing and classifying several methods from the literature for measuring I–V curves of photovoltaic devices. We then move on to describe the proposed system as it has been implemented in our photovoltaic laboratory at the University of Malaga.

Basically, a four–quadrant power supply is used to bias the module while two multimeters acquire current and voltage values. These multimeters are synchronized through a signal from a waveform generator to ensure that current and voltage values are acquired simultaneously. These instruments are controlled by a computer using the GPIB standard. The uncertainties in the measurement of the points belonging to the I–V curve are estimated.

The uncertainty in the irradiance and module temperature measurements are also analyzed. The main electrical parameters are calculated with their respective uncertainties. By way of illustration, some I–V curves over a test module are presented. In order to check the accuracy of the proposed experimental system several outdoor measurements have been consecutively carried out under the same irradiance and module temperature and the statistical variability of these measurements is studied. Finally, an example of application of the proposed system is described and its results are presented. It is related to the degradation mechanisms that take place on PV modules after a long–period exposure. The shifting in the electrical parameters has been analysed.

In Chapter 3, a standard is proposed in order to store the recorded data measured from photovoltaic devices with the aim of providing a unified file format facilitating data exchange between different laboratories and re-

searchers. The main objective is to harmonize file outputs of different I–V curve tracer systems but this definition can easily be expanded to address other needs in photovoltaic laboratories.

The idea consists of offering an XML based format to the photovoltaic community with the aim for it to be used in all situations where an I–V curve is measured or used to perform calculations over it, such as when translating it to STC conditions or when parameters of a module need to be determined using this measurement data. The proposed format is based on XML, probably the most common language for storing and accessing data. We begin by reviewing other proposed formats which appear in the literature in order to store and accessing recorded data including XML based formats. Even a recent proposal oriented to monitor photovoltaic plants is referenced.

We continue the chapter by summarizing the most relevant features of XML and the different ways of defining an XML file format: DTDs and XSD. Before defining the format, an analysis is performed to determine the data needs, taking into account the different requirements of all users. This data does not only include information about measurements but also the specifications of measured PV devices and even administrative information about the laboratory that performs the tests. Finally, the model implementation is presented. The definition of the entities to be included is given in the XSD that defines the new XML format. For each entity, its definition is given using a tree as a graphic means to show its possible nested entities.

In Chapter 4 the different calculated parameters necessary for the models proposed in Chapter 5 are presented. Specifically, this chapter sets out the algorithms to calculated variables related with the solar energy that the photovoltaic system will receive, i.e.: solar angles, the air mass factor, the clearness index and the average photon energy. The main solar angles, solar elevation and azimuth, are calculated using the solar position in the celestial sphere. The astronomical relationship between the Sun and the Earth is taken into account in order to determine the solar position.

A review of different methods for solar position estimation is first presented. One of them is selected in order to be implemented. The angle of incidence is then determined and the extraterrestrial irradiance is also estimated. A formulation in order to determine the clearness index is given based on the calculus of the extraterrestrial solar irradiance. A normalization calculus of the clearness index is likewise proposed taking into account a correction using the air mass factor. Finally the average photon energy is presented as an attempt to characterize the spectrum shape using a unique index. In addition, an alternative definition of this index is presented in this thesis in order to extract more information from each measured spectrum splitting the wavelength range into contiguous intervals.

A methodology based on artificial neural networks is proposed in Chapter 5 as an alternative to algebraic and numerical procedures to be found in the literature to determine the I–V curve of a module under different conditions. The main contribution is the incorporation of the spectrum as an input to the neural network to determine the I–V curve. In addition, a suitable selection of the training set is fundamental in order to obtain an operating model.

In this chapter, a pattern selection based on a Kohonen self–organizing map instead a random selection is proposed improving previous results. We start by reviewing the previous methods and continue by studying a few works which try to solve the same problem using artificial neural networks. This is the approach that is selected in this thesis.

First, a representation of the current–voltage curves suitable to train a multilayer perceptron is presented. Two attempts at using the multilayer perceptron are performed. In the first attempt, in addition to irradiance and module temperature, the angle of incidence and the clearness index are used as input parameters to train the network. One hundred samples have been randomly selected from among all the acquired measurements in order to train the network. A detailed curve by curve study is then performed in order to illustrate the behaviour of the proposed model versus a multilayer perceptron trained only using irradiance and module temperature. This study is performed for all measurements and over a selection of clear–sky days.

In the second approach the incorporation of the solar spectral distribution as an input to the multilayer perceptron is considered using a representation of the spectral measurement based on the concept of average photon energy presented in Chapter 4. A classification of the input samples is then performed using a Kohonen self–organizing map. This classification is used in order to select the 100 most representatives samples and we finally use these reduced set of samples in order to train the network. This Kohonen based selection is used to achieve a significantly improvement of the results obtained using only irradiance and module temperature.

Finally, the conclusions of the thesis are presented in Spanish as each chapter has its own conclusions included at the end of each one.

This thesis concludes with two Appendices. In the first one the complete source code corresponding to the XSD Schema which defines the proposed file format in Chapter 3 is listed. A summary of this thesis is presented in Spanish in the second appendix.

Bibliography

[1] *Solar Generation 6 – Solar photovoltaic electricity empowering the world*. European Photovoltaic Industry Association (EPIA) and Greenpeace, 2011.

[2] S.R. Williams, T.R. Betts, R. Gottschalg, D.G. Infield, N.J.C.M. van der Borg, A.R. Burgers, H. de Moor, W. Warta, G. Friesen, D. Chianese, A. Guerin de Montgareuil , T. Zdanowicz, D. Stellbogen, W. Herrmann, S. Pietruzko, J. Krustok, and E. Dunlop. Evaluating of the art of photovoltaic performance modelling in Europe. In *20th European Photovoltaic Solar Energy Conference*, pages 1937–1941, Barcelona (Spain), 2005.

[3] D. Anderson, T. Sample, and E. Dunlop. Obtaining module energy rating from standard laboratory measurements. In *17th European Photovoltaic Solar Energy Conference*, pages 832–835, Munich (Germany), 2001.

[4] R.P. Kenny, E.D. Dunlop, H.A. Ossenbrink, and . Müllejans H. A practical method for the energy rating of c–Si photovoltaic modules based on standard tests. *Progress in Photovoltaics: Research and Applications*, 14(2):155–166, 2006. doi: 10.1002/pip.658.

[5] J. Metzdorf, K. Wittchen, K. Heidler, K. Dehne, R. Shimokawa, F. Nagamine, H. Ossenbrink, L. Fornarini, C. Goodbody, M. Davies, K. Emery, and R. De Blasio. Objectives and results of the PEP'87 round-robin calibration of reference cells and modules. In *21st IEEE Photovoltaic Specialists Conference*, pages 952–959, Kissimmee (FL, USA), 1990. doi: 10.1109/PVSC.1990.111759.

[6] K.A. Emery. Measurement and characterization of solar cells and modules. In A. Luque and S. Hegedus, editors, *Handbook of Photovoltaic Science and Engineering*, chapter 16, pages 701–747. Wiley, New York (NY, USA), 2003. ISBN 978-0-471-49196-5.

[7] E. Caamaño, E. Lorenzo, and R. Zilles. Quality control of wide collections of PV modules: lessons learned from the IES experience. *Progress in Photovoltaics: Research and Applications*, 7(2):137–149, 1999. doi: 10.1002/(SICI)1099-159X(199903/04)7:2<137::AID-PIP249>3.0.CO;2-C.

[8] G. Nofuentes, J. Aguilera, R.L. Santiago, J. de la Casa, and L. Hontoria. A reference–module–based procedure for outdoor estimation of crystalline silicon PV module peak power. *Progress in Photovoltaics: Research and Applications*, 14(1):77–87, 2006. doi: 10.1002/pip.636.

[9] F. Fabero, N. Vela, M. Alonso–Abella, and F. Chenlo. Characterization of recent commercial technologies of PV modules based on outdoor and indoor *I–V* curve measurements. In *20th European Photovoltaic Solar Energy Conference*, pages 2059–2062, Barcelona (Spain), 2005.

[10] Y. Tang, G. TamizhMani, L. Ji, and C. Osterwald. Outdoor energy rating of photovoltaic modules: Module temperature prediction and spectral mismatch analysis. In *20th European Photovoltaic Solar Energy Conference*, pages 2051–2054, Barcelona (Spain), 2005.

[11] W. De Soto, S.A. Klein, and W.A. Beckman. Improvement and validation of a model for photovoltaic array performance. *Solar Energy*, 80 (1):78–88, 2006. doi: 10.1016/j.solener.2005.06.010.

Chapter 2

I–V curve measurement system

2.1 Introduction

The current versus voltage curve of a module provides useful information on its electrical performance. Manufacturing processes usually cause differences in the electrical parameters of different photovoltaic modules, even in cells of the same type. Therefore, only the experimental measurement of the I–V curve allows us to establish the electrical parameters of a photovoltaic device accurately. This measurement provides highly relevant information for the design, installation and maintenance of PV systems. Electrical parameters of photovoltaic modules are usually measured by indoor testing. However, outdoor testing offers significant advantages, such as no expensive artificial light sources being required, there is no limitation on the size of the samples and the illumination of the samples is more homogeneous [1].

In section 2.2, several methods for I–V curve measurement to be found in the literature are reviewed and classified.

Section 2.3 describes an experimental system to measure current–voltage curves of photovoltaic modules under outdoor conditions, designed, built and implemented in our photovoltaic laboratory at the University of Malaga, Spain. A four–quadrant power supply is used to bias the module while two multimeters acquire current and voltage values. Measurements are performed in an automated way by employing commercial instruments controlled by a computer using the GPIB standard.

In section 2.4, the method for synchronizing both multimeters is analyzed. A function generator synchronizes them through their external trigger input and thus ensuring that current and voltage values are acquired simultaneously.

In section 2.5, we analyze the uncertainty in the measurement of the

discrete points belonging to the I–V curve and in the irradiance and module temperature measurements.

In section 2.6, the main electrical parameters are estimated and an analysis of the uncertainties associated with each parameter is included.

In section 2.7, by way of illustration, some curves are performed over a test module to show the functionality of the system. In order to check the accuracy of the proposed experimental system several outdoor measurements were consecutively carried out for the test module under the same irradiance and module temperature and the statistical variability of these measurements is studied.

Finally, an application of the proposed system is presented. It is related with the degradation mechanisms which take place on PV modules after a long–period exposure. The system has been used to measure the characteristic curve of each module. The shifting in the electrical parameters has been analysed.

The chapter concludes with a summary of the most relevant ideas of this system (section 2.9).

2.2 Review of the different methods

In order to characterize photovoltaic devices a procedure to measure I–V curves is required. The basic principle to measure the I–V curve is based on the control of the current supplied by the photovoltaic module between the short circuit point (I_{SC}) and the zero current point (V_{OC}). There are different ways to perform this task and the main methods used are reviewed. Given the large number of methods for I–V measurement, a categorization would be very convenient and useful. The different methods are discussed according to their flexibility, fidelity and cost at the end of this section. A table that summarizes the major characteristics of the methods is also provided.

- Variable resistor.

  The simplest way to measure the I–V curve of a module is to use a variable resistor R as shown in Figure 2.1. The value of R will be varied in steps from zero to infinity in order to capture the points of the I–V curve from short circuit to open circuit, by measuring the voltage and the current in each step. This method is only applicable to low–power modules since higher power resistors are not readily available. Load resistors are not recommended for photovoltaic module characterization as I_{SC} is never exactly reached and the reverse bias characteristics cannot be determined. However, the use of load resistors to evaluate the

performance of a solar module can provide an inexpensive way of approximating its performance and a profitable experiment to introduce students to photovoltaic devices [2].

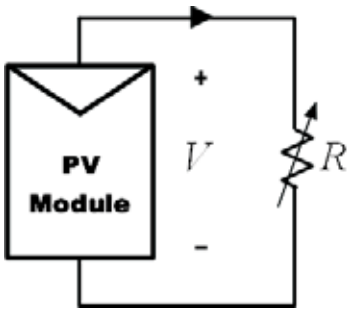

Figure 2.1: Variable resistor scheme

In the study by Malik and Damit [3], the load resistor is increased manually in steps. In each step, the voltage and the current (actually the voltage across a shunt resistor) are sensed using a pair of handed digital multimeters.

According to Mahmoud [4], manually changing the load resistor makes the process very slow, and solar radiation and thermal conditions could therefore be changed during the measurement.

The system presented by Van Dyk et al. [5] employs a set of resistors as load. An array of relays, controlled by a computer card, is used to select the combination of resistors to achieve a specific resistive load. The resistors are chosen to obtain a good spread of points around the *knee* of the curve. Two A/D channels of the computer card are used in order to measure each I–V pair. With this approach, manual operation over the resistor is avoided and the acquisition time is improved.

Muoy et al. [6] and Osterwald [7] present systems also based on the variable resistor principle in order to characterize photovoltaic modules.

- Capacitive Load.

  The second measuring method is based on biasing the module by a large capacitor, which is charged while the former moves from short circuit to open circuit. A schematic circuit using this principle is shown in Figure 2.2.

  At the beginning of the measurement the capacitor is short-circuited and its loading starts when the *S3* switch is opened and the *S1* is closed. As the charge of the capacitor increases, current drops and

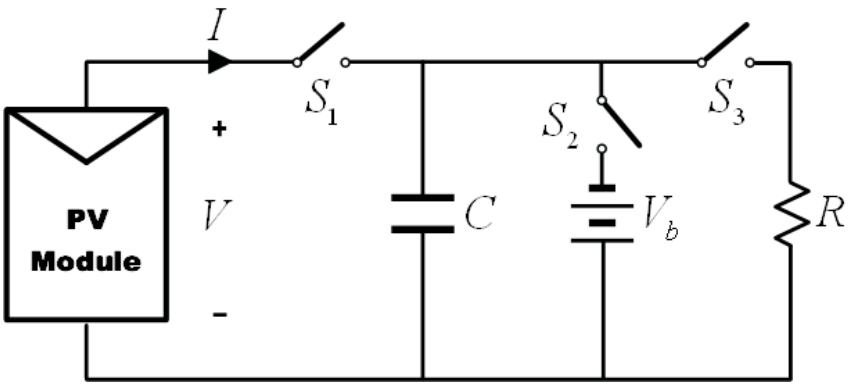

Figure 2.2: Capacitive load scheme

voltage rises. When the charge is completed, the current supplied by the module becomes zero and the open circuit condition is achieved. Instead of beginning in short circuit, we could start with *S2* closed, and the capacitor would then be initially charged to negative voltage and the *I–V* curve would cross the current axis in order to get I_{SC}. To obtain a reliable *I–V* curve with the capacitor method, high quality capacitors with small losses are required. In addition, the three switches must be activated with the appropriate sequence, and the prior discharge of the capacitor is needed to start a new measurement.

This method has been applied since the implementation of the earlier curve tracers for photovoltaic cells and modules. Warner and Cox [8] present a high power current voltage curve tracer employing a capacitive load.

Tzanetakis and Tsilis [9] describe two portable systems based on different principles. The first one is based on a capacitive load. They highlight the absence of noise in the measurement but they also state that one of the major drawbacks is the difficulty to fully cover the first quadrant.

In the system presented by Recart et al. [10], the voltage and current are monitored using a computer card. The measurement starts when the card sends a trigger signal to the switch that connects the capacitor to the cell. Muñoz and Lorenzo [11] describe a portable capacitive load based on insulated gate bipolar transistors (IGBTs), for PV arrays under real operating conditions. The switches are implemented using IGBTs and the capacitor is performed with a parallel arrangement of capacitors and resistors.

Mahmoud [4] presents a capacitive load system, reporting that the capacitor size must be directly proportional to the I_{SC} and indirectly proportional to V_{OC} . Furthermore, the higher the speed of the measuring system, the smaller the size of the required capacitor will be. Accordingly, this paper presents a capacitance calculation chart, which enables selecting the correct capacitance for measuring the I–V characteristics by a computerized data acquisition system.

Most of the commercially available curve tracers use this principle. Two known examples could be the PVPM from PV–Engineering GmbH [12] and the DS–100C from Daystar Inc [13] . Both are portable solutions with battery designed thinking in PV arrays and plants. Their accuracy is not suitable in order to measure cells or modules.

- Electronic Load.

  The electronic load method (Figure 2.3) uses a transistor (usually a MOSFET) as load; the resistance between drain and source is modulated through the gate source voltage, and consequently the flow of current supplied by the module. When this method is used to trace the I–V curve of the module, the MOSFET must operate in its three operating modes (cut–off, active and ohmic region). As a result, most of the power delivered by the module will have to be dissipated by this device, which limits its application to medium power.

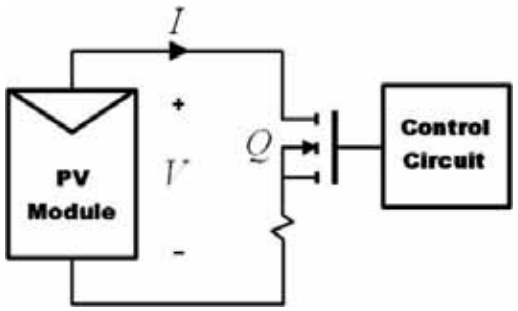

Figure 2.3: Electronic load scheme

In the article of Kuai and Yuvarajan [14], a simple electronic load based on a MOSFET is proposed to achieve the I–V curve of panels by quickly scanning the load. Its advantage is the fast variation of the equivalent load resistance of the MOSFET. The linear MOSFET is driven by a low frequency scan signal with a large enough amplitude to cover the complete range of panel characteristic. Several MOSFETs can be operated in parallel to handle higher output current from an

array with several PV panels. The output voltage and current are sensed using a potential divider and a sensing resistor respectively. The outputs are fed to an oscilloscope to display the curve. I_{SC} and V_{OC} are obtained using two peak detectors and voltage and current signals are multiplied using a multiplier to get instantaneous power. Thus, a third peak detector can be used to capture the P_{M} value.

Forero et al. [15] introduce a system for monitoring the performance of PV solar plants, including I–V curves measurements, which are obtained over a short period to prevent cloud interference during outdoor measurements. The electronic load is constituted by several transistors in cascade. By reducing the transistor base current gradually, the PV generator moves from the short circuit point to the open circuit voltage point. A data acquisition card with high–speed A/D converter is used to measure the current and voltage, while the operating point changes. The innovation of this circuit is that the scan of the I–V curve is controlled through a current ramp, instead of using a voltage ramp.

Salmon et al. [16] present a circuit to measure I–V curves of PV multi–junction cells (those that have more than one junction in order to capture photons from a wider spectral band). An n–channel MOSFET transistor and an operational amplifier are combined to create the voltage controlled current sink. For each current setting a differential amplifier is used to read the voltage across the solar cell, which it sweeps through several points along its characteristic curve. Data gathered for each curve includes solar cell temperature, solar angle and time.

Kattakayam et al. [17] and Mantingh et al. [18] describe systems that are likewise based on an electronic load in order to bias the module.

- DC–DC Converter.

  The ability of DC–DC converters to emulate a resistor has been studied and analyzed in several applications. This property of acting as resistor emulators of the DC–DC converters has been applied to obtain I–V curves of solar modules. There are three basic converter configurations: buck converter, boost converter and buck–boost converter. In a DC transformer the relationship of transformation can be controlled electronically by changing the duty cycle of the converter in the range $(0, 1)$. Figure 2.4 shows the scheme to characterize a module by means of a DC–DC converter with duty cycle sweep (R_i is the emulated resistor on the terminals of the module).

Matsuo and Kurokawa [19] use a boost type bidirectional DC–DC converter and a simple control circuit in order to track the maximum power point (MPP) of a solar array. Furthermore, a power efficiency comparison between the new MPP tracker and a conventional one is performed both theoretically and experimentally.

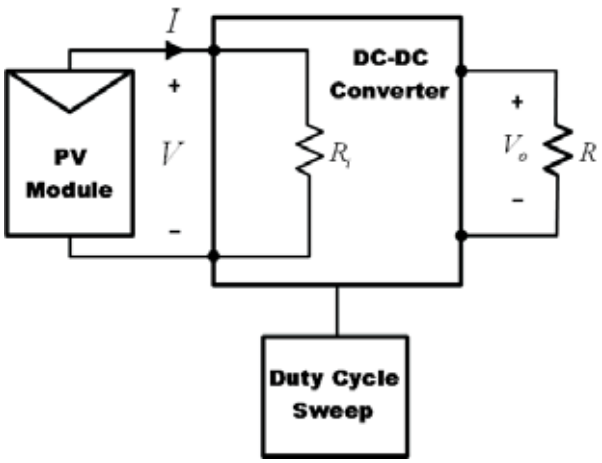

Figure 2.4: DC–DC converter scheme

Sanchis et al. [20] present a system based on a boost bidirectional DC–DC converter with two operation modes: a measurement mode in order to acquire the I–V characteristic curve of a photovoltaic generator, and an emulation mode in which the system simulates the measured generator to test photovoltaic inverters. A 15–kW prototype is designed and built. With the proposed device, the optimal configuration and performance of photovoltaic modules and generators, as well as the operation of photovoltaic inverters can be thoroughly analyzed under real atmospheric conditions.

A controllable DC load based on buck converter with input filter is described by Kazerani [21]. The features of this load are its simple structure, low cost and fast response. The load can be used to test and evaluate single fuel cells, fuel cell stacks or solar arrays.

Along with describing the system based on capacitive load, Tzanetakis and Tsilis [9], present a system based on a buck–boost DC–DC converter loaded by a halogen incandescent lamp. The load can be varied continuously by a microcontroller between open and short circuit.

Likewise based on this scheme, Durán et al. [22] present an automatic system to trace I–V curves. They demonstrate that the buck converter

does not allow the points of the curve that are close to I_{SC} to be traced, whereas the boost converter cannot reach the points near to V_{OC} . Yet buck–boost, Zeta, Cuk and SEPIC (Single Ended Primary Inductance Converter) schemes allow a complete sweep of the curve. Furthermore, when Cuk or SEPIC structures are used the reproduction of the *I–V* curve is achieved with less ripple (the current ripple by the inductor due to the switching technique is the main drawback of DC–DC converter method).

- Four–quadrant Power Supply.

  Several photovoltaic research laboratories use a system based on a four–quadrant power supply. This type of equipment is capable of delivering as well as dissipating power; in other words, it can source or sink power (Figure 2.5). This method involves a circuit that allows the current and voltage in the module to be reversed. Its scheme is based on a traditional class B power amplifier (Figure 2.6). It uses two BJTs transistors as load, for forward and reverse current respectively. The bipolar transistors must operate in its three operating modes (cut–off, active and saturation region). As a result, most of the power delivered by the module will have to be dissipated by those devices, which limits its application to medium power (four–quadrant power supplies that work over 1 kW are not readily available). This type of system is also intrinsically expensive.

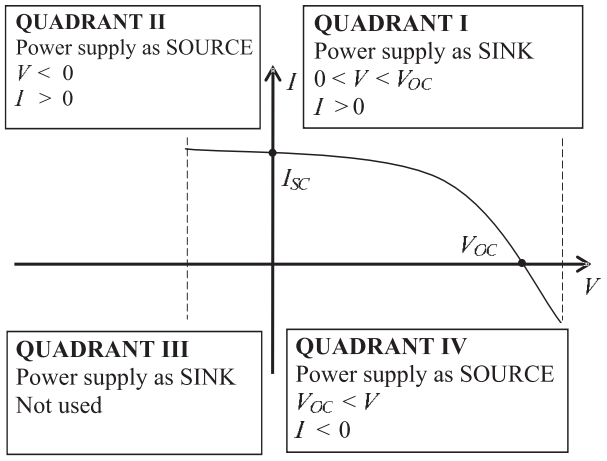

Figure 2.5: *I–V* characteristic in 1^{st}, 2^{nd} and 4^{th} quadrant

Although photovoltaic modules are designed to operate in the first quadrant, the exploration of the points lying in the second and fourth

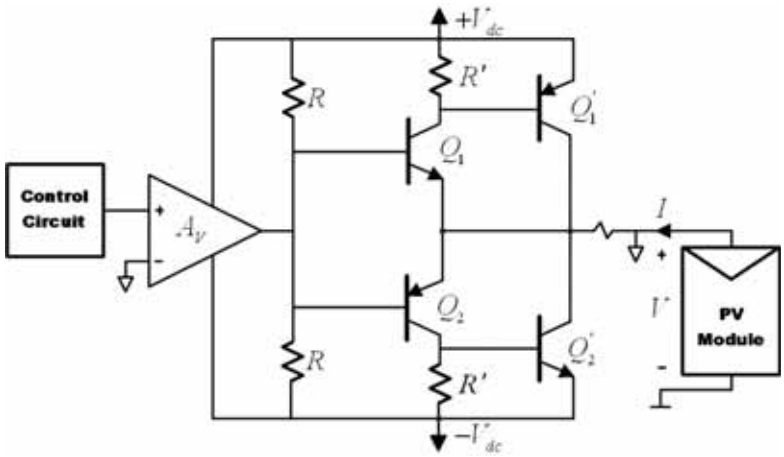

Figure 2.6: Four–quadrant power supply scheme

quadrant may be an important diagnostic tool. Points can then be captured around the axes, the reverse bias characteristic measured and the dark I–V curves of the modules measured. This method has been implemented in our experimental system described in the next section of this chapter. Previous proposed systems that use the same method will be reviewed.

Guvench et al. [23] present a PC controlled test setup based on this method. It seeks to measure the I–V characteristics of large–area solar cells under an artificial light source, which simulates solar radiation. The measurement is done in an automated way by employing standard GPIB instruments interfaced to a PC. The high test current needed by the large area solar cell is provided by a four–quadrant power supply driven by a function generator, which performs a stepped voltage at its output (the power supply amplifies the signal provided by the function generator). An application controls the function generator to start from a minimum bias voltage and step up in increments, until the maximum bias or a maximum safe current value is reached. The voltage and current at each step are sensed taking advantage of the separate voltmeter and ammeter inputs of the same digital multimeter.

Recart et al. [10] (in this paper a system based on a capacitive load is also described) present a very similar circuit to bias voltage of a cell, but instead of using a function generator to perform the ramp, a D/A card plays the role of control circuit.

Almonacid et al. [24] perform a study about CIS modules and use a measurement system based on a four–quadrant power supply. An

application developed in LabView drives the power supply in order to perform the voltage stepped ramp without using a function generator. In each step, the computer sends a command to establish a bias voltage and then a data logger with an unique internal multimeter and several multiplexed channels registers voltage and current (with the help of a shunt resistor) in a sequential order (not simultaneous). It is possible as the bias voltage is fixed when measuring the voltage and current for the same point of the curve.

Another system presented by Malik and Damit [3] uses a variable bipolar operational power supply with four–quadrant capability (in this paper a system based on variable resistor principle is also presented). In this case, the voltage on the power supply is also modified step by step. However, the voltage across the solar cell is measured using a digital multimeter and a further one is used to measure the voltage drop across the shunt that senses the current. The reverse bias characteristic is likewise determined in this system.

A step by step variation of the bias voltage requires a delay between the measuring of each point of the curve. Therefore, the acquisition of the curve is very time consuming and is not adequate in order to measure modules under outdoors conditions as the irradiance level could vary in a very short time. Emery [25] suggests generating a continuous voltage ramp to bias the module from an initial voltage to a final voltage. In this case, equipment capable of acquiring two channels (voltage and current) simultaneously need to be used in order to ensure that both measurements correspond to the same point of the characteristic curve.

Hecktheuer et al. [26] describe a methodology to determine I–V characteristic curves of photovoltaic modules under diverse conditions. The voltage sweep of the power supply is controlled automatically by a computer. The voltage and current are measured simultaneously by two digital multimeters connected to a computer via GPIB. The computer retrieves the acquired data and the main electrical parameters are determined. De Blas et al. [27] use an identical system, but in this case the curve is rejected if the measured irradiance at the beginning and at the end of the sweep varies significantly.

Fernández–Reche et al. [28] describe a concentration photovoltaic cell characterization facility. The PV cells are illuminated with a solar parabolic concentrator and a set of shutters allows control the PV cell exposition time obtaining a train of flashes over the cell but using solar radiation. Synchronized with the shutters is a set of instruments that

measures the I–V curves. All the points of the curve can thus be found in successive radiation flashes. The sweep is controlled by a waveform generator that is able to generate a pre–programmed analogue voltage ramp that is amplified by the power supply. Two channels (current and voltage) of a power analyzer are used as a high speed and simultaneous data acquisition of the curve.

Granek and Zdanowicz [29] present a system in which the voltage of the power supply is controlled by a D/A converter of a computer card. Current is measured as the voltage drop on a resistor measured by an input channel of an A/D converter of the same computer card. Several resistors are available and each one can be automatically selected using binary output signals of the computer card accordingly to the current range of the module to measure.

Powell et al. [30] perform a study about the stability of CdTe/CdS modules and their measurements likewise use a four–quadrant power supply to bias the module and a 12–bit A/D card to measure the current and the voltage values.

A detailed comparison is eventually accomplished, in order to emphasize the properties of the different methods presented. The comparison is carried out with the following fundamental parameters for measuring systems. At the end of this section, Table 2.1 summarizes the properties for each method taking into account these parameters.

A. Flexibility: It is an important comparison factor and plays an important role to select one of the methods. A partial reproduction of the I–V curve is possible using a four–quadrant power supply; in addition the range, speed and direction of the sweep are easy to configure. This can likewise be performed with the DC–DC converter by modifying the duty cycle, so specific zones of the I–V curve can be partially reached. It can be operated continuously around the maximum power point of the photovoltaic module under test. The methods based on electronic load also show high flexibility, but the reproduction of points around the MPP requires excessive power dissipation, especially with high–power generators, since the transistors operate in their linear zone. A partial reproduction of the I–V curve or changing the speed and direction of the sweep are not possible with the capacitive load method.

B. Modularity: This concept is related to the ability of the system to scale and grow in order to cover greater ranges. The method based on

DC–DC converter allows the system to be expanded by merely connecting several converters in parallel. Variable resistor and electronic load methods present difficulties when the power of the array under test increases. In both cases, the principal design concern is power dissipation. When using the capacitor load method, the size of the capacitor needs to be adapted by increasing the time to perform the sweep. In the case of four–quadrant power supply, modularity is only possible with some manufacturers, which provides a cable kit in order to combine several equipments and control them as a single device. However, this solution involves an excessive increase in cost.

C. Fidelity: Evaluating the reliability of each method is very hard as this feature is largely dependent on the data acquisition system. However, with the method based on four–quadrant power supply and DC–DC converter, high fidelity is achieved even for a high speed sweep. An exhaustive analysis of the reviewed methods reveals that it is difficult to reproduce the exact point of zero voltage (I_{SC}). Four–quadrant power supply and DC–DC methods only need an interpolation around zero volts. Interpolation can likewise be applied in the capacitor method, but only if a prior negative charge is imposed. Only an extrapolation is possible with the variable resistor method and electronic load method. The calculation of the maximum power (P_{M}) also presents difficulties. It is often taken to be the largest power value of all points of the sample. Therefore, accuracy depends on the density of points around the knee of the curve. This feature can only be controlled with the DC–DC and four–quadrant power supply methods.

D. Fast Response: This is particularly interesting as it ensures that all points of the curve have been acquired under the same meteorologic conditions. The possibility of configuring the sweep speed is likewise important, as it increases the flexibility and reliability of the system.

E. Cost: A good cost evaluation can usually be made by taking into account the data acquisition system, the development of the software and the number of sensors required. The costs vary considerably depending on the accuracy and sampling rate of the current and voltage sensors. Although a four–quadrant power supply could be very expensive, our system is based on it as it is good value for the cost, if the previous considerations are taken into account.

	Flexibility	Modulartiry	Fidelity	Fast Response	Cost
Variable Resistor	Low	Low	Low	Low	Low
Capacitive Load	Low	High	Low	Medium	Medium
Electronic Load	Low	Medium	Medium	Medium	Medium
DC–DC Converter	Medium	Medium	Medium	High	Low
4–quadrant Supply	High	Medium	High	High	High

Table 2.1: Characteristics of the different methods

2.3 Architecture of the system

To measure the I–V curve, all previous described systems are based on reading the current supplied by the photovoltaic module when voltage is increased gradually between the short circuit point and open circuit point. Our system is based on a four–quadrant power supply (Kepco BOP 100–10MG), a type of equipment capable of delivering as well as dissipating power. This model is able to work in a voltage range of ± 100 V and in a current range of ± 10 A (Table 2.2 summarizes the main characteristics of this device, extracted from its user manual [31]). The I–V curve can then be performed beyond the first quadrant in order to measure the reverse bias characteristic, which is closely related to mismatch effects, partial shading of PV arrays and hot–spot testing [32]. Moreover, obtaining points around the axes allow us to estimate I_{SC} and V_{OC} more accurately. A computer connected to the power supply using GPIB protocol controls the voltage sweep automatically. A programming language called SCPI is used to command the device. The scheme used for measuring the I–V curve is shown in Figure 2.7. A snapshot of the system can be seen in Figure 2.8.

Module voltage is measured in a four–wire configuration (the pair of wires used to bias the module is not the same as the one used to measure voltage between its terminals) in order to avoid errors due to voltage drop. Module voltage is measured using a digital multimeter (Agilent 34411A) connected to its terminals. Module current is sensed with the help of a shunt resistor in series between the module and the power supply. The voltage drop across the shunt is measured using another digital multimeter (Agilent 34411A). Both multimeters are connected to the control computer via GPIB. While the sweep is being performed, the multimeters store the measurements in their internal data memory and when the process is finished the control computer retrieves the acquired data. Table 2.3 summarizes the main features of the multimeter used in our system (extracted from its user manual [33]).

BOP 100–10MG FEATURES	
Load type	Four quadrant (sink and source operation)
Communication Interface	Controllable via RS232 or GPIB (SCPI language)
Maximum Power	1000 W
Output Voltage	±100 V
Output Current	±10 A
Other features	Energy recuperation during sink–mode through a bi–directional PFC circuit
	High efficiency switch–mode operation
	Keypad control from front panel with menu to access functions
	Large graphic LCD that displays settings and actual output
	Waveform generation (RAMP, SIN, SQUARE, TRIANGLE)

Table 2.2: Main features of Kepco BOP 100–10MG power supply

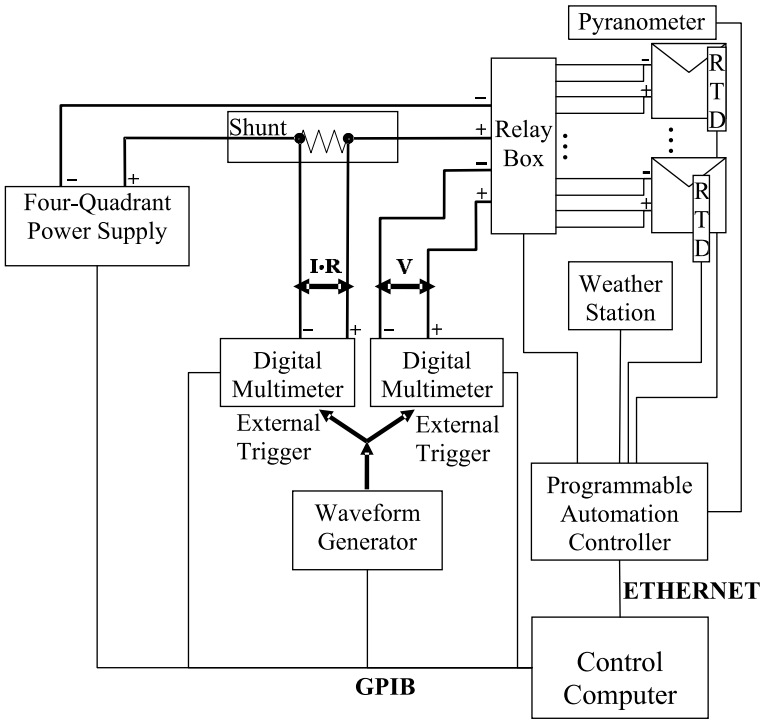

Figure 2.7: Proposed scheme for measuring *I–V* curves of PV modules.

Figure 2.8: Snapshot of the *I–V* tracer system at our laboratory

Agilent 34411A FEATURES	
Max. resolution	6 1/2 digit
Communication Interface	LAN, USB and GPIB (SCPI language)
Maximum sampling rate	50 000 readings/s at 4 1/2 digit
Reading memory	1 MByte
Other features	Analog level and pre/post triggering
	Capacitance and temperature measurements
	Data logger for improved usability

Table 2.3: Main features of Agilent 34411A multimeter

The main contribution of the developed system is the way in which the two multimeters are synchronized. As the operating point of the module is continuously changing during the voltage sweep, a small difference in time between the triggering of the two multimeters implies that the components in voltage and current of a measured point belong to different operating points of the actual *I–V* curve. Previous systems synchronize the multimeters through GPIB protocol which allows the multiple devices to be simultaneously triggered using a single SCPI sentence. In contrast, we propose a different *I–V* measurement synchronization method based on using a waveform generator (Agilent 33220A) which performs a square signal for triggering both multimeters (both of them have been programmed in order to acquire a measurement every time there is a pulse through their external trigger input). The proposed synchronization method ensures that the two measurements are performed simultaneously as both multimeters use the

same time base. This synchronization method is far more accurate than the software synchronization via GPIB as it is proved in the following section.

The *I–V* curve of a module can be performed in two different ways: with one ramp or with two ramps. In the first case only one ramp is performed and then the bias rate is the same throughout the measuring range; this means that the *I–V* curve points are equally spaced along the voltage axis. Whereas in the second case two ramps are performed; a fast ramp between the initial voltage and an intermediate voltage (before the knee of the *I–V* curve), and another slow ramp between that intermediate value and the final voltage value. This implies that more points are going to be captured while the performing of this second ramp that covers the knee and the part of *I–V* curve with more slope (on the flat part of the curve it is not necessary to take lots of points). In the experimental results presented in section 2.7 the *I–V* curves have been performed using two ramps. This allows us to acquire more experimental points around the maximum power point and open circuit point, so that P_{M} and V_{OC} will be determined more accurately.

Kipp & Zonen CMP21 FEATURES	
ISO classification	Secondary standard
Response time (95 % response)	< 5 s
Zero offset (radiative transfer)	$\pm 7\,{}^{\mathrm{W}}/_{\mathrm{m}^2}$
Zero offset (temperature change)	$\pm 2\,{}^{\mathrm{W}}/_{\mathrm{m}^2}$
Resolution (smallest change)	$\pm 1\,{}^{\mathrm{W}}/_{\mathrm{m}^2}$
Stability (change per year)	< 0.5 %
Temperature response	< 1 %
Non-linearity	± 0.2 %
Tilt response at $1000\,{}^{\mathrm{W}}/_{\mathrm{m}^2}$	± 0.2 %

Table 2.4: Main features of Kipp & Zonen CMP21 pyranometer.

Meteorological parameters are also acquired at the same time as the *I–V* curve. Module temperature is measured using a RTD Pt100 sensor coupled to its backside and irradiance incident on the module surface is measured using a Kipp & Zonen CMP21 pyranometer (Table 2.4 summarizes its main features extracted from its user manual [34]). These signals are recorded at the beginning and at the end of each measurement, and the curve is stored only if the difference between them is less than a threshold fixed by the user. These and other sensors (such as anemometer, vane, rain gauge ...) are connected to a modular acquisition data system National Instruments FieldPoint cFP–2120 (Table 2.5 summarizes its main features extracted from its user manual [35]) controlled by the control computer through an Ethernet

interface. The communication with the data acquisition system is performed through a server/client protocol called OPC–DA [36], based on DCOM technology. This standard can be used to retrieve real–time data among many different devices in a unified way, using the OPC server delivered by the manufacturer of the device.

cFP–2120 PAC FEATURES	
Microprocessor frequency	188 MHz
RAM memory	128 MBytes of SDRAM
Non–volatile memory	128 MBytes
Removable media	CompactFlash
Communication Interface	1 Ethernet ports 100BaseTX, 4 serial ports (3 RS232 and 1 RS485)
Other features	Execution target for NI LabVIEW Real–Time applications
	Distributed real–time systems
	Available OPC Server

Table 2.5: Main features of Compact FieldPoint cFP–2120 programmable automation controller.

In order to perform automated measurements of different modules, our system integrates a relay box that multiplexes up to eight modules. Each module can be automatically selected or sequentially measured. Several modules can thus be selected and measured in succession in a short time. A cFP–RLY–425 module is installed inside the acquisition data system to control this relay box.

The control program, written in the Borland Delphi programming language, allows the user to configure the range and the duration of the voltage sweep (in order to adapt the bias rate to the technology of the module under test), current limits to protect the module, the number of point of each curve and the time interval between curves, among others parameters. Current–voltage acquired values are processed to determine I_{SC}, V_{OC}, P_M, I_M, V_M and FF under measurement conditions. Eventually, this information is stored in a relational database implemented with MySQL [37]. All measured I–V curves can be shown through a web page ordered by months and days. The user can see the information displayed in a table or graphically. Furthermore, selected data can be exported to a file to process measurements with an external application in order to perform more advanced processing of the measured curves, such as estimating other important parameters of the module.

2.4 Proposed synchronization method

Traditionally, a four–quadrant power supply performs a voltage sweep while two multimeters record the current and voltage values. These multimeters are synchronized by software through GPIB protocol and SCPI language using a single statement to trigger several devices simultaneously. A small time difference in the timing of the two multimeters means that the measured I and V values do not correspond to the same instant of time and therefore they do not correspond to any value of the I–V curve. This difference can be particularly significant near the V_{OC} where the slope of the curve is maximum.

Two experiments have been conducted to compare two synchronization methods: synchronization by software and synchronization by external triggering (implemented in our system). In both experiments, a ramp from –50 V to +50 V was generated with duration of one second. One hundred measurements were recorded for this time using two multimeters connected at the same point. In the first experiment, the voltmeters were synchronized using GPIB and in the second one the proposed method was used. If the measurements of the two multimeters were made at the same instant, both of them should register the same value. The differences between the measurements recorded by the two voltmeters in each experiment are a measurement of the accuracy of the synchronization method. The differences of two voltmeters measurements throughout the range of voltage for the first experiment (GPIB synchronization) are presented in Figure 2.9. These results show that the difference between the measurements made by both multimeters is much larger than the uncertainty associated with the voltage measurement. This means that measurements cannot be considered as simultaneous.

The results obtained by synchronizing the multimeters using the method proposed in this paper are presented in Figure 2.10. In this case, the differences between the measurements of the two multimeters are much lower than those obtained by the GPIB method and they are always lower than the estimated uncertainty. In Figure 2.11 the axis scale is magnified in order to assess the measured values with uncertainty. These differences are much smaller than the associated uncertainty. Therefore, the proposed synchronization method is more accurate than previous ones and it does not increase the uncertainty associated to experimental measurements.

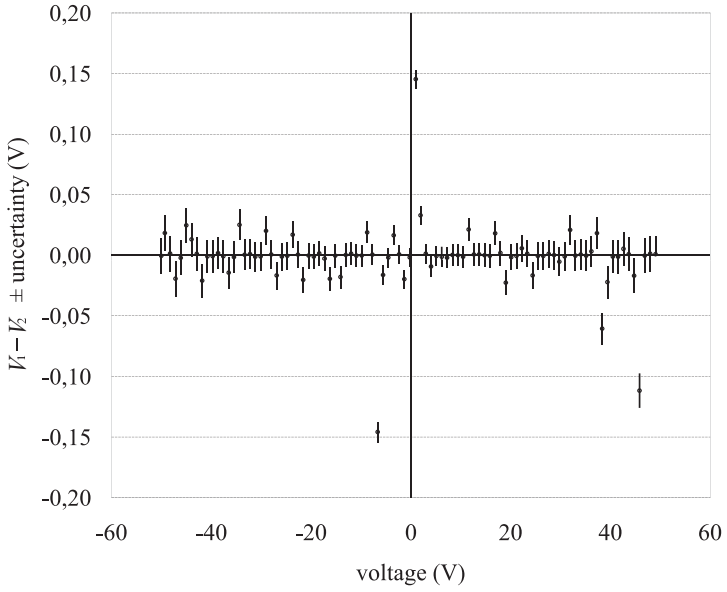

Figure 2.9: Voltage differences between the voltage measures of two multimeters when the synchronization is performed using GPIB (software).

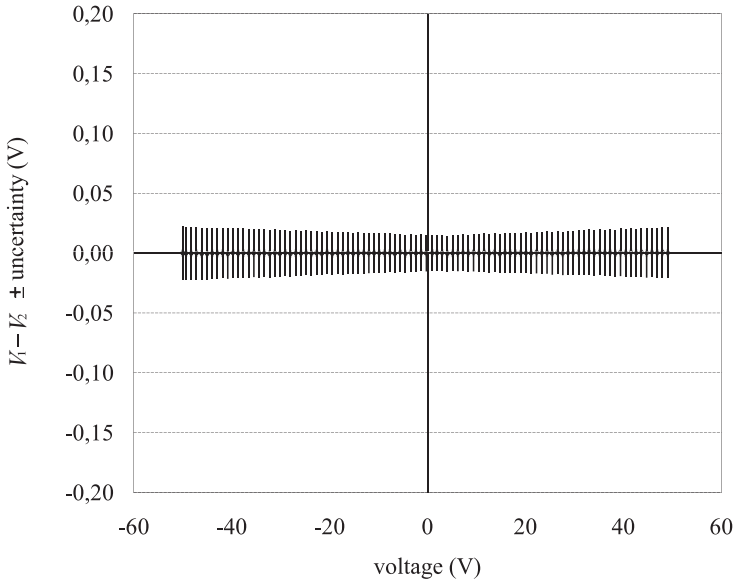

Figure 2.10: Voltage differences between the voltage measures of two multimeters when the synchronization is performed using the proposed method and expanded uncertainty for each value.

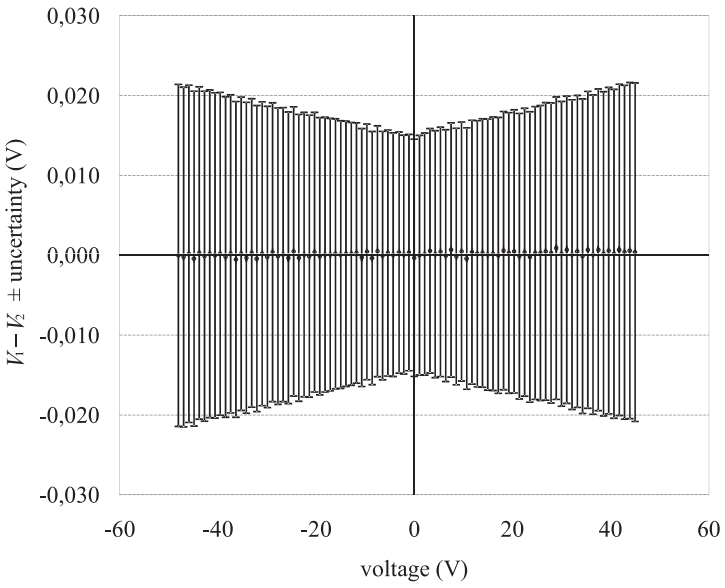

Figure 2.11: Zoom detail of Figure 2.10

2.5 Analysis of uncertainty

In this section, the uncertainty in the measurement of the discrete points belonging to the *I–V* curve is analysed (the estimation of calculated parameters and their uncertainty are studied in the next section). In order to evaluate the uncertainty of the proposed system, ISO–GUM [38], the concepts included by Taylor and Kuyatt [39] and the procedure proposed by Whitfield and Osterwald [40] have been used. Type B evaluation can be stated as an estimation of the uncertainty of a variable that has not been obtained from repeated observations, so this type of uncertainty has been taken into account at each point of the *I–V* curve. In this case, the uncertainty could be calculated using information given by the manufacturers of the instruments and their configuration and calibration. According to the multimeter user manual [33], its accuracy is expressed as the sum of two terms:

$$Accuracy = (\%\ \text{of reading}) \cdot (reading\ value) + (\%\ \text{of range}) \cdot (range\ value)$$

These parameters can be calculated from the tables provided by the manufacturer taking into account the integration time, the used range and the operation temperature of the instrument. While photovoltaic module voltage is measured directly by one of the multimeters using ±100 V range, the photovoltaic module current is estimated using a class 0.1 shunt resistor (this value means the relative accuracy of the shunt expressed as percentage) with

10 A of nominal value and an output equal to 100 mV, whose voltage drop is measured by another digital multimeter using ±100 mV range.

	A		B^*	C	
	A_1^*	A_2^{**}		C_1^*	C_2^{**}
$Voltage \pm 100$V	0.0040	0.0006	0.0015	0.0005	0.0001
$Current \pm 100$mV	0.0050	0.0035	0.0150	0.0005	0.0005

* % of reading ** % of range

Table 2.6: Different contributions to the accuracy of a measurement made with an Agilent 34411A multimeter

Table 2.6 shows the different contributions to the relative accuracy. In this table, A_2 is given for an integrated time of 100 PLC (power line cycles, where 1 PLC is 20 ms if AC grid frequency is 50 Hz). Both multimeters have been configured to use an integration time value of 0.2 PLC, which enables up to 300 measurements to be taken in one second using 18 bits for analog–to–digital conversion. As we use 0.2 PLC we must add to A_2 (% of range) another term B (% of range) called RMS Noise Adder, that depends on selected range and integration time used. If the difference between the operation temperature (the laboratory temperature in our case) and the calibration temperature of the multimeter (23 °C) is greater than 5 °C, A_1 and A_2 need to be increased by a quantity, C_1 and C_2 respectively, that depends on the selected range. The reading value must be taken as absolute value and range value must be set to 100 V (although the actual range is 200 V, from –100 V to +100 V). Taking into account the values given in Table 2.6(first row), the accuracy of voltage at module terminals is

$$\begin{aligned} e_V(\mathrm{V}) &= (A_1+C_1)\cdot 10^{-2}\cdot(reading\,value)+(A_2+B+C_2)\cdot 10^{-2}\cdot(range\,value) \\ &= 4.5\cdot 10^{-5}\cdot|V|+2.2\cdot 10^{-3} \end{aligned}$$

According to Whitfield and Osterwald [40], the voltage measurement uncertainty is a combination of resolution and accuracy of the multimeter used. The expanded uncertainty with 95 % confidence (coverage factor=2) has been estimated using the following expression:

$$U_V(\mathrm{V}) = 2\cdot\sqrt{\left(\frac{R_V}{2^n\sqrt{12}}\right)^2+\left(\frac{e_V}{\sqrt{3}}\right)^2+\left(\frac{U_V^C}{2}\right)^2}$$

where R_V is the multimeter range (200 V, from –100 V to +100 V), n is the number of bits of the analog–to–digital converter (18 bits), $e_{_V}$ is the accuracy

of the instrument given by the previous equation, and U_V^C is the expanded uncertainty of the reference standard reported at the 95 % confidence level from an approximately normal distribution (coverage factor of 2). The calibration certificate states that the calibrator instrument has a tolerance to uncertainty ratio (TUR) greater than 4:1, so U_V^C is equal to the multimeter accuracy e_V divided by 4. By substituting and reducing we have,

$$\begin{aligned} U_V(\mathrm{V}) &= 2 \cdot \sqrt{\left(\frac{200}{2^{18}\sqrt{12}}\right)^2 + \left(\frac{e_V}{\sqrt{3}}\right)^2 + \left(\frac{e_V}{4 \cdot 2}\right)^2} \\ &= 2 \cdot \sqrt{7.1 \cdot 10^{-10} \cdot V^2 + 6.9 \cdot 10^{-8} \cdot |V| + 1.7 \cdot 10^{-6}} \end{aligned}$$

This uncertainty depends on the measured value. This means that each point of the I–V curve will have a different uncertainty. Worst cases occur when $V = \pm 100$ V. Then, the voltage uncertainty in the worst–case will be $U_{V,worst}$=0.008 V.

As for the voltage, in order to estimate expanded current uncertainty U_I, the accuracy of the multimeter that measures the voltage drop across the shunt e_I^V must first be calculated taking into account its range ($\pm$100 mV) and the parameters given in Table 2.6(second row). So we have,

$$\begin{aligned} e_I^V(\mathrm{mV}) &= (A_1 + C_1) \cdot 10^{-2} \cdot (reading\, value) + (A_2 + B + C_2) \cdot 10^{-2} \cdot (range\, value) \\ &= 5.5 \cdot 10^{-5} \cdot |V_{shunt}| + 1.9 \cdot 10^{-2} \end{aligned}$$

This measurement is also affected by another source of uncertainty due to the shunt resistor. As the shunt resistor class is 0.1, we have that,

$$e_I^{shunt}(\mathrm{mV}) = 0.1\,\% \cdot |V_{shunt}| = 10^{-3} \cdot |V_{shunt}|$$

The expanded uncertainty associated to the voltage drop across the shunt is a combination of resolution and accuracy of the multimeter used and can be estimated using the expression (95 % confidence, coverage factor=2):

$$U_I^V(\mathrm{mV}) = 2 \cdot \sqrt{\left(\frac{R_I^V}{2^n\sqrt{12}}\right)^2 + \left(\frac{e_I^V}{\sqrt{3}}\right)^2 + \left(\frac{e_I^{shunt}}{\sqrt{3}}\right)^2 + \left(\frac{U_I^C}{2}\right)^2}$$

where R_I^V is the multimeter range (200 mV, from –100 mV to +100 mV), n is the resolution of analog–to–digital converter (18 bits), e_I^V is the accuracy of the instrument, e_I^{shunt} is the accuracy of the shunt, and U_I^C is the expanded uncertainty of the reference standard reported at the 95 % confidence level

from an approximately normal distribution (coverage factor of 2). The calibration certificate states that the calibrator instrument has a tolerance to uncertainty ratio greater than 4:1, so U_I^C is equal to the multimeter accuracy e_I^V divided by 4. Substituting and by reducing we have that,

$$\begin{aligned} U_I^V(\text{mV}) &= 2 \cdot \sqrt{\left(\frac{200}{2^{18}\sqrt{12}}\right)^2 + \left(\frac{e_I^V}{\sqrt{3}}\right)^2 + \left(\frac{10^{-3} \cdot |V_{shunt}|}{\sqrt{3}}\right)^2 + \left(\frac{e_I^V}{4 \cdot 2}\right)^2} \\ &= 2 \cdot \sqrt{3.3 \cdot 10^{-7} \cdot V_{shunt}^2 + 7.3 \cdot 10^{-7} \cdot |V_{shunt}| + 1.3 \cdot 10^{-4}} \end{aligned}$$

According to the Ohm law, $I = \dfrac{10\ \text{A}}{100\text{mV}} \cdot V_{shunt}$, so current measurement uncertainty U_I must be calculated as,

$$\begin{aligned} U_I(\text{A}) &= \frac{10\ \text{A}}{100\ \text{mV}} \cdot U_I^V \\ &= 0.1 \cdot 2 \cdot \sqrt{3.3 \cdot 10^{-7} \cdot V_{shunt}^2 + 7.3 \cdot 10^{-7} \cdot |V_{shunt}| + 1.3 \cdot 10^{-4}} \\ &= 2 \cdot \sqrt{3.3 \cdot 10^{-7} \cdot I^2 + 7.3 \cdot 10^{-8} \cdot |I| + 1.3 \cdot 10^{-6}} \end{aligned}$$

Worst case happens when the measured current equals the maximum current measurable with this shunt (10 A). So worst–case expanded uncertainty for current will be $U_{I,worst}$= 0.01 A.

According to ISO–GUM [38] and taking into account that $P = V \cdot I$, the expanded uncertainty (95 % confidence, coverage factor=2) associated to the power value of each point is calculated as:

$$\begin{aligned} U_P(\text{W}) &= 2 \cdot \sqrt{\left(\frac{\partial P}{\partial V}\right)^2 \cdot \left(\frac{U_V}{2}\right)^2 + \left(\frac{\partial P}{\partial I}\right)^2 \cdot \left(\frac{U_I}{2}\right)^2} \\ &= 2 \cdot \sqrt{I^2 \cdot \left(\frac{U_V}{2}\right)^2 + V^2 \cdot \left(\frac{U_I}{2}\right)^2} \\ &= 2 \cdot \sqrt{\begin{array}{l} 6.9 \cdot 10^{-8} \cdot |V| \cdot I^2 + 1.7 \cdot 10^{-6} \cdot I^2 + 7.3 \cdot 10^{-8} \cdot |I| \cdot V^2 + \\ +1.3 \cdot 10^{-6} \cdot V^2 + 3.4 \cdot 10^{-7} \cdot V^2 \cdot I^2 \end{array}} \end{aligned}$$

Finally, for the worst–case expanded uncertainty in power happens at point (100 V, 10 A) and its value is $U_{P,worst}$=1.2 W (95 % confidence level, coverage factor=2).

Each time an I–V curve is acquired, the irradiance and the module temperature are measured. Therefore, the uncertainties associated to these measurements must likewise be estimated. The output of the pyranometer is connected to a channel of the FieldPoint cFP–AI–112 module that, according to its operating instructions [41], its accuracy is also expressed as the sum of two terms:

$$Accuracy = (\%\text{ of reading}) \cdot (reading\ value) + (\%\text{ of range}) \cdot (range\ value)$$

These parameters can be calculated from the tables provided by the manufacturer taking into account the used range and the operation temperature of the instrument.

	15 °C to 35 °C		**-40 °C to 70 °C**	
	D_1^*	D_2^{**}	E_1^*	E_2^{**}
Voltage ±60 mV	0.05	0.3	0.10	1.5
* % of reading		** % of range		

Table 2.7: Different contributions to the accuracy of a measurement made with the cFP–AI–112 module

Table 2.7 shows the different contributions to the relative accuracy for the range used (±60 mV). In this table, D_1 and D_2 are given for a temperature operation range very close to the actual range in Malaga (Spain) when measurements are performed. Furthermore, the *range value* must be taken as 60 mV (although the actual range is 120 mV, from –60 mV to +60 mV). So, the accuracy of the module used to measure the output of the pyranometer can be expressed as

$$\begin{aligned} e_{V_{FP}}(\text{mV}) &= D_1 \cdot 10^{-2} \cdot (reading\,value) + D_2 \cdot 10^{-2} \cdot (range\,value) \\ &= 5.0 \cdot 10^{-4} \cdot |V_{FP}| + 1.8 \cdot 10^{-1} \end{aligned}$$

This module has an A/D converter of 16 bits (n=16) and a TUR of 4:1 implies that $U^C_{V_{FP}}$ equals $e_{V_{FP}}$ divided by 4. Thus, the expanded uncertainty due to cFP–AI–112 module with 95 % confidence level (coverage factor = 2) is:

$$
\begin{aligned}
U_{V_{FP}}(\mathrm{mV}) &= 2 \cdot \sqrt{\left(\frac{R_{V_{FP}}}{2^n\sqrt{12}}\right)^2 + \left(\frac{e_{V_{FP}}}{\sqrt{3}}\right)^2 + \left(\frac{U^C_{V_{FP}}}{2}\right)^2} \\
&= 2 \cdot \sqrt{\left(\frac{120}{2^{16}\sqrt{12}}\right)^2 + \left(\frac{e_{V_{FP}}}{\sqrt{3}}\right)^2 + \left(\frac{e_{V_{FP}}}{4 \cdot 2}\right)^2} \\
&= 2 \cdot \sqrt{8.7 \cdot 10^{-8} \cdot V_{FP}^2 + 6.3 \cdot 10^{-5} \cdot |V_{FP}| + 1.1 \cdot 10^{-2}}
\end{aligned}
$$

Following the work of Kratzenberg et al. [42], different contributions to the uncertainty in the irradiance measurement performed by pyranometer must be considered. Data needed to perform these calculations could be extracted from the pyranometer user manual [34] and the information provided by the calibration certificate. It has been reported that the sensitivity is $S = 8.66\,^{\mu\mathrm{V}}/_{\mathrm{Wm^{-2}}}$ from calibration by comparison with a CM21 pyranometer whose sensitivity is $S_C = 19.77\,^{\mu\mathrm{V}}/_{\mathrm{Wm^{-2}}}$ with $U^C_G = 0.25\,^{\mu\mathrm{V}}/_{\mathrm{Wm^{-2}}}$ (expanded uncertainty at 95 % confidence level and coverage factor=2). The directional response error $e_{_{DR}}$ is given in the calibration certificate as a tabular function of AOI (angle of incidence). For each measured I–V curve, the AOI could be determined knowing the latitude, date and tilt following the algorithm described by Reda and Andreas [43]. The manufacturer does not specify a value for the uncertainty due to the spectral response. The maximal variation due to spectral sensitivity $e_{_{SS}}$ for a secondary standard pyranometer must be less than 2%. However, a value of 0.5% is considered more realistic in this case [42]. Following a chart in the calibration certificate, the maximum temperature dependence $e_{_{TD}}$ could be considered equal to 0.4 %. The non–linearity error of the pyranometer $e_{_{NL}}$ and its tilt response error $e_{_{TR}}$ are quantified to be 0.2 %. Assuming that the instrument is calibrated each year, its non-stability error $e_{_{NS}}$ is estimated as 0.5 %. Finally, maximum zero offset values must be considered: due to changes in ambient temperature ($e_{_{TC}} = 7\,^{\mathrm{W}}/_{\mathrm{m^2}}$) and due to radiative transfer to the atmosphere $e_{_{RT}} = 2\,^{\mathrm{W}}/_{\mathrm{m^2}}$. Taking into account all these sources of uncertainty , it can be stated with 95 % confidence and a coverage factor equal to 2 that the expanded uncertainty in the measurement of the irradiance U_G is

$$
U_G(^{\mathrm{W}}/_{\mathrm{m^2}}) = 2 \cdot \sqrt{\begin{array}{l}\left(\frac{U_{V_{FP}}}{2 \cdot S}\right)^2 + \left(\frac{U^C_G \cdot G}{2 \cdot S_C}\right)^2 + \left(\frac{e_{DR} \cdot G}{\sqrt{3}}\right)^2 + \left(\frac{e_{SS} \cdot G}{\sqrt{3}}\right)^2 + \left(\frac{e_{TD} \cdot G}{\sqrt{3}}\right)^2 + \\ + \left(\frac{e_{NL} \cdot G}{\sqrt{3}}\right)^2 + \left(\frac{e_{TR} \cdot G}{\sqrt{3}}\right)^2 + \left(\frac{e_{NS} \cdot G}{\sqrt{3}}\right)^2 + \left(\frac{e_{TC}}{\sqrt{3}}\right)^2 + \left(\frac{e_{RT}}{\sqrt{3}}\right)^2\end{array}}
$$

$$= 2\cdot\sqrt{\begin{array}{l}\left(\frac{U_{V_{FP}}}{2\cdot S}\right)^2+\left(\frac{0.25\cdot 10^{-3}\cdot G}{2\cdot 19.77\cdot 10^{-3}}\right)^2+\left(\frac{e_{DR}\cdot G}{\sqrt{3}}\right)^2+\left(\frac{0.005\cdot G}{\sqrt{3}}\right)^2+\left(\frac{0.004\cdot G}{\sqrt{3}}\right)^2+\\ +\left(\frac{0.002\cdot G}{\sqrt{3}}\right)^2+\left(\frac{0.002\cdot G}{\sqrt{3}}\right)^2+\left(\frac{0.005\cdot G}{\sqrt{3}}\right)^2+\left(\frac{7}{\sqrt{3}}\right)^2+\left(\frac{2}{\sqrt{3}}\right)^2\end{array}}$$

Assuming that $\frac{V_{FP}}{S} = G$, the first term of the sum inside last expression can be rewritten as

$$\left(\frac{U_{V_{FP}}}{2\cdot S}\right)^2 = \frac{8.7\cdot 10^{-8}\cdot V_{FP}^2 + 6.3\cdot 10^{-5}\cdot |V_{FP}| + 1.1\cdot 10^{-2}}{S^2}$$

$$= 8.7\cdot 10^{-8}\cdot G^2 + 7.3\cdot 10^{-3}\cdot G + 1.5\cdot 10^2$$

Finally, the following expression can be achieved for the expanded uncertainty (95 % confidence, 2 coverage factor):

$$U_G(\mathrm{W/m^2}) = 2\cdot\sqrt{\left(\frac{e_{DR}^2}{3} + 6.5\cdot 10^{-5}\right)\cdot G^2 + 4.4\cdot 10^{-3}\cdot G + 1.7\cdot 10^2}$$

With normal incidence ($e_{DR} = 0$ %) and an irradiance equal to 1000 $\mathrm{W/m^2}$, the expanded uncertainty has a value of 30 $\mathrm{W/m^2}$ (3 %).

The uncertainty associated to the module temperature measurement will be estimated. First, there is a source of uncertainty due to the FieldPoint cFP–RTD–124 module accuracy. Its operating instructions [44] report the A/D converter resolution (n=16 bits), the absolute temperature accuracy ($e_{T_{FP}} = 0.25$ °C) supposing that the cFP–RTD–124 module is working between 15 °C and 35 °C and the measured temperature is in the range of –200 °C to 150 °C. A TUR value greater than 4:1 is likewise assumed, so the expanded uncertainty due to calibration U_T^C is $e_{T_{FP}}/4$. On the other hand, the tolerance of a class B Pt100 sensor, according to IEC 60751 [45] is given by the expression:

$$e_{Pt_{100}}(^\circ\mathrm{C}) = 5.0\cdot 10^{-3}\cdot |T_M| + 3.0\cdot 10^{-1}$$

The literature reports that the average cell–to–backskin temperature drop will be experimentally determined, being around $+2.5 \pm 1$ °C [40]. This is a systematic error that must be corrected, and a new source of uncertainty e_{TCO}(1 °C) due to the correction must be considered. Therefore, the next expression must therefore be considered (expanded uncertainty with 95 % of confidence and coverage factor equals 2),

$$U_T(\mathrm{W/m^2}) = 2\cdot\sqrt{\left(\frac{T_{max}-T_{min}}{2^n\cdot\sqrt{12}}\right)^2+\left(\frac{e_{T_{FP}}}{\sqrt{3}}\right)^2+\left(\frac{U_T^C}{2}\right)^2+\left(\frac{e_{Pt_{100}}}{\sqrt{3}}\right)^2+\left(\frac{e_{TCO}}{\sqrt{3}}\right)^2}$$

$$= 2\cdot\sqrt{\left(\frac{850-(-200)}{2^{16}\cdot\sqrt{12}}\right)^2+\left(\frac{0.25}{\sqrt{3}}\right)^2+\left(\frac{0.25}{4\cdot 2}\right)^2+\left(\frac{e_{Pt_{100}}}{\sqrt{3}}\right)^2+\left(\frac{1}{\sqrt{3}}\right)^2}$$

$$= 2\cdot\sqrt{8.3\cdot 10^{-6}\cdot T_M^2 + 1.1\cdot 10^{-3}\cdot |T_M| + 3.9\cdot 10^{-1}}$$

A module temperature reading of 50°C will have an associated expanded uncertainty of 1.4 °C.

2.6 Estimation of electrical parameters

Using the measured data, the main electrical parameters of each I–V curve must be estimated: the short–circuit current (I_{SC}), the open–circuit voltage (V_{OC}), the maximum power output (P_{M}), the current at the maximum power point (I_{M}), and the voltage at the maximum power point (V_{M}). Those values can be used to calculate other derived parameters as the fill factor (FF). The short–circuit current (I_{SC}) value is calculated by linear interpolation of the two closest points to the zero voltage axis (one point with negative voltage and the other with positive voltage). According to Emery [25], a linear regression using more than two points can be performed to reduce uncertainty, but this option had been discarded as there is a high risk of points resulting from bypass diodes being taken. In the same way, the open–circuit voltage (V_{OC}) is also obtained by linear interpolation of the two closest points to the zero current axis. Although the I–V curve is far from being linear around V_{OC}, a linear interpolation could be enough if the points are very close to the zero current axis.

Let $(V^- \pm U_V^-, I^- \pm U_I^-)$ and $(V^+ \pm U_V^+, I^+ \pm U_I^+)$ be the nearest points to the zero voltage axis with their respective expanded uncertainties. I_{SC} is estimated using the expression:

$$I_{\mathrm{SC}} = \begin{cases} I^- & if\ |V^-| \le U_V^- \\ I^+ & if\ |V^+| \le U_V^+ \\ I^- - \dfrac{I^+ - I^-}{V^+ - V^-}V^- & in\ other\ case \end{cases}$$

The associated expanded uncertainty for the first and second cases are U_I^- and U_I^+ respectively; for the third case it is:

$$U_{I_{\mathrm{SC}}}(\mathrm{A}) = 2 \cdot \sqrt{\begin{array}{l}\left(\frac{\partial I_{\mathrm{SC}}}{\partial I^-}\right)^2 \cdot \left(\frac{U_I^-}{2}\right)^2 + \left(\frac{\partial I_{\mathrm{SC}}}{\partial I^+}\right)^2 \cdot \left(\frac{U_I^+}{2}\right)^2 + \\ + \left(\frac{\partial I_{\mathrm{SC}}}{\partial V^-}\right)^2 \cdot \left(\frac{U_V^-}{2}\right)^2 + \left(\frac{\partial I_{\mathrm{SC}}}{\partial V^+}\right)^2 \cdot \left(\frac{U_V^+}{2}\right)^2\end{array}}$$

$$= 2 \cdot \sqrt{\begin{array}{l}\left(\frac{V^+}{V^+ - V^-}\right)^2 \cdot \left(\frac{U_I^-}{2}\right)^2 + \left(\frac{V^-}{V^+ - V^-}\right)^2 \cdot \left(\frac{U_I^+}{2}\right)^2 + \\ + \left(\frac{(I^+ - I^-)V^+}{(V^+ - V^-)^2}\right)^2 \cdot \left(\frac{U_V^-}{2}\right)^2 + \left(\frac{(I^+ - I^-)V^-}{(V^+ - V^-)^2}\right)^2 \cdot \left(\frac{U_V^+}{2}\right)^2\end{array}}$$

The estimation of V_{OC} and its expanded uncertainty is analogous.

The maximum power (P_{M}) is often taken to be the largest power value $\widehat{P_{\mathrm{M}}}$ of all points of the sample (V_{M} and I_{M} are also taken to be $\widehat{V_{\mathrm{M}}}$ and $\widehat{I_{\mathrm{M}}}$ respectively). However, as this value is selected from a discrete sample, it is an underestimation of the actual value of maximum power. Emery [25] suggests the use of more accurate methods, such as performing a fourth–order or higher polynomial curve fit to a selection of P–V pairs. In the proposed system, as there is a large amount of recorded data, the difference between two consecutive measurements surrounding the point of maximum power is always in the same order of magnitude as the measurement uncertainty; therefore we propose to take the maximum power point of the curve as the experimental value that maximizes the product $I \cdot V$. This requires a high density of points surroundings the maximum power point so that $\Delta P = |P_{i+1} - P_i| \leq U_P$. In the proposed experimental system, this condition is met as the number of points recorded in each area of the curve can be controlled, as described in section 2.3. The extended uncertainty of the maximum power point is calculated as described in section 2.5.

The fill factor is defined as,

$$\mathrm{FF}\ (\%) = \frac{P_{\mathrm{M}}}{I_{\mathrm{SC}} \cdot V_{\mathrm{OC}}} \cdot 100$$

Therefore, the expanded uncertainty of the fill factor of each curve could be estimated using the following expression,

$$\mathrm{U_{FF}} = 2 \cdot \sqrt{\left(\frac{\partial \mathrm{FF}}{\partial P_{\mathrm{M}}}\right)^2 \cdot \left(\frac{U_{P_{\mathrm{M}}}}{2}\right)^2 + \left(\frac{\partial \mathrm{FF}}{\partial I_{\mathrm{SC}}}\right)^2 \cdot \left(\frac{U_{I_{\mathrm{SC}}}}{2}\right)^2 + \left(\frac{\partial \mathrm{FF}}{\partial V_{\mathrm{OC}}}\right)^2 \cdot \left(\frac{U_{V_{\mathrm{OC}}}}{2}\right)^2}$$

$$= 2 \cdot \frac{100}{I_{\mathrm{SC}} \cdot V_{\mathrm{OC}}} \cdot \sqrt{\left(\frac{U_{P_{\mathrm{M}}}}{2}\right)^2 + \left(\frac{P_{\mathrm{M}}}{I_{\mathrm{SC}}}\right)^2 \cdot \left(\frac{U_{I_{\mathrm{SC}}}}{2}\right)^2 + \left(\frac{P_{\mathrm{M}}}{V_{\mathrm{OC}}}\right)^2 \cdot \left(\frac{U_{V_{\mathrm{OC}}}}{2}\right)^2}$$

2.7 Experimental Results

In Figure 2.12 , two experimental *I–V* curves of a *p–Si* module obtained with the proposed experimental system are shown. These measurements were performed under outdoor conditions with different irradiances and module temperatures. These results were obtained using two ramps.

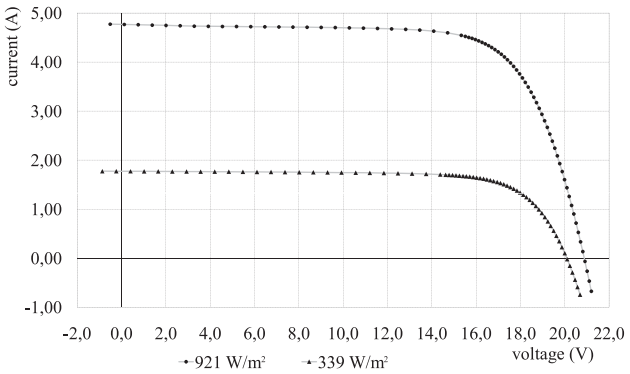

Figure 2.12: Experimental measurements of the test module under outdoor conditions for different irradiances.

Table 2.8 summarizes the main electrical characteristic parameters for these curves and the uncertainty of each value. This table also shows the irradiance and module temperature and their uncertainty when the measurements were performed. As can be seen, the measurement dispersion is not significant; it is important to note that the proposed synchronization method ensures the simultaneous measurement of I and V.

Several outdoor measurements were been consecutively carried out for the test module in order to check the accuracy of the proposed experimental system. All the measurements were obtained for the same irradiance and module temperature. These measurements are shown in Figure 2.13. The mean, maximum, minimum and variance for the fifteen curves are shown in Table 2.9.

	Curve 1		Curve 2	
	$Value$	U_{Value}	$Value$	U_{Value}
I_{SC}(A)	4.768	0.005	1.772	0.002
V_{OC}(V)	20.881	0.003	20.095	0.004
P_M(W)	71.81	0.09	26.49	0.05
I_M(A)	4.336	0.006	1.606	0.003
V_M(V)	16.560	0.004	16.489	0.004
FF(%)	72.12	0.12	74.34	0.17
G(W/m²)	921	30	339	27
T_M(°C)	40.7	1.3	39.0	1.3

Table 2.8: Estimated electrical characteristic parameters for the I–V curves in Figure 2.12 and their uncertainties.

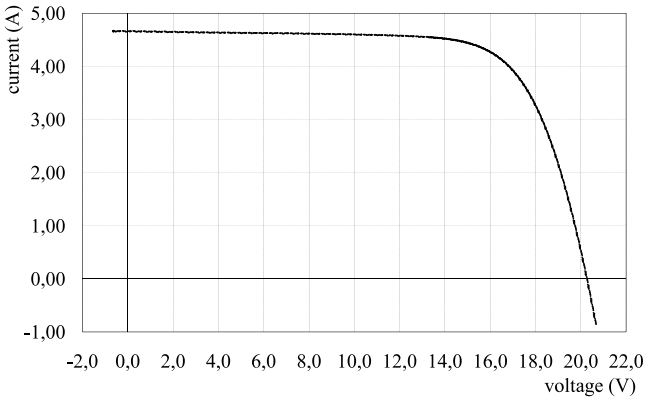

Figure 2.13: Graphics of fifteen I–V curves for the test module consecutively carried out in order to check the accuracy of the proposed experimental system.

2.8 Analysis of degradation mechanisms

An application which has been performed in the Photovoltaic Laboratory of University of Málaga is presented in this section. It has been carried out by using the system described in this chapter and its results have been published [46]. This work is related to a study on the degradation mechanisms of the PV generator installed on the roof of the laboratory after 12 years of exposure. The system has been used to measure the characteristic curve of each module in order to compare it with the measured curve at the beginning of the exposure period. Then, the correlation of the visual defects of the modules and the variation in their electrical parameters has been analysed.

	Min	Max	$Mean$	Var
I_{SC}(A)	4.652	4.668	4.660	0.00002
V_{OC}(V)	20.244	20.288	20.269	0.0001
P_M(W)	68.22	68.51	68.37	0.006
I_M(A)	4.214	4.268	4.246	0.0003
V_M(V)	16.015	16.248	16.103	0.004
FF(%)	72.30	72.46	72.38	0.00007
$G(\mathrm{W/m^2})$	930	932	930	0.4
T_M(°C)	44.6	45.1	45.0	0.02

Table 2.9: Minimum, maximum, mean and variance for the fifteen curves in Figure 2.13.

We will describe how the system has been used in order to quantify degradation looses of a crystalline silicon PV installation of 2 kWp. The photovoltaic generator under study is composed of 42 PV modules with nominal power 53 Wp. This type of module has 36 series–connected p–type mono–crystalline silicon solar cells of size 103 mm and about 300 micrometer thickness. The cells are textured and have a TiOx antireflecting coating. They are interconnected with tinned copper ribbons. The cells are encapsulated with *ethilen–vinil–acetate* (EVA) between a high transmittance flat tempered glass and a composite backsheet of Tedlar® (PVF) and polyester (PET), with a PVF/PET/PVF configuration. Each module contains two IP65 protected junction boxes with by–pass diodes in series with 24 cells. They have an anodized aluminium frame. The modules were then mounted in a horizontal configuration over an open–rack structure. The modules are facing south–west with an azimuth of 9° and an inclination of 54° from the horizontal. In a previous publication [47], the installation and the performance during the first two years of operation are described.

The main visual defects found almost in the totality of the modules are: irreversible soiling of the glass at the bottom edge of the modules, oxidation of the front metallization grid and the AR coating of the cells and localized delamination at the cell–encapsulant interface. A small percentage of the modules also showed backsheet delamination at the PVF/PET interfaces and formation of hot-spots with cell cracking and backsheet burning. Hot–spots were an isolated effect probably caused by shadows external to the installation. The impact on the module electrical performance was also not very significant.

Prior to the installation the I–V curves of all the modules were measured outdoors and converted to standard test conditions. After 12 years the

I–V curve of each module has been measured and compared to the initial measurement. Taking into account standard IEC 60904–1 [48], the following conditions were imposed to all measurements:

- Time of measurement within an hour of solar noon.
- Global irradiance in the measurement plane higher than 800 W/m^2.
- Diffuse fraction lower than 10 %.
- Maximum variation of irradiance during time of measurement lower than 1 %.
- Maximum variation of module temperature during time of measurement lower than 1 °C.
- Wind speed lower than 1 m/s.

In addition, both sets of measurements were carried out during the month of June, in 1996 and 2008 respectively, so that sunlight spectral differences can be minimized. The maximum relative uncertainty of the power measurements was 2 % at the beginning of the period under study and 1 % at the end. It is noted that the initial measurements were performed directly upon arrival of the modules, so that the initial light induced degradation of the modules will be included in the reported losses. The measurements at the start and end of the degradation period were performed under very similar meteorological conditions. All the global irradiance data lied in the interval 900–1200 W/m^2, whereas the ambient temperature was kept between 19 °C and 29 °C.

The curves were translated to standard test conditions (STC) following the *procedure 1* described in IEC 60891 [49], with the translation parameters α, β, κ and internal R_S supplied by the PV modules manufacturer. The translated curves were then fitted to a one–diode model with variable ideality factor, using the IVFIT software [50] supplied by the Energy Research Centre of the Netherlands (ECN). This allows us to estimate the values of the series (R_S) and shunt (R_{SH}) resistances for each module before and after degradation, in addition to the characteristic parameters: short–circuit current (I_{SC}), open–circuit voltage (V_{OC}), fill factor (FF) and maximum power point current (I_{M}), voltage (V_{M}) and power (P_{M}).

A statistical analysis of the characteristic parameters before and after degradation was conducted. It was observed that the data fitted well a normal distribution. It is shown that the total peak power of the installation is reduced by 11.5 % in 12 years. This corresponds mostly to a decay of

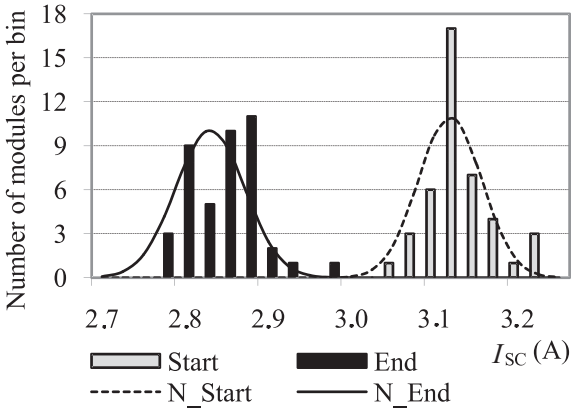

Figure 2.14: Normal distribution of I_{SC} before and after the degradation period.

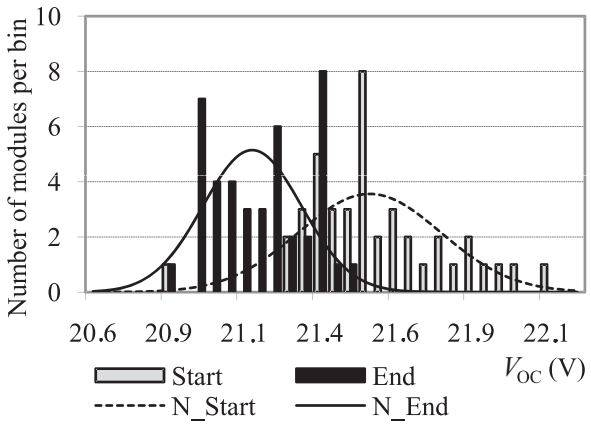

Figure 2.15: Normal distribution of V_{OC} before and after the degradation period.

9.3 % in the short–circuit current. The FF and open–circuit voltage show, on average, very little variation. The average annual degradation of the peak power is of the order of 1 %. However, if we take into account that the initial measurements of the modules were performed without preconditioning [51], it is likely that a typical initial degradation of the order of 3 % took place during the first hours of exposure to light. This leaves a 0.7 % additional loss per year during the 12 years of exposure. It is remarkable that despite the visual defects observed at the PV modules, the overall electrical performance

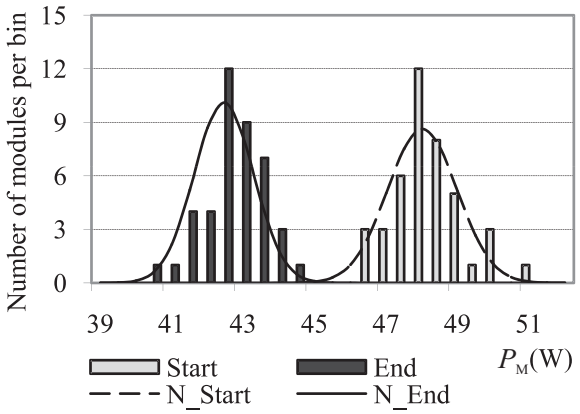

Figure 2.16: Normal distribution of P_{M} before and after the degradation period.

of the installation is still good and within the power warranty offered by the manufacturer. Figures 2.14 to 2.16 show the frequency distributions of the main electrical characteristic parameters before and after the degradation, together with the corresponding Gaussian distributions.

2.9 Conclusions

A new experimental procedure to measure the current–voltage curve of photovoltaic modules under outdoor conditions was developed. The proposed system is based on the use of an electronic load of four quadrants and two digital multimeters synchronized by a waveform generator that creates a square signal to trigger both multimeters. This synchronizing method ensures that the measuring of the voltage and current values is performed simultaneously; this could not be ensured in the previous methods using synchronization by GPIB. The control application that is running on the main computer allows the user to configure and define several experiments over different modules. Measurements are performed and stored in a database at regular intervals of time. Moreover, these measurements could be visualized and exported through a friendly web interface in a remote way. The electrical parameters of the module were estimated. An uncertainty analysis was performed. This analysis includes both errors due to the resolution and accuracy of electronic equipment, and those due to the methods used to estimate the electrical parameters.

Bibliography

[1] W. Durisch, J. Urban, and G. Smestad. Characterisation of solar cells and modules under actual operating conditions. *Renewable Energy*, 8 (1–4):359–366, 1996. doi: 10.1016/0960-1481(96)88878-1.

[2] M.J. Morgan, G. Jakovidis, and I. McLeod. An experiment to measure the I–V characteristics of a silicon solar cell. *Physics Education*, 29(4): 252–254, 1994. doi: 10.1088/0031-9120/29/4/014.

[3] A.Q. Malik and S.J.B.H. Damit. Outdoor testing of single crystal silicon solar cells. *Renewable Energy*, 28(9):1433–1445, 2003. doi: 10.1016/S0960-1481(02)00255-0.

[4] M.M. Mahmoud. Transient analysis of a pv power generator charging a capacitor for measurement of the I–V characteristics. *Renewable Energy*, 31(13):2198–2206, 2006. doi: 10.1016/j.renene.2005.09.019.

[5] E.E. Van Dyk, A.R. Gxasheka, and E.L. Meyer. Monitoring current–voltage characteristics and energy output of silicon photovoltaic modules. *Renewable Energy*, 30(3):399–411, 2005. doi: 10.1016/j.renene.2004.04.016.

[6] Y. H. Muoy, J. P. Charles, and M. Adbelkrim. Reliable and economical circuit I–V characterization solar cells. *American Journal of Physics*, 49(5):508–509, 1981. doi: 10.1119/1.12710.

[7] C.R. Osterwald. Standards, calibration and testing of PV modules and solar cells. In T. Markvart and L. Castañer, editors, *Practical Handbook of Photovoltaics: Fundamentals and Applications*, chapter IV–I, pages 791–816. Elsevier Science, Oxford (UK), 2003. ISBN 978-1-85617-390-2.

[8] T.H. Warner and C.H. Cox. A high power current–voltage curve tracer employing a capacitive load. *Solar Cells*, 7(1–2):175–181, 1982. doi: 10.1016/0379-6787(82)90102-8.

[9] P. Tzanetakis and M. Tsilis. Design, construction and comparative evaluation of two portable photovoltaic array *I–V* curve tracers. In *11th European Photovoltaic Solar Energy Conference*, pages 1359–1362, Montreux (Switzerland), 1992.

[10] F. Recart, H. Mackel, A. Cuevas, and R.A. Sinton. Simple data acquisition of the Current–Voltage and Illumination–Voltage curves of solar cells. In *4th IEEE World Conference on Photovoltaic Energy Conversion*, volume 1, pages 1215–1218, Waikoloa (HI, USA), 2006. doi: 10.1109/WCPEC.2006.279400.

[11] J. Muñoz and E. Lorenzo. Capacitive load based on IGBTs for on–site characterization of PV arrays. *Solar Energy*, 80(11):1489–1497, 2006. doi: 10.1016/j.solener.2005.09.013.

[12] *PVPM 2540C 6020C 1000C 1000C40. Peak Power Measuring Device for PV Modules . Users Manual.* PV–Engineering GmbH, Iserlohn (Germany), 2009.

[13] *DS–100C I–V Curve Tracer User Manual.* Daystar Inc, Las Cruces (NM, USA), 2006.

[14] Y. Kuai and S. Yuvarajan. An electronic load for testing photovoltaic panels. *Journal of Power Sources*, 154(1):308–313, 2006. doi: 10.1016/j.jpowsour.2005.04.016.

[15] N. Forero, J. Hernández, and G. Gordillo. Development of a monitoring system for a PV solar plant. *Energy Conversion and Management*, 47 (15–16):2329–2336, 2006. doi: 10.1016/j.enconman.2005.11.012.

[16] J. Salmon, R. Phelps, S. Michael, and H. Loomis. Solar cell measurement system for NPS Spacecraft Architecture and Technology Demonstration Satellite NPSAT1. In *17th Annual AIAA/USU Conference on Small Satellites*, Logan (UT, USA), 2003.

[17] T.A. Kattakayam, S. Khan, and K. Srinivasan. Diurnal and environmental characterization of solar photovoltaic panels using a PC–AT add on plug in card. *Solar Energy Materials and Solar Cells*, 44(1):25–36, 1996. doi: 10.1016/0927-0248(96)00012-8.

[18] E.G. Mantingh, W. Zaaiman, and H.A. Ossenbrink. Ultimate transistor electronic load for electrical performance measurement of photovoltaic devices using pulsed solar simulators. In *1st IEEE World Conference*

on Photovoltaic Energy Conversion, volume 1, pages 871–873, Waikoloa (HI, USA), 1994. doi: 10.1109/WCPEC.1994.520099.

[19] H. Matsuo and F. Kurokawa. New solar cell power supply system using a boost type bidirectinal DC–DC converter. *IEEE Transactions on Industrial Electronics*, 31(1):51–55, 1984. doi: 10.1109/TIE.1984.350020.

[20] P. Sanchis, J. López, A. Ursúa, and L. Marroyo. Electronic controlled device for the analysis and design of photovoltaic systems. *IEEE Power Electronics Letters*, 3(2):57–62, 2005. doi: 10.1109/LPEL.2005.851314.

[21] M. Kazerani. A High–Performance controllable DC load. In *IEEE International Symposium on Industrial Electronics*, pages 1015–1020, Vigo (Spain), 2007. doi: 10.1109/ISIE.2007.4374737.

[22] E. Durán, J.M. Andújar, J. Galán, and M. Sidrach–de–Cardona. Methodology and experimental system for measuring and displaying DC–DC characteristic curves of PV facilities. *Progress in Photovoltaics: Research and Applications*, 17(8):574–586, 2009. doi: 10.1002/pip.909.

[23] M.G. Guvench, C. Gurcan, K. Durgin, and D. MacDonald. Solar simulator and I–V measurement system for large area solar cell testing. In *American Society for Engineering Education Annual Conference & Exposition*, Salt Lake City (UT, USA), 2004.

[24] F. Almonacid, C. Rus, L. Hontoria, and F.J. Muñoz. Characterisation of PV CIS module by artificial neural networks. A comparative study with other methods. *Renewable Energy*, 35(5):973–980, 2010. doi: 10.1016/j.renene.2009.11.018.

[25] K.A. Emery. Measurement and characterization of solar cells and modules. In A. Luque and S. Hegedus, editors, *Handbook of Photovoltaic Science and Engineering*, chapter 16, pages 701–747. Wiley, New York (NY, USA), 2003. ISBN 978-0-471-49196-5.

[26] L.A. Hecktheuer, A. Krenzinger, and C. W. M. Prieb. Methodology for photovoltaic modules characterization and shading effects analysis. *Journal of the Brazilian Society of Mechanical Sciences*, 24(1):26–32, 2002. doi: 10.1590/S0100-73862002000100004.

[27] M. A. De Blas, J. L. Torres, E. Prieto, and A. García. Selecting a suitable model for characterizing photovoltaic devices. *Renewable Energy*, 25(3): 371–380, 2002. doi: 10.1016/S0960-1481(01)00056-8.

[28] J. Fernández–Reche, I. Cañadas, M. Sánchez, J. Ballestrín, L. Yebra, R. Monterreal, J. Rodríguez, G. García, M. Alonso, and F. Chenlo. PSA Solar furnace: A facility for testing PV cells under concentrated solar radiation. *Solar Energy Materials and Solar Cells*, 90(15):2480–2488, 2006. doi: 10.1016/j.solmat.2006.03.030.

[29] F. Granek and T. Zdanowicz. Advanced system for calibration and characterization of solar cells. *Opto Electronics Review*, 12(1):57–67, 2004.

[30] R.C. Powell, R. Sasala, G. Rich, M. Steele, K. Bihn, N. Reiter, S. Cox, and G. Dorer. Stability testing of CdTe/CdS thin–film photovoltaic modules. In *25th IEEE Photovoltaic Specialists Conference*, pages 785–788, Washington (DC, USA), 1996. doi: 10.1109/PVSC.1996.564245.

[31] *Operator's Manual. BOP 1000W High Power Bipolar Power Supply. Model BOP 100–10MG*. Kepco Inc, Flushing (NY, USA), 2005.

[32] M.C. Alonso–García and J.M. Ruiz. Analysis and modelling the reverse characteristic of photovoltaic cells. *Solar Energy Materials and Solar Cells*, 90(7–8):1105–1120, 2006. doi: 10.1016/j.solmat.2005.06.006.

[33] *Agilent 34410A/11A 6 1/2 Digit Multimeter User's Manual*. Agilent Technologies, Santa Clara (CA, USA), 4th edition, 2007.

[34] *CMA series albedometer and CMP series pyranometer. Instruction Manual*. Zipp & Zonen, Delft (The Netherlands), 2006.

[35] *Compact FieldPoint cFP–21xx and cFP–BP–x User Manual*. National Instruments Corporation, Austin (TX, USA), 2005.

[36] F. Iwanitz and J. Lange. OPC–Openness, Productivity, and Connectivity. In Richard Zurawski, editor, *The Industrial Information Technology Handbook*, chapter 62. CRC Press, Danvers (MA, USA), 2005. ISBN 978-0-8493-1985-3.

[37] J. Greenspan and B. Bulger. *Mysql/PHP Database Applications*. M&T Books, Foster City (CA, USA), 2001. ISBN 978-0-7645-3537-6.

[38] ISO–GUM. *Guide 98–3, Evaluation of measurement data – Part 3: Guide to the expression of uncertainty in measurement*. 2008.

[39] B.N. Taylor and C.E. Kuyatt. NIST Technical Note 1297. Guidelines for evaluating and expressing the uncertainty of NIST measurement results. Technical report, National Institute of Standards and Technology, Gaithersburg (MD, USA), 1994.

[40] K. Whitfield and C.R. Osterwald. Procedure for determining the uncertainty of photovoltaic module outdoor electrical performance. *Progress in Photovoltaics: Research and Applications*, 9(2):87–102, 2001. doi: 10.1002/pip.356.

[41] *FP–AI–112 and cFP–AI–112, FieldPoint Operating Instructions*. National Instruments Corporation, Austin (TX, USA), 2004.

[42] M.G. Kratzenberg, H.G. Beyer, S. Colle, and A. Albertazzi. Uncertainty calculations in pyranometer measurements and applications. In *ASME International Solar Energy Conference*, pages 689–699, Denver (CO, USA), 2006.

[43] I. Reda and A. Andreas. Solar position algorithm for solar radiation applications. Technical Report NREL/TP–560–34302, National Renewable Energy Laboratory (NREL), Golden (CO, USA), 2008.

[44] *FP–RTD–124 and cFP–RTD–124, FieldPoint Operating Instructions*. National Instruments Corporation, Austin (TX, USA), 2002.

[45] IEC 60751. *Industrial platinum resistance thermometers and platinum temperature sensors*. International Electrotechnical Commission, Geneva (Switzerland), 2nd edition, 2008. ISBN 978-2-8318-9849-0.

[46] P. Sánchez–Friera, M. Piliougine, J. Peláez, J. Carretero, and M. Sidrach–de–Cardona. Analysis of degradation mechanisms of crystalline silicon PV modules after 12 years of operation in Southern Europe. *Progress in Photovoltaics: Research and Applications*, 2011. doi: 10.1002/pip.1083.

[47] M. Sidrach–de–Cardona and L. Mora–López. Performance analysis of a grid–connected photovoltaic system. *Energy*, 24(2):93–102, 1999. doi: 10.1016/S0360-5442(98)00084-X.

[48] IEC 60904–1. *Photovoltaic devices – Part 1: Measurement of photovoltaic current voltage characteristics*. International Electrotechnical Commission, Geneva (Switzerland), 2nd edition, 2006.

[49] IEC 60891. *Procedures for temperature and irradiance corrections to measure I–V characteristics of crystalline silicon photovoltaic devices.* International Electrotechnical Commission, Geneva (Switzerland), 2nd edition, 2009. ISBN 978-2-88910-316-4.

[50] A.R. Burgers, J.A. Eikelboom, A. Schonecker, and W.C. Sinke. Improved treatment of the strongly varying slope in fitting solar cell *I–V* curves. In *25th IEEE Photovoltaic Specialists Conference*, pages 569–572, Washington (DC, USA), 1996. doi: 10.1109/PVSC.1996.564070.

[51] D. Chianese, A. Realini, N. Cereghetti, S.Rezzonico, E. Burà, G. Friesen, and A. Bernasconi. Analysis of weathered c–Si PV modules. In *3rd World Conference on Photovoltaic Energy Conversion*, volume 3, pages 2922–2926, Osaka (Japan), 2003.

Chapter 3

I–V exchange file format

3.1 Introduction

In this chapter, a standard is defined to format the recorded data measured from photovoltaic devices, such as cells, modules and arrays. The objective is to define a unified and accepted methodology that facilitates *communication* among different laboratories and enterprises. This could be very useful to enable the exchange of data among different stakeholders interested in this type of measurements, namely, manufacturers, laboratories and researchers, among others. The goal of this chapter is to define a file format for *I–V* curve data which can be easily exchanged. Despite there being numerous laboratories where photovoltaic devices are measured, there has no far been widely accepted proposal to systematize the way in which data is stored. Each laboratory defines its own measurement storage format, which makes it impossible to easily exchange data and results in order to compare the values obtained by different laboratories. This fact implies an extra cost in human resources in order to adapt the output files from different sources.

For several years now, work has begun on facilitating the information exchange and the validation of the measurement protocols of laboratories and institutions dedicated to characterizing photovoltaic devices. Until very recently, there was no commonly accepted protocol regarding the parameters which had to be measured for each device and their traceability. Aware of this problem, the European Commission Joint Research Centre, together with its partners in the PERFORMANCE FP6 Integrated Project (Sub-Project 1: Traceable Performance Measurements of PV Devices), proposed in April 2010 the *Guidelines for PV Power Measurement in Industry* [1]. As suggested in this guide, the proposed recommendations could contribute to the goal of using a comprehensive organization of all type of data recorded in

photovoltaic laboratories, such as the I–V data, temperature and irradiance values, module identification data, reference device and system setting for each measurement. Therefore, these are a set of practical recommendations for module manufacturers seeking to harmonize measurement methods and to improve the quality of their power measurements.

The use of standard formats for storing information makes easy to share this data. This standardization is also essential to enable the development of programs to process this information with minimal effort and using existent tools and libraries. One format is not only usually proposed for storing the data, but the technology is also facilitated that enables them to be accessed and processed. Some of the most used technology data are describing in the following lines.

- *XML* (eXtensible Markup Language):

  This is probably the most common language for storing and accessing data. It has been used in many different projects as it meets the information exchange and retrieval requirements. For instance:

  - In Sormaz et al. [2], an efficient model for communications between CAD, CAPP, and CAM applications in distributed manufacturing planning environments has been developed using XML–based representation for product data required for process planning and the process model also uses XML representation of data required for scheduling and control.
  - QuakeML is an XML–based data exchange standard for seismology, [3]. It was developed with the aim of helping to consolidate existing data formats for applications in statistical seismology, as well as setting a cutting-edge and community–agreed standard to foster interoperability of distributed infrastructures.
  - In Poorazizi and Alesheikh [4], an environmental monitoring application based on a mashup architecture is designed and developed. The application uses Google Maps API (Application Programming Interface), Web GIServices (Geospatial Information Services), and AJAX (Asynchronous JavaScript and XML) to disseminate real–time air quality information through the Web.

- *Hierarchical Data Format* (HDF, current version HDF5):

  HDF files are self–describing and allow users to specify complex data relationships and dependencies. With this format, the data are stored

in binary files organized for high–performance access, using a machine–independent, self–describing format. HDF files can contain binary data (in many representations) and allow direct access to parts of the file without first parsing the entire content. It is used for different enterprises and research centres in different fields such as: in satellite meteorology, oceanography, groundwater hydrology, medicine, etc. ; see for instance, [5], [6], [7], [8] and [9]. Bennett and Robertson [10] propose to integrate and use both XML and HDF5 for data archiving and this offers a good solution for data providers and consumers to share information for computational and scientific purposes.

- *Extensible Data Model and Format* (XDMF):

  This integrated approach is a new flexible data exchange mechanism for high–performance computing (HPC), known as the eXtensible Data Model and Format (XDMF). XDMF is part of a larger effort known as the *Interdisciplinary Computing Environment* (ICE). ICE provides computational engines with the data management, visualizations, and user interface tools necessary to exist in a modern computing environment. Instead of imposing a new programming paradigm on HPC codes, XDMF uses the existing concept of file I/O for distributed coordination. XDMF incorporates Network Distributed Global Memory (NDGM), Hierarchical Data Format version 5 (HDF5), and eXtensible Markup Language (XML) to provide a flexible yet efficient data exchange mechanism [11].

- *Measurement Data Format* (MDF):

  It is used in the automotive industry. The MDF allows an efficient storage of measurement data. MDF is a binary file format for measurement data. It was developed in 1991 by Vector and Robert Bosch GmbH.

- *Network Common Data Form* (netCDF):

  This library also offers a flexible data model and machine independence similar to HDF5. The most recent version, netCDF-4, has adopted HDF5 as its intermediate layer.

There is a prior attempt in order to develop a format data file based on XML oriented to store and monitor information from photovoltaic plants. In Kolodenny et al. [12], a universal data scheme called PVML is proposed, allowing analysis of the performance of a PV system of any type and size in order to detect faults and underperformance on PV plants. In this work

several kinds of user roles are identified depending on the actions they may want to perform: owner, technician, data logger system and scientist. All of them interact with the platform using PVML language, but whereas human users access this information through a web interface, machine users and applications process the XML files straightforward. For example, the scientist analyses available data with the aim of searching for correlations between not only measured data but also calculated parameters using specialized software that could open XML files as input. This work could be view as an extension of the approach given by a SCADA giving special importance to historical stored data in order to monitor the plant along a period and build an operative model of it. In addition to the different services that can be implemented the data exchange between all users is described. In a second work, Prorok et al. [13], the entities of the format are described in more detail, including structures for storing *I–V* curves and solar spectrum curves.

3.2 A brief survey on XML and XML Schema

There are two main approaches for storing data in order to enable the interchange of information. On the one hand, if the aim is to store or interchange many *I–V* measurements, we need a compressed file format in order to store the maximum number of measurements in the minimum space, thus saving disk space. So in this case the readability of the file format is not important (a binary format could be a good alternative); the measured and calculated values (and their uncertainties) could be expressed using a floating point format. On the other hand, if the aim is to achieve a universal format, readability is more important that the file size. As nowadays the storage capacity and the transmission speed over the Internet are very high, we think that the readability of the file format is very important and it must be taken into account.

In order to further develop a standard, we propose an XML–based format to describe and store the recorded values and the necessary additional information from the measurement of photovoltaic devices. XML stands for the eXtensible Markup Language, developed to overcome the limitations of HTML. As it has been pointed out in [14], *this standard attempts to highlight an unprecedented effort by a consortium of organizations and companies to create an information framework for the 21st century. XML itself is an attempt to rein in the uncontrolled development of competing technologies and proprietary languages.*

Both HTML and XML are based on the concept of markup. Markup is a special code embedded within the document which stores the information

required for electronic processing (such as font name, size or boldness). It facilitates the treatment of the pieces of text in a document with programs. XML was created to solve the problems with the use and creation of new tags in HTML, especially as the new tags that have needed to be added in HTML are very specialized and each application requires different tags. As there are no predefined tags in XML, it is easy to create the tags that each application requires without modifying the language. Moreover, HTML was developed for facilitating separating the contents from the formats, that is, it focuses on the format and appearance of the document. By contrast, XML focuses on the structure of the document and it is not only a solution for publishing web pages but also it is very useful to exchange information. In fact, XML is widely used as a valid format for data exchange among applications. XML is easy to read by parse programs. The files written in XML are character–oriented files, compared to the binary file formats that require the structure of the files to be defined for their content to be read. One additional advantage of XML is that it is an open standard, and is supported by a large range of products, libraries and applications. It is therefore easy to find support, store and exchange XML documents, even by non–computer specialists. In addition to these reasons, the use of XML is proposed in this thesis as it is a flexible way that accommodates the structure of specific applications.

XML specification is based on the concept of *element*. As stated in [14], each element has a name and content. The content of an element is delimited by special markups known as start tag and end tag. The name appears in the start tag and also in the end tag. It is possible to attach additional information to elements in the form of attributes including them in the start tag. Element content is not limited to text; elements can contain other elements that in turn can contain text or elements and so on. Therefore, an XML document is a tree of elements. The definitions of the tags and their relationships are provided by a set of rules that specify the tags that can be used and what they can contain. A well–formed XML document must follow specific syntax rules common for all XML documents. Moreover, the XML document must comply with a specific structure in order to be considered a valid document and to be useful for the application for which it has been created.

In the past, DTDs (*Document Type Definition*) provide a mechanism to describe the content and structure of the XML file. However, other languages have been developed that overcome the DTD limitations. One of the most common is the *XML Schema* (sometimes referred to as XSchema): it is also well–formed XML and provides much greater control over data types and patterns that DTD syntax. XML Schema allows the description of every object (element, attribute, and so on) that can appear in the XML docu-

ment. In the case of the elements, the list of children that are acceptable in that element and whether and how these children can be repeated need to be provided for each one. A list of valid attributes, giving for each attribute its name, its type and its default value need to be defined for each element. There are applications and libraries in order to ensure that an XML document follows the structure described in its associated XSD (*XML Schema Definition*). Moreover, there are graphical tools to draw a visual tree from the description provided by an XSD file. In Zhanga et al. [15], the use of XML and standard schemes in different areas is analysed.

This thesis proposes an XSD to be used to define the structure of valid XMLs files to format some type of data and information in photovoltaic laboratories; specifically we propose the XSD to format data related to *I–V* curves. This definition can easily be expanded to address other needs in photovoltaic laboratories. The idea consists of offering this XSD to the photovoltaic community with the aim that it should be used in all situations where an *I–V* curve is measured or used to perform calculations over it, such as when translating it to STC conditions or parameters of a module need to be determined using this measurement data. This proposal has been used in the experimental measurements used in Chapter 5 and that have been recorded in the Solar Energy Photovoltaic Laboratory of the Department of Applied Physics II at the University of Malaga.

3.3 Photovoltaic device data

With respect to the measurement equipment and software used for photovoltaic devices, there are many *I–V* curve tracer systems from different manufactures and research laboratories. There are applications that take an *I–V* curve measurement and extract some electrical parameters of the PV device from the data or translate the *I–V* measurement curve to other irradiance and temperature conditions using the methods described in the standard IEC 60891 [16] or in the literature (sometimes the own control software of the *I–V* curve tracer system includes these functionalities). In many conferences and journals, papers can be found consisting of round–robin tests over several commercial modules measured by a set of selected research and calibration laboratories in order to perform comparative studies between different measuring methods; for example Herrmann et al. [17]. In all these cases, the need for a standardized format for *I–V* curve data is clearly evident. This opens up away for experimental *I–V* curve interchange and saves a great deal of time and effort when adapting and converting all the heterogeneous data files.

Most I–V curve tracers store the result of the measurements using an ASCII file with a specific ad–hoc format. The measured magnitudes and the calculated parameters are fixed beforehand by the control software programmer according to the application requirements. Hence, it is not possible to interchange files from different I–V tracers as each one is using its specific format to store the characteristic curves. Comparing the measurement from different I–V curve tracers is a very difficult task, as it requires a prior step consisting of converting each file to a unique format.

Before definining the format, an analysis must be performed in order to determine the data needs, taking into account the different requirements of the various stakeholders. This step is critical to the success of achieving a useful and widely accepted format. The data needed to be stored in the measurement of photovoltaic devices are the following:

- Standard IEC 60904–1 [18] states to generate a report of each I–V curve measurement. Therefore, the proposed format must contain enough information to generate the report. This report has to include specific information such as:
  - Name and address of the laboratory
  - Name and address of the client
  - Description and identification of the specimen (PV module)
  - Description of the test environment (natural or simulated sunlight)
  - Date of receipt of PV module and measurement date
  - Description and identification of the method for temperature and irradiance correction of the measured characteristic
  - Statement of the estimated uncertainty of the results
  - A signature, title and identification of the person(s) accepting responsibility of the content of the report with date of issue
- Measured electrical parameters:
  - Short–circuit current I_{SC} (A, mA)
  - Open–circuit voltage V_{OC} (V, mV)
  - Maximum power P_{M} (W)
  - Maximum power current I_{M} (A, mA)
  - Maximum power voltage V_{M} (V, mV)

  - Fill factor FF (%)
  - Energy conversion efficiency η (%)
  - Ideality factor m (dimensionless)
  - Series resistance R_S (Ω)
  - Shunt resistance R_{SH} (Ω)

- Description of the specimen
  - Type of specimen: module, cell, string.
  - In cell case:
    - Manufacturer
    - Model
    - Nominal electric parameters at STC
      - Short–circuit current I_{SC} (A, mA)
      - Open–circuit voltage V_{OC} (V, mV)
      - Maximum power P_{M} (W)
      - Maximum power current I_{M} (A, mA)
      - Maximum power voltage V_{M} (V, mV)
      - Fill factor FF (%)
    - Cell dimensions (height $\times$ width $\times$ depth)
    - Cell technology identification: m–Si, p–Si, a–Si ...
  - In module case:
    - Manufacturer
    - Model
    - Serial number
    - Nominal electric parameters at STC
      - Short–circuit current I_{SC} (A, mA)
      - Open–circuit voltage V_{OC} (V, mV)
      - Maximum power P_{M} (W)
      - Maximum power current I_{M} (A, mA)
      - Maximum power voltage V_{M} (V, mV)
      - Fill factor FF (%)
    - Module dimensions (height $\times$ width $\times$ depth)
    - Number of cells in series/parallel
    - Cell description

  - In string case:
    - Module description
    - Nominal electric parameters of the string at STC
      - Short–circuit current I_{SC} (A, mA)
      - Open–circuit voltage V_{OC} (V, mV)
      - Maximum power P_M (W)
      - Maximum power current I_M (A, mA)
      - Maximum power voltage V_M (V, mV)
      - Fill factor FF (%)
    - Number of modules in series/parallel

- Depending whether the measurement has been taken indoors or outdoors, specific information shall be stored in each case:
  - If the measurement has been taken indoors, information about the solar simulator shall be provided.
  - If the measurement has been taken outdoors, localization shall be provided
    - Latitude
    - Longitude
    - Altitude
    - Slope or inclination
    - Rotation or orientation

- Meteorological and solar position parameters
  - Date and time
  - Azimuth angle
  - Zenith angle
  - Angle of incidence
  - Primary irradiance value
  - Other irradiance values
  - PV device temperature(s)
  - Wind speed and direction
  - Air temperature
  - Air humidity

  - Atmospheric pressure

- Solar spectral distribution data: If the solar spectrum has been measured, a list of points, each one formed by a pair of values of wavelength (nm) and spectral irradiance (Wm^{-2}/nm).

- Information about the measurement equipment could be provided.

- If the *I–V* curve has been translated to STC or other conditions:

  - The measured *I–V* curve and the translated curve(s) will be stored.
  - The method used to translate the *I–V* curve must be described.
  - For each specimen, the used parameters (temperature coefficients, series resistance ...) must be provided.

- For each *I–V* pair:

  - Voltage value at this point
  - Current value at this point
  - *G* irradiance at this measured *I–V* pair (optional)
  - Power associated to each measured *I–V* pair (optional)

3.4 Model Implementation

Taking into account all the information requirements listed in section 3.3, we will present the definition of the entities needed to be included in the XSD in order to model the different pieces of information that are involved in the measuring and manipulating of *I–V* curves. For each entity, we first discuss the most suitable structure and a graphic with a tree is shown where each child represents a possible nested entity. The associated code is presented as a single XSD file in Appendix A. This format is proposed as a standard to be followed by all PV community.

- *measurement-type*

  We first start by defining some XML Schema complex types that will be useful in order to simplify the definitions of the entities. According to ISO–GUM [19], every measurement could be stated with its associated uncertainty, also giving the coverage factor and the confidence level (when not stated, they are taken to be 2 and 95 % respectively). Therefore, it could be convenient to define a complex type

called *measurement-type* composed by a mandatory element *value* and an optional element *uncertainty*, both of them of double type. The *uncertainty* entity could have *coverage* and *confidence* as optional attributes in order to indicate values other than 2 and 95 %. Figure 3.1 shows a tree representation of this user–defined complex type.

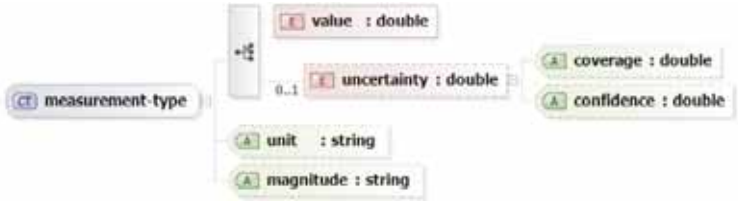

Figure 3.1: Tree representing XML complex type called *measurement-type*.

- *iv-pair-type* and *iv-array-type*

  This XML complex type is defined in order to represent each point of an I–V curve. Basically, an I–V pair has two components: a voltage measurement and a current measurement. For each pair it is possible to precalculate and store the associated power value in order to accelerate further processing over this curve. In some research laboratories, the irradiance incident on the device surface at each point of the I–V curve is also acquired. According to ISO–GUM [19], each measurement (voltage, current, irradiance ...) could be stated with its associated uncertainty giving also the coverage factor and the confidence level. Figure 3.2 shows a tree with the nested structure for the XML complex type used to model an I–V pair. Note that *voltage* and *current* are defined as mandatory entities whereas *power* and *irradiance* are defined as optional entities.

  The main concept we want to model is the I–V curve. The type called *iv-array-curve* is defined to represent the list of points of an I–V curve. Each I–V curve could be considered as an ordered list (with a variable number of items) of I–V pairs. Figure 3.3 shows the structure for the XML complex type used to model an I–V curve as a list of I–V pairs.

- *measurement-list-type*

  Always an I–V curve is measured the conditions at the time of measurement are acquired. In general, the irradiance at the plane of the module and the cell temperature are mandatory, but there are other many meteorological parameters that could be also taken into account, such as air temperature, relative humidity, atmospheric pressure ...

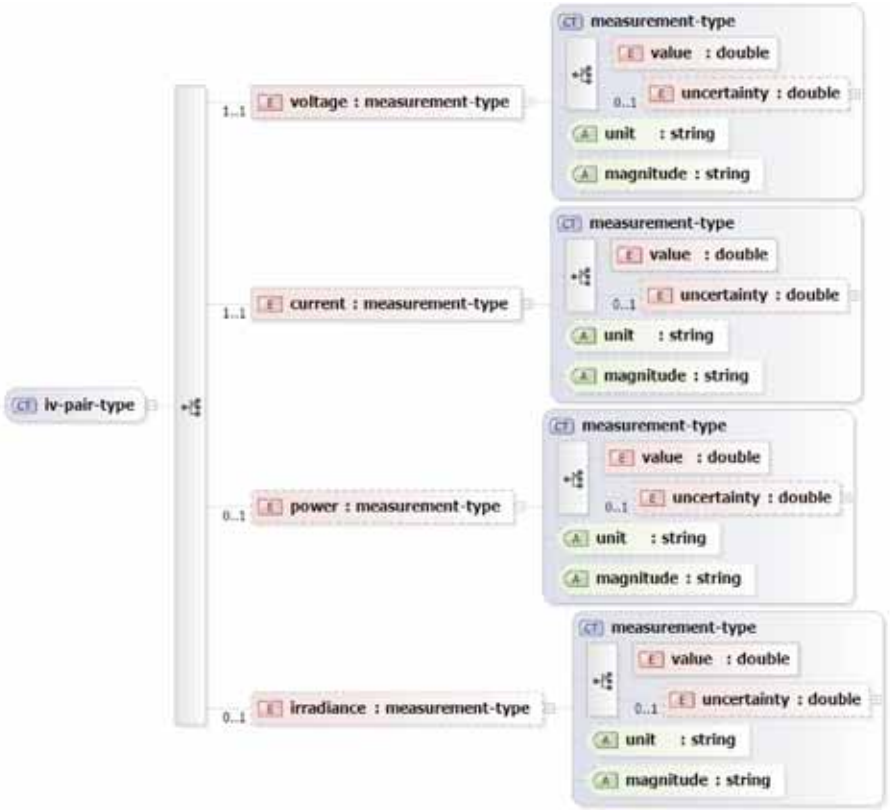

Figure 3.2: Scheme of the XML type for representing each I–V pair.

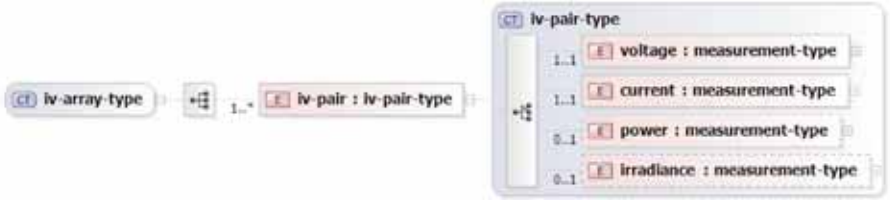

Figure 3.3: Scheme of the complex type *ivarray-type*.

These parameters might differ from one application to another and we must give a way to store them with flexibility. Instead of defining a fixed structure to store each meteorological parameter cited in previous section, a generic solution is proposed: a variable list of measures must be provided using the XML complex type called *measurement-list-type* (see Figure 3.4)

- *spectrum-point-type* and *spectrum-type*

  In addition to the measurement of the I–V curve and meteorological

Figure 3.4: Complex type for representing a list of meteorological measurements.

parameters, it is possible to measure the solar spectrum of the incident light. The solar spectrum is given by the spectroradiometer as an ordered list of points, each one composed by two values: wavelength and spectral irradiance at that wavelength value. The points of the solar spectrum are defined as it can be seen in Figure 3.5.

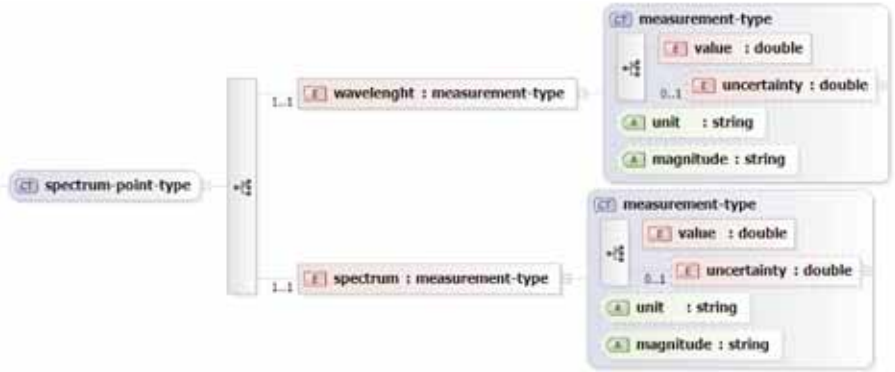

Figure 3.5: Tree representing XML complex type called *spectrum-point-type*.

Finally, the whole solar spectrum is modelled as an ordered list of points defined by the previous scheme. Figure 3.6 shows the structure associated to this spectrum–type.

Figure 3.6: A spectrum as an ordered list of spectrum points.

- *electrical-parameters-type*

  From the list of points of an I–V curve it is necessary to calculate the main electrical parameters of the module under the conditions of measurement. Mainly, these are I_{SC}, V_{OC}, P_M, I_M, V_M, the efficiency of

the specimen, the ideality factor and the series and shunt resistances. However, it is possible to calculate additional parameters, so the standard has to support this possibility. In Figure 3.7 is represented the structure of a complex XML type called *electrical-parameters-type* as an aggregation of different parameters. Note that in order to take into account additional parameters the entity *parameter-list* has been included at the end of this aggregation. Every additional parameter must be expressed as an element of this list, specifying its unit and magnitude.

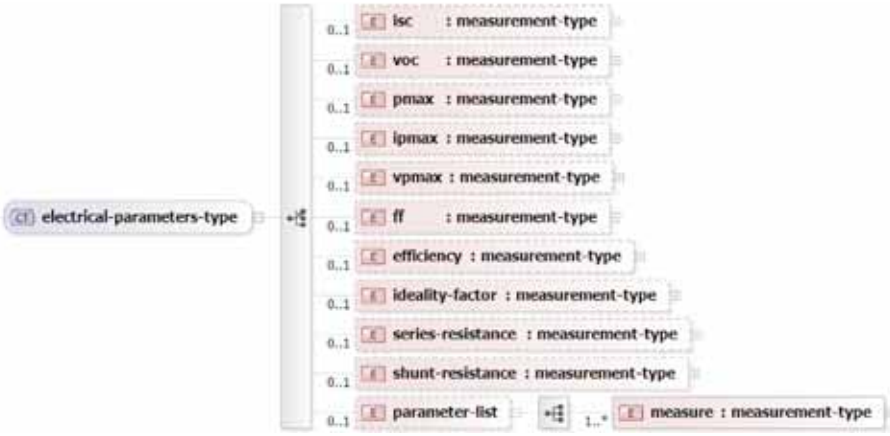

Figure 3.7: Main electrical parameters stored using *electrical-parameters-type*.

- *measured-curve-type* and *corrected-curve-type*

  At this point, we must define two types of I–V curves: the measured curves and the corrected curves. Both of them have an array of I–V points and the values of the electrical parameters. The measured curve must include the meteorological conditions at the time of measurement (and optionally the solar spectrum); the corrected curve only must include the new conditions and the method used in order to translate the I–V points of the curve. Figures 3.8 and 3.9 show the schemes associated to the complex XML types *measured-curve-type* and *corrected-curve-type* respectively.

- *iv-curve-type*

  The measured I–V curves are acquired straight from the measurement equipments, whereas the corrected I–V curves are the result of the application of an I–V translation method to a measured I–V curve. Therefore, every corrected I–V curve must be always referred to a measured

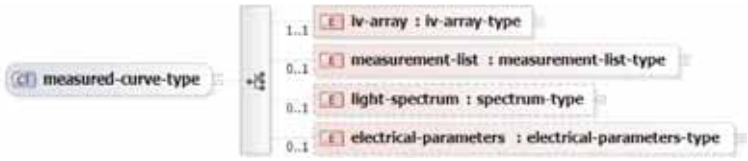

Figure 3.8: Scheme of the complex type denominated *measured-curve-type*.

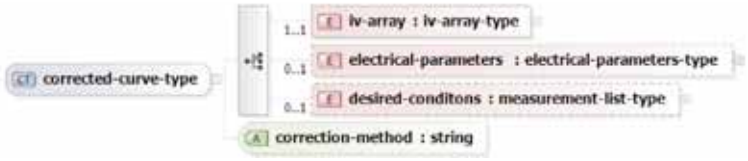

Figure 3.9: Scheme associated to *corrected-curve-type*.

I–V curve. In order to express this relationship between a corrected I–V curve and its associated measured I–V curve, we define an I–V curve as the aggregation of a unique measured I–V curve with several optional corrected I–V curves (the same measured I–V curve could be corrected by different translation methods). Therefore, the scheme used to model an I–V curve is depicted in Figure 3.10. It could be seen that an I–V curve must include a measured I–V curve and optionally one or more corrected I–V curves (implemented as a list of corrected I–V curves). Note that each I–V curve has a date–time stamp indicating the point in time of the measurement.

Figure 3.10: Scheme associated to *iv-curve-type*.

- *specimen-description*

  Now we will define the XML complex type that will be used in order to store the description of the photovoltaic device to be measured. First, about the kind of the photovoltaic device, there are three alternatives: it could be a single *cell*, a photovoltaic *module*, or even a group of modules connected between them as a *string*. Note in the Figure 3.11 that cell, module and string are different options for a PV device description (XML allows a definition of an entity as an alternative of several options).

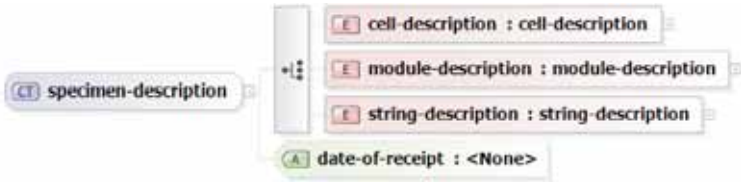

Figure 3.11: Scheme associated to *specimen-description*.

- *cell-description*, *module-description* and *string-description*

  For each measured cell it is necessary to store several pieces of information, such as its technology, dimensions, nominal electrical parameters, manufacturer, etc. Figure 3.12 shows the subentities which must be given to describe a cell.

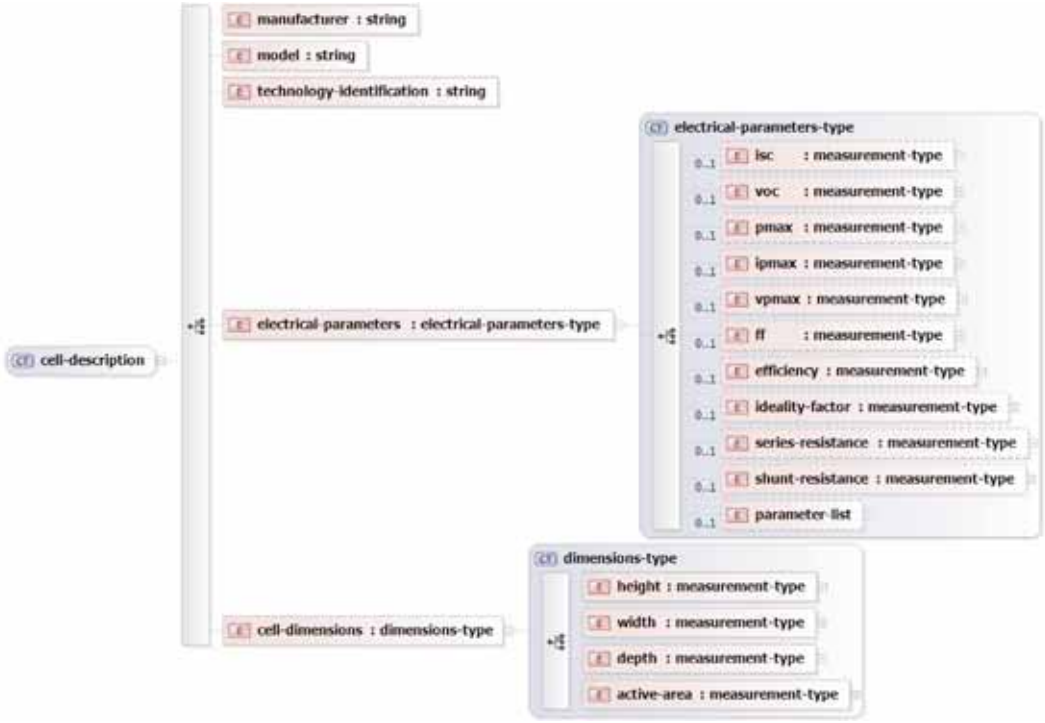

Figure 3.12: Information to be stored for each measured cell.

In the same way, with the complex types *module-description* (Figure 3.13) and *string-description* (Figure 3.14) we provide the syntax in order to represent generic information about a module or a string. Note that for each case the pieces of information could be different.

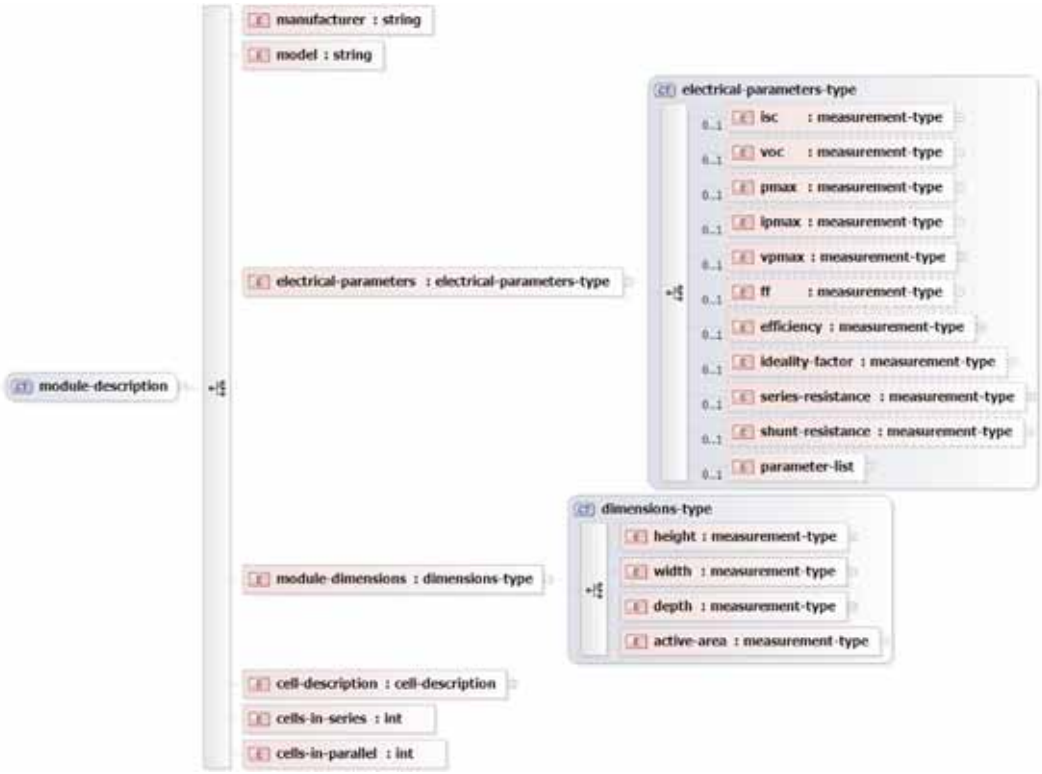

Figure 3.13: Information to be stored for each measured module.

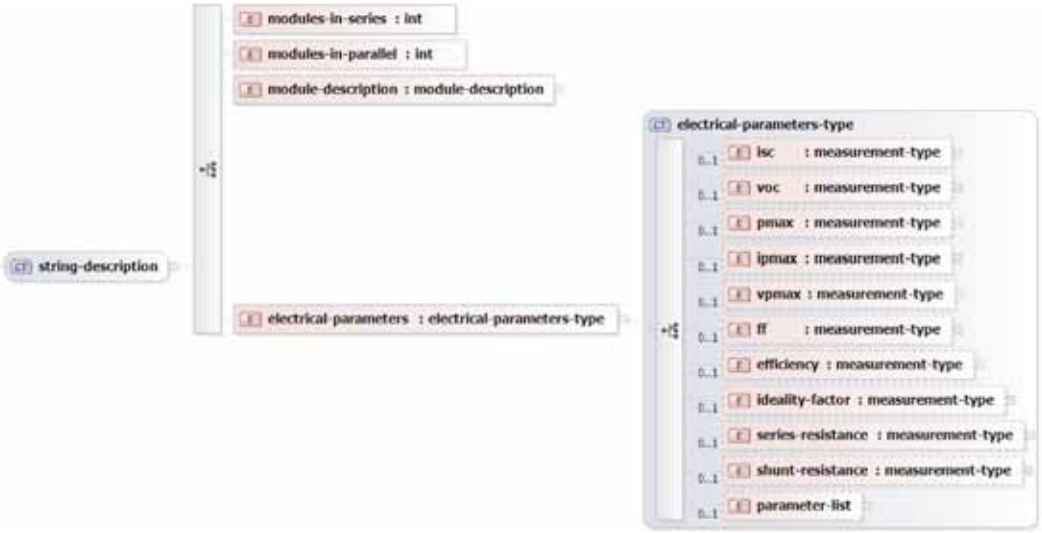

Figure 3.14: Information to be stored for each measured string.

- *environment-type*

  There are some minor details related with the environment in which the measurements are acquired that must also be stored. This information depends on where the measures have been taken: indoors or outdoors. For example, if the measure has been taken outdoors, the geographical coordinates of the laboratory must be provided. Figure 3.15 shows the scheme of the complex type that could be used to describe the environment.

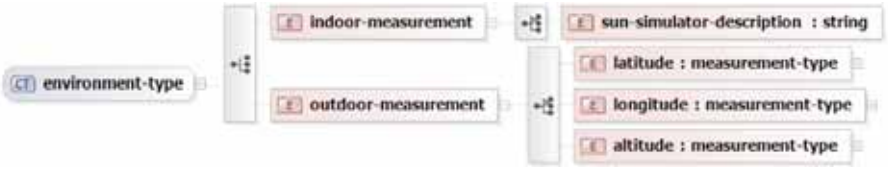

Figure 3.15: XML complex type to store information about the measurement environment.

- *administrative-information*

  Finally, some administrative issues must be stored, specially in order to fill the reports required by the standard IEC 60904–1 [18]. This data is related to the identification and address of the laboratory and the client and other administrative information of interest. In Figure 3.16 the complex type *administrative-information* is depicted.

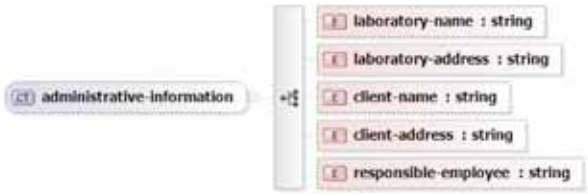

Figure 3.16: Complex type to store administrative issues.

3.5 Conclusions

In this chapter an XML Scheme to format the data recorded in photovoltaic laboratories has been proposed. This format can contribute to the standardization of the data used for characterizing the measurements acquired by different laboratories in order to facilitate data exchange between them. Therefore, it is possible to perform analyses and round–robin tests among several laboratories using common datasets. In addition, developed software by different research groups could be shared. A hierarchical structure has been developed for the elements and parameters usually used in the measurements of photovoltaic devices.

Bibliography

[1] *Guidelines for PV Power Measurements in Industry*. JRC Scientific and Technical Reports (EUR collection). Publications Office of the European Union, 2010.

[2] D.N. Sormaz, J. Arumugam, R.S. Harihara, C. Patel, and N. Neerukonda. Integration of product design, process planning, scheduling, and FMS control using XML data representation. *Robotics and Computer–Integrated Manufacturing*, 26(6):583–595, 2010. doi: 10.1016/j.rcim.2010.07.014.

[3] D. Schorlemmer, F. Euchner, P. Kaestli, J. Saul Joachim, and QuakeML Working Grp. QuakeML: status of the XML–based seismological data exchange format. *Annals of Geophysics*, 54(1):59–65, 2011. doi: 10.4401/ag-4874.

[4] M.E. Poorazizi and A.A. Alesheikh. Monitoring real–time environmental information using Web 2.0 and GIServices technology. *International Journal of Civil Engineering*, 9(1):63–70, 2011.

[5] S.K. Sahoo and G. Agrawal. Supporting XML based high–level abstractions on HDF5 datasets: A case study in automatic data virtualization. In *Languages and Compilers for High Performance Computing*, volume 3602 of *Lecture Notes in Computer Science*, pages 299–318, Berlin (Germany), 2005. Springer–Verlag.

[6] C.A. Steed, J.E. Braud, and K.A. Koehler. VGRID: A generic, dynamic HDF5 storage model for georeferenced, grid data. In *OCEANS 2002 Marine Technol Soc. and IEEE Ocean Engn. Soc.*, volume 1–4, pages 900–907, Biloxi (MS, USA), 2002. IEEE. doi: 10.1109/OCEANS.2002.1192087.

[7] I. Szczesniak and J.R. Cary. DXHDF5: A software package for importing HDF5 physics data into OpenDX. *Computer Physics Communications*, 164(1–3):365–369, 2004. doi: 10.1016/j.cpc.2004.06.048.

[8] C.A. Steed, C.F.T. Cheng, and D.V. Harvey. Development of the geophysical data base variable resolution (GDBV) Version 2 using HDF5. In *OCEANS 2009 Marine Technol Soc. and IEEE Ocean Engn. Soc.*, volume 1–3, pages 286–291, Biloxi (MS, USA), 2009. Marine Technol Soc. and IEEE Ocean Engn Soc., IEEE.

[9] M. Jackson, J.P. Simmons, and M. De Graef. MXA: a customizable HDF5–based data format for multi–dimensional data sets. *Modelling and Simulation in Materials Science and Engineering*, 18(6):1–13, 2010. doi: 10.1088/0965-0393/18/6/065008.

[10] K. Bennett and J. Robertson. The impact of the data archiving file format on the sharing of scientific data for use in popular computational environments. In *Conference on Active and Passive Signatures*, volume 7687 of *Proceedings of SPIE-The International Society for Optical Engineering*, Orlando (FL, USA), 2010. doi: 10.1117/12.850609.

[11] J.A. Clarke and R.R. Namburu. A distributed computing environment for interdisciplinary applications. *Concurrency and Computation–Practice & Experience*, 14(13–15):1161–1174, 2002. doi: 10.1002/cpe.685.

[12] W. Kolodenny, M. Prorok, T. Zdanowicz, N. Pearsall, and R. Gottschalg. Applying modern informatics technologies to monitoring photovoltaic (PV) modules and systems. In *33rd IEEE Photovoltaic Specialists Conference*, pages 1–5, San Diego (CA, USA), 2008. doi: 10.1109/PVSC.2008.4922829.

[13] M. Prorok, W. Kolodenny, T. Zdanowicz, R. Gottschalg, and D. Stellbogen. PVML – photovoltaic markup language: Toward universal structure for collection and exchange of data acquired during PV monitoring process. In *23rd European Photovoltaic Solar Energy Conference and Exhibition*, pages 3452–3456, Valencia (Spain), 2008. doi: 10.4229/23rdEUPVSEC2008-5BV.2.30.

[14] Erik T. Ray. *Creating Self–Describing Data. Learning XML*. E.T. Ray, 2001. ISBN 978-0-596-00046-2.

[15] J. Zhanga, A. Webster, M. Lawrence, M. Nepal, R. Pottinger, S. Staub-French, and M. Tory. Improving the usability of standard schemas. *Information Systems*, 36(2):209–221, 2011. doi: 10.1016/j.is.2010.08.005.

[16] IEC 60891. *Procedures for temperature and irradiance corrections to measure I–V characteristics of crystalline silicon photovoltaic devices.*

International Electrotechnical Commission, Geneva (Switzerland), 2nd edition, 2009. ISBN 978-2-88910-316-4.

[17] W. Herrmann, H. Becker, and W. Wiesner. Round robin test on translation procedures for measured PV generator characteristics. In *14th European Photovoltaic Solar Energy Conference*, pages 203–206, Barcelona (Spain), 1997.

[18] IEC 60904–1. *Photovoltaic devices – Part 1: Measurement of photovoltaic current voltage characteristics.* International Electrotechnical Commission, Geneva (Switzerland), 2nd edition, 2006.

[19] ISO–GUM. *Guide 98–3, Evaluation of measurement data – Part 3: Guide to the expression of uncertainty in measurement.* 2008.

Chapter 4

Algorithms for estimating solar parameters

4.1 Introduction

The different proposed methods for estimating several parameters related to the Sun–Earth geometry are analyzed in this chapter. These parameters are necessary for the models proposed in Chapter 5. Some of them have been included as *elements* in the file format proposed in Chapter 3. The algorithms for calculating variables related to the incoming solar radiation have been specifically included here. These include the solar angles (height, azimuth and incidence), the air mass factor and the clearness index. In addition, the procedure in order to determine the average photon energy (APE) from the solar spectrum is described. Some of them are input parameters for the models proposed in Chapter 5. A MATLAB [1] library has been built to implement all these parameters.

The different models proposed to estimate the characteristics of photovoltaic devices under different conditions (specially when using outdoor measurements) take as input two parameters that affect their behaviour: the irradiance and the module temperature. Moreover, some models also use the spectral distribution of the sunlight or the average photon energy.

[1] MATLAB® is a high-level language and interactive environment that enables computationally intensive tasks to be performed.

4.2 Solar position calculations

4.2.1 Introduction

This section sets out some formulas related to the position of the Sun in the celestial sphere. We will then use these calculations in order to determine the angle of incidence and the instantaneous clearness index.

Most of the input parameters used for modelling the photovoltaic modules are based on different formulas that describe the solar position taking into account the Earth–Sun astronomical relationships, given the Sun's coordinates in a specific reference system. Earlier proposed expressions for these parameters have very little computational requirements, but their uncertainties are very high. One of the most common expressions is the one proposed by Spencer [1], which has a maximum uncertainty of 0.25°. Michalsky [2] proposes a method with an uncertainty of 0.011°, but it is only valid for a very restricted period of time, $1950 - 2050$. This is also true for the expression proposed in Blanco–Muriel et al. [3], which is only it is only applicable from 1995 until 2015, and has an uncertainty of 0.008°.

In order to compute the solar coordinates with great accuracy (less than 0.01″), complex astronomical models need to be used, but at greater computational cost. One of them is given by Meeus [4]. Recently, this work has been adapted for solar applications and implemented by Reda and Andreas [5] (a first publication in 2004 and a recent revision in 2008). The latter report is a concise step by step guide to apply the algorithm described by Meeus [4] focusing on the Sun instead of on the planets and adapting the formulas to solar engineering applications. This work includes calculating the angle of incidence for a tilted surface in any orientation using the formulas given by Iqbal [6]. By further simplifying the work of Reda and Andreas [5], in Grena [7] a very acceptable uncertainty is achieved (around 0.003°) with a minimum computational effort, but only valid for the period from 2003 to 2023. We decided to implement the model used by Reda and Andreas [5] in this thesis.

4.2.2 Astronomical time reckoning

The model followed by Reda and Andreas [5] uses a set of astronomical tables and uses as input the date and time given in *Julian Ephemeris Millenniums* `JME`. This is a way of time reckoning used by the astronomers and is based on the *Julian Day* concept. The Julian Day is a linear format (a unique number with fractional part to express part of a day) used to refer to a specific point in time. It represents the number of days since 1 January

-4712 (4713 BC) at 12:00 on the Julian Calendar (this date is 24th November -4713 in the Gregorian Calendar). Hence, prior to using this model, we must calculate the `JME` corresponding to the point in time of each measurement. We will here introduce some concepts to be used to determine this date/time values.

The solar time is defined as the angle (hour angle, measured in hours taking into account that an hour is 15°) between the meridian where the Sun is at noon and the observer meridian. In fact, an offset of 12 hours is added to this value to match the local solar noon with 12:00 hour. A solar day is the time between two successive noons. The flow of the solar time depends on the irregular elliptical motion of the Earth around the Sun (faster when the distance is lower), on the declination (angle between the Earth–Sun vector and the equator plane) and on the rotation of the Earth around its axis. The duration of the solar day therefore changes throughout the year. In order to have a uniform scale of time the mean duration of a solar day is taken into account as if there were a fictitious sun (called mean sun) which crosses the local meridian every day at the same rate. The hour angle (in minutes) that there is every noon between the apparent Sun (the true one) and the mean sun is called equation of time, and its value changes throughout the year between +16 minutes and –14 minutes, and is equal to zero four times a year. The mean solar time measured from the Greenwich meridian (the angle in hours between the fictitious mean sun and the Greenwich meridian) is known as `GMT`.

The sidereal time is another way to reckon time. It is defined as the angle (also measured in hours) between the observer meridian and the *vernal equinox*. The vernal equinox is the point where the ecliptic cuts the celestial equator and where Sun is when spring starts at the northern hemisphere. A sidereal day is the time between two successive crosses of the vernal equinox with the local meridian. After one sidereal day, the celestial sphere with all its stars returns to its original position with respect to the observer. The flow of the sidereal time depends on the rotation of the Earth, which is not as irregular as than the motion around the Sun, but it is slowly decreasing over time. In addition, irregular variations of the order of milliseconds in the rotation motion have been reported. Therefore, the length of the sidereal day is not exactly the same. There are actually two types of sidereal time: the apparent sidereal time and mean sidereal time. On the one hand the vernal equinox is affected by the precession, i.e., it is moving along the ecliptic at about 50" a year (it is a consequence of the very smooth and slow circular motion of the rotation axis with a period of 25800 years). On the other hand, the rotation axis of the Moon is also described as a circular motion, but in this case the period is only 18.6 years. The influence of this motion on the rotation

of the Earth is called nutation, and it affects to the obliquity of the Earth (nutation in obliquity) and to the precession of the vernal equinox (nutation in longitude). The mean equinox is the point where the vernal equinox would be if there was no nutation. The mean sidereal time is the hour angle of this mean equinox and the mean sidereal day is the time between to consecutive upper transit of this mean equinox. The difference between the apparent and the mean sidereal time is called the equation of equinoxes. This difference is at most around one second (very little in comparison with the 16 minutes in the equation of time of the Sun). The mean sideral time measured from the Greenwich meridian is known as `GMST`.

Nowadays, Universal Time (`UT`) has replaced the traditional Greenwich Mean Time (`GMT`). Both of them, `UT` and `GMT`, are defined as the hour angle of the fictitious mean Sun (in hours) with respect to the lower branch of the Greenwich meridian. However, the measurement of the meridian transits of the Sun is not accurate enough, so `UT` is by definition calculated from `GMST`, thanks to the close correlation between `GMST` and mean solar time at Greenwich:

```
24 hours mean sidereal time = 23h 56m 4.090524s mean solar time
```

The time obtained, called `UT0`, is affected by very small error (milliseconds), due to the polar motion (a tiny quasi–circular movement of the Earth's crust with respect to the axis of rotation). After applying a correction for this error `UT1` is achieved, which is commonly called `UT`.

Solar time and sidereal time are based on the rotation of the Earth, which is affected by many irregularities as already mentioned. However a method to measure time with precision and uniformity is necessary. International Atomic Time (`TAI`) is the result of a statistical combination of a great number of atomic clocks all over the world. It is based on the *SI–second* defined according to a property of one isotope of the Caesium element. On the one hand, `UTC` (Universal Coordinated Time), the basis for civilian life, is controlled by `TAI` (`UTC` is incremented following `TAI`). On the other hand, as `UTC` is thought to be used as civil time, it must have a value close to `UT` in order to follow the day/night cycle. However, `UTC` and `UT` are based on different principles, in such a way that the difference between them is continuously increasing. For this reason, when the difference between them is near to 0.9 seconds, a leap second is inserted in order to keep them close one to another. They verify:

$$\mathtt{UT} = \mathtt{UTC} + \Delta\mathtt{UT}$$

where $|\Delta\mathtt{UT}| < 0.9s$. The value of $\Delta\mathtt{UT}$ could be inferred only by observation and it is reported weekly in a bulletin (IERS). Although TAI and UTC are incremented simultaneously, they have different values due to all the accumulated number leap seconds N that have been inserted since the UTC system began.

$$\mathtt{UTC} = \mathtt{TAI} - \mathtt{N}$$

UTC is not a continuous measure of time as a result of the introduction of leap seconds. The Terrestrial Time TT (formerly called Terrestrial Dynamical Time, TDT) is also based on the International Atomic Time. TT and its predecessor ET (ephemeris time) were thought to be a uniform and precise method to describe ephemerides in Astronomy. Whereas ET was based on the movement of the planets and physical laws of motion, TT is based on TAI. However, TT has been conceived as a continuation of ET and at the time when TT started, the difference between TAI and ET was 32.184 s; so by definition we have that:

$$\mathtt{TT} = \mathtt{TAI} + 32.184 \text{ s}$$

.

From the previous definitions, the following relationship also be stated:

$$\Delta T = 32.184 \text{ s} + \mathtt{N} - \Delta\mathtt{UT}$$

Finally, the local civil time is exactly the one given by clocks. It is synchronized with UTC but there is a gap between them known as the time zone. In each country (or each region of a very large country) the official time is exactly the result of adding (or subtracting) to/from the UTC time of an integer number of hours, given by the hour angle between the Greenwich meridian and another meridian with a longitude multiple of 15° (1 hour) near to that country or region. In addition, an extra hour is added in order to save energy in some countries during a period called summer time (actually this period extends beyond the true summer season)

Then, two shifts could have to be removed to change between civil time (zone time) and UTC (universal coordinated time). First the one due to the time zone difference:

$$\mathtt{dateUTC} = \mathtt{dateZone} - (\mathtt{timeZone}/24)$$

And there may be another shift in summer time due to daylight saving time:

$$\texttt{dateZone} = \texttt{dateZoneWithSaving} - (1/24)$$

In both cases the variables are given in days and the shifts must therefore be converted from hours to days.

Given a date and a time in TT, the *Julian Ephemris Millennium* can be computed using the algorithm depicted in the book of Meeus [4]. JME is a linear format (a unique number with fractional part) used to refer a specific point in time. It represents the number of millenniums (based of years of 365.25 days) from 12:00 TT (terrestrial time) on 1 January 2000.

For further information on these time concepts see Karttunen et al. [8].

4.2.3 Solar angles

Several astronomical calculations will be introduced to determine the position of the Sun in the celestial sphere. The final objective is the calculus of the elevation (or its complementary, the zenith angle), the azimuthal angle and finally the angle of incidence.

There are two concepts closely related to the relative Sun–Earth position (see Figure 4.1):

- The ecliptic angle ε is the angle between the normal of the ecliptic plane and the polar axis. It is the same angle as between the equatorial plane and the elliptic plane. Its value is around 23.5° and changes very slowly over thousands of years. In the celestial sphere, it is the angle between the plane containing the celestial equator and the plane containing the apparent path of the Sun.

- The solar declination δ is the angle between the equatorial plane and the line containing the centres of the Sun and the Earth. In the celestial sphere, it is the angle between the line that join the earth centre and the celestial equator (the outward projection of the equator on the celestial sphere). The value of the solar declination is changing continuously during the year between −23.5° (from 21 to 22 December) and +23.5° (from 21 to 22 June), equalling 0.0° twice a year (first between 20 and 21 of March, and also between 22 and 23 of September). The two points of the ellipse in which its minimum and maximum values are reached are called solstices, and other two points in which its value reaches zero are called equinoxes.

The first step consists of calculating the Earth's heliocentric ecliptical coordinates (longitude and latitude of the Earth measured from the centre

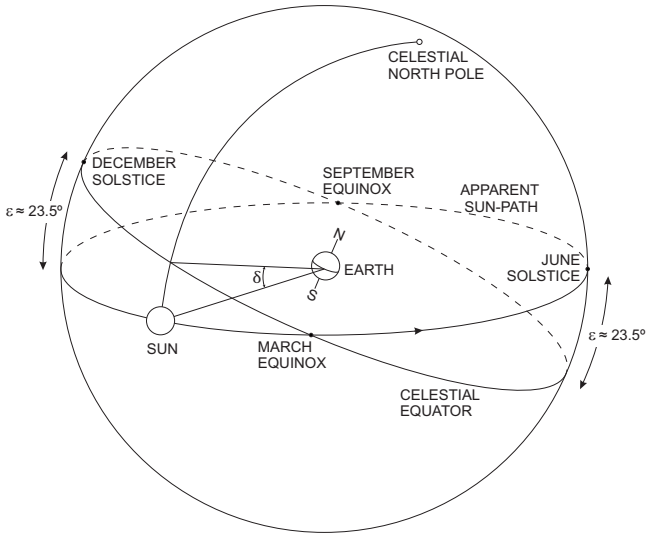

Figure 4.1: Apparent path of the Sun. Declination and ecliptic angles

of the Sun) and the radius vector (distance between the Earth and the Sun). This calculus is performed using several Fourier series whose coefficients are taken from the astronomical tables provided by Reda and Andreas [5] and also the `JME` value associated to the specific point in time. These coordinates must then be converted to a geocentric coordinate system in order to obtain the position of the Sun in the celestial sphere.

The mean value of the obliquity (mean value of the ecliptic angle) is then calculated. The mean value of the obliquity is due to the precession over a period of 25800 years without considering nutation. The ecliptic mean obliquity could be calculated using a tenth order polynomial given also by Reda and Andreas [5]. They also provided several astronomical tables in order to determine the nutation in longitude and nutation in obliquity.

Once all these calculations have been performed the geocentric equatorial coordinates of the Sun can be determined: the right ascension α and the declination δ. However, our objective is to calculate the topocentric equatorial coordinates of the Sun, i.e., the right ascension α' and declination δ' of the Sun measured from the surface of the Earth instead of from the centre of the Earth. Several corrections must be performed in order to determine the topocentric coordinates. Finally, the topocentric hour angle H' is also determined.

We must now calculate the topocentric elevation angle of the Sun (measured from the surface of the Earth) without refraction correction, and the corrected value will then be computed taking into account the air temperature and atmospheric pressure.

The expression for estimating the elevation angle e_0(without correction) is:

$$\sin e_0 = \sin\varphi \sin\delta' + \cos\varphi \cos\delta' \cos H'$$

where φ is the latitude, δ' is the topocentric declination and H' is topocentric local hour angle.

In order to correct this value taking into account different refraction indexes due to variations in air temperature and atmospheric pressure, the following expression can be used:

$$e = 90 - \theta = e_0 + \Delta e = e_0 + \frac{P}{1010} \times \frac{283}{273 + T} \times \frac{1.02}{60 \times \tan(e_0 + \frac{10.3}{e_0 + 5.11})}$$

where θ is the zenith angle, P is the atmospheric pressure and T is the air temperature.

The expression for estimating the azimuth angle Γ is:

$$\tan\Gamma = \frac{\sin H'}{\cos H' \sin\varphi - \tan\delta' \cos\varphi}$$

Angle of incidence: The calculation of the angle of incidence I for a tilted surface in any orientation could be implemented using the formula given by Reda and Andreas [5]:

$$\cos I = \cos\theta \cos\omega + \sin\theta \sin\omega \cos(\Gamma - \gamma)$$

where ω is the slope of the surface (measured from the horizontal) and γ is the rotation (measured from the south) of the oriented surface.

These formulas could be deduced by spherical trigonometry laws [9], but recently Sproul [10] has obtained the same results using vectorial calculus. Figure 4.2 shows the angle of incidence according to the elevation, azimuth, slope and rotation.

4.3 Solar radiation parameters

4.3.1 Extraterrestrial irradiance

This concept is related to the irradiance if there were not atmosphere and the light from the Sun reached the Earth's surface with no obstacle nor deviation. It will be obtained using the solar constant and the exact Earth–Sun distance at a point in time (Earth's radius vector).

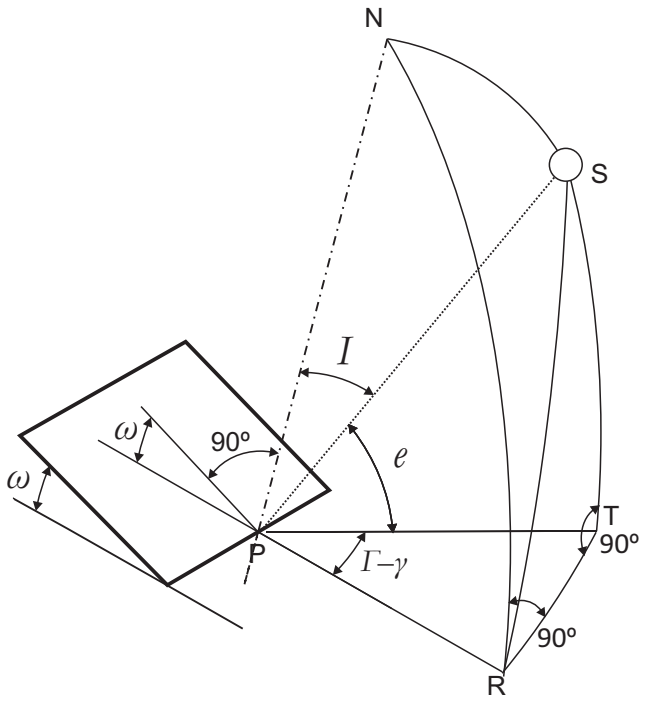

Figure 4.2: Angle of incidence according to the elevation, azimuth, slope and rotation

The *solar constant* is the amount of total solar energy of all wavelengths received by unit time and unit area at the mean Sun–Earth distance in the absence of the Earth's atmosphere. Although it was considered as a constant a few years ago, it is now recognized that this term *solar constant* is misnamed as this value of irradiance is varying continuously. These variations can be observed on all time scales – from minutes to decades, but particularly within the 11–year solar activity cycle. Therefore, this magnitude should be referred to as *total solar irradiance* (TSI), whereas the term *solar constant* should be only used to describe the long-term average of TSI. In this thesis, it is taken as a constant using the value 1366.1 W/m^2 given recently by Gueymard [11] instead of the value 1367 W/m^2, given by Iqbal [6] several years before.

The solar constant, I_0 is calculated for a distance Sun–Earth equal to 1 AU [2]. Taking into account the inverse square law this value is estimated using the expression:

$$I_0 = \frac{P_S}{4\pi r_0^2}$$

[2]The Sun–Earth mean distance r_0 is called 1 astronomical unit (AU), $r_0 = 1$ AU $= 1.496 \times 10^8$ km

where P_S is the solar power (see Iqbal [6]).

This value can be used to estimate the value of the normal or beam extraterrestrial irradiance:

$$I_{0,b} = \frac{P_S}{4\pi r_{0,v}^2} = \frac{I_0(4\pi r_0^2)}{4\pi r_{0,v}^2} = (\frac{r_0}{r_{0,v}})^2 I_0$$

where r_0 is the mean radius vector and $r_{0,v}$ is the radius vector. The term $(r_0/r_{0,v})^2$ is dimensionless and has been called *reciprocal of the square radius vector* by Spencer [1] and *eccentricity correction factor* by Iqbal [6]. Finally, as the value of r_0 is equal to 1 AU, the expression for the normal extraterrestrial irradiance is:

$$I_{0,b} = \frac{I_0}{r_{0,v}^2}$$

This value is the extraterrestrial irradiance with normal incidence, i.e. if the surface is perpendicular to the light of the Sun. If the angle of incidence is other than normal, this value must be reduced by a factor equal to the cosine of the angle of incidence.

4.3.2 Air mass factor

The air mass factor is the optical path length of the light when the Sun is at a given elevation divided by the optical path length when the Sun is at the zenith (theoretically at sea-level). The air mass AM can be approximated using the formula given by Kasten and Young [12] as a function of the elevation, according to the expression:

$$AM = \frac{1}{\sin\alpha + 0.50572(\alpha + 6.07995)^{-1.6364}}$$

The value of air mass can be corrected by pressure as it is proposed in Bird and Riordan [13]. Bird states that a correction by pressure can be performed using the following expression:

$$AM^* = AM\frac{P}{P_0} = AM\frac{P}{1013}$$

where AM^* is the pressure-corrected air mass, P is the pressure and P_0 is 1013 mbar.

4.3.3 Clearness index

Liu and Jordan [14] define the transmission coefficient as the ratio between the global measured irradiance at a horizontal surface and the extraterrestrial irradiance (the theoretical irradiance if there were not absorption or deviation in the atmosphere), according to the expression:

$$\tau = \frac{G}{G_0}$$

where G is the global irradiance (Wm^{-2}) and G_0 is the global extraterrestrial solar irradiance (Wm^{-2}).

Woyte et al. [15] rename the concept of transmission coefficient and term it instantaneous clearness index K_T, extending its definition to whichever angle of incidence over an arbitrarily oriented surface:

$$K_T = \frac{G}{I_0 E \cos I}$$

where I_0 is the solar constant, E is the eccentricity correction factor (due to the elliptical orbit of the Earth) and I is the angle of incidence.

This index K_T is not independent of the zenith angle, for example, a high clearness index values ($K_T \geq 0.8$) does not appear possible for high zenith angles around 80°. An alternative formulation of the clearness index is proposed by Pérez et al. [16] in order to make it independent of zenith angle. This new index is named normalized clearness index $K_T^{'}$ and is defined as:

$$K_T^{'} = \frac{K_T}{1.031 \times \exp(\frac{-1.4}{0.9+\frac{9.4}{AM}} + 0.1)}$$

where AM is the airmass. However, instead of the standard value of AM, we will use the pressure–corrected value AM^*.

4.3.4 Average photon energy

The average photon energy (APE), is an attempt to characterize the spectrum shape using a unique index. The APE is an instantaneous value defined as the ratio of the total irradiance of the spectrum over the photon flux density, i.e., the integrated value of the spectral irradiance divided by the integrated value of the spectral photon flux density, Minemoto et al. [17]:

$$APE = \frac{G}{\Phi} = \frac{\int_0^\infty G_\lambda(\lambda) d\lambda}{\int_0^\infty \Phi_\lambda(\lambda) d\lambda}$$

where G is the total irradiance for the whole spectrum, Φ is the photon flux density of the whole spectrum, $G_\lambda(\lambda)$ is the spectral irradiance and $\Phi_\lambda(\lambda)$ is the spectral photon flux density. The spectral photon flux density at a specific value of wavelength λ can be determined by dividing the spectral irradiance at that λ between the energy of a photon ε_λ with that wavelength (in joules):

$$\Phi_\lambda(\lambda) = \frac{G_\lambda(\lambda)}{\varepsilon_\lambda} = \frac{G_\lambda(\lambda)}{\frac{hc}{\lambda}}$$

where h=6.6260687652$\times 10^{-34}$ Js is the *Planck constant* and c=2.99792458$\times$ 10^8 m/s is the velocity of the light at the vacuum. Using these values the final result of APE will be expressed in J, but it is usual to express it in eV, taking into account that:

$$1 \text{ eV} = 1.60217646263 \times 10^{-19}\text{J}$$

However, spectroradiometers do not have sufficient spectral range to cover the whole solar spectrum. Therefore, the definition of APE can be extended in order to take into account a finite integration interval:

$$APE_{\lambda_a}^{\lambda_b} = \frac{\int_{\lambda_a}^{\lambda_b} G_\lambda(\lambda)d\lambda}{\int_{\lambda_a}^{\lambda_b} \Phi_\lambda(\lambda)d\lambda}$$

where λ_a and λ_b are the integration limits.

A numerical integration method can be used in order to implement a routine to compute this APE value; we propose to use a trapezoidal integration:

$$APE_{\lambda_a}^{\lambda_b} \approx \frac{\sum_{i=1}^{n} \frac{G_\lambda(\lambda[i])+G_\lambda(\lambda[i-1])}{2}(\lambda[i]-\lambda[i-1])}{\sum_{i=1}^{n} \frac{\Phi_\lambda(\lambda[i])+\Phi_\lambda(\lambda[i-1])}{2}(\lambda[i]-\lambda[i-1])}$$

in eV, where $i = 0..n$, $\lambda[0] = \lambda_a$ and $\lambda[n] = \lambda_b$.

It is remarkable that the estimation of each value of $\Phi\lambda(\lambda[i])$ requires the previous calculus of ε_λ as hc/λ. A conversion factor equal to 10^{-6} or 10^{-9} needs to be applied to λ to get ε_λ in joules as it is usual to have λ in μm or nm respectively.

We propose the evaluation of this index along several contiguous integration ranges instead of evaluating the APE value along a unique range. In this way more information from the original spectral measured is taken into account, and what is more important, the spectral range has been split into intervals that depending on the spectral response of each photovoltaic technology would have more or less influence in the power output of the cell or module.

4.4 Conclusions

The different expressions for estimating the parameters related with the Sun–Earth geometry have been presented in this chapter. As an important contribution to the previous related works, it is proposed to estimate the average energy photon by using different intervals of integration rather than using several values. Some of these parameters will be used as inputs to the models developed in Chapter 5.

Bibliography

[1] J.W. Spencer. Fourier series representation of the position of the sun. *Search*, 2(5):172–177, 1971.

[2] J. Michalsky. The astronomical Almanac's algorithm for approximate solar position (1950–2050). *Solar Energy*, 40(3):227–235, 1988. doi: 10.1016/0038-092X(88)90045-X.

[3] M. Blanco–Muriel, D.C. Alarcón–Padilla, T. López–Moratalla, and M. Lara–Coira. Computing the solar vector. *Solar Energy*, 70(5):431–441, 2001. doi: 10.1016/S0038-092X(00)00156-0.

[4] J. Meeus. *Astronomical Algorithms*. Willmann–Bell Inc., 1991. ISBN 978-0-943396-35-4.

[5] I. Reda and A. Andreas. Solar position algorithm for solar radiation applications. Technical Report NREL/TP–560–34302, National Renewable Energy Laboratory (NREL), Golden (CO, USA), 2008.

[6] M. Iqbal. *An Introduction to Solar Radiation*. Academic Press, New York (NY, USA), 1983. ISBN 978-0-12-373752-6.

[7] R. Grena. An algorithm for the computation of the solar position. *Solar Energy*, 82(5):462–470, 2008. doi: 10.1016/j.solener.2007.10.001.

[8] H. Karttunen, P. Kroger, H. Oja, M. Poutanen, and K.J. Donner. *Fundamental Astronomy*. Springer, 5th edition, 2007. ISBN 978-3-540-34143-7.

[9] S.V. Szokolay. *Solar Geometry*. Passive and Low Energy Architecture International and University of Queensland, Brisbane, Australia, 2007. ISBN 0-86766-634-4.

[10] A.B. Sproul. Derivation of the solar geometric relationships using vector analysis. *Renewable Energy*, 32(7):1187–1205, 2007. doi: 10.1016/j.renene.2006.05.001.

[11] C.A. Gueymard. The Sun's total and spectral irradiance for solar energy applications and solar radiation models. *Solar Energy*, 76(4):423–453, 2004. doi: 10.1016/j.solener.2003.08.039.

[12] F. Kasten and A. Young. Revised optical air mass tables and approximation formula. *Applied Optics*, 28(22):4735–4738, 1989. doi: 10.1364/AO.28.004735.

[13] R.E. Bird and C. Riordan. Simple solar spectral model for direct and diffuse irradiance on horizontal and tilted planes at the earth's surface for cloudless atmospheres. *Journal of Climate and Applied Meteorology*, 25(1):87–97, 1986. doi: 10.1175/1520-0450(1986)025<0087:SSSMFD>2.0.CO;2.

[14] B.Y.H. Liu and R.C. Jordan. The interrelationship and characteristic distribution of direct, diffuse and total solar radiation. *Solar Energy*, 4 (3):1–19, 1960. doi: 10.1016/0038-092X(60)90062-1.

[15] A. Woyte, R. Belmans, and J. Nijs. Fluctuations in instantaneous clearness index: Analysis and statistics. *Solar Energy*, 81(2):195–206, 2007. doi: 10.1016/j.solener.2006.03.001.

[16] R. Pérez, P. Ineichen, R. Seals, and A. Zelenka. Making full use of the clearness index for parameterizing hourly insolation conditions. *Solar Energy*, 45(2):111–114, 1990. doi: 10.1016/0038-092X(90)90036-C.

[17] T. Minemoto, S. Nagae, and H. Takakura. Impact of spectral irradiance distribution and temperature on the outdoor performance of amorphous Si photovoltaic modules. *Solar Energy Materials & Solar Cells*, 91(10): 919–923, 2007. doi: 10.1016/j.solmat.2007.02.012.

Chapter 5

Artificial neural networks for simulating photovoltaic modules

5.1 Introduction

A novel methodology based on artificial neural networks is proposed as an alternative to algebraic and numerical procedures to determine the I–V curve of a module under different conditions. Although there are methods that use neural networks for approximating the I–V curve, this is the first time that the measurement of the spectrum is incorporated as an input. In addition, a suitable selection of the training samples used to build the model is fundamental in order to get an accurate approximation. This is why a training sample selection based on a Kohonen self–organizing map is performed instead of a random selection. Using this preliminary step, the performance of the network trained with spectral information improves over the one without spectral information.

Photovoltaic engineering requires tools in order to forecast the behaviour of photovoltaic modules under different measurement conditions. Basically, the most relevant of these conditions are the irradiance and the module temperature, but also the spectral distribution of the sunlight. Manufacturers must report the electrical parameters under specific conditions referred as *standard test conditions* STC: global irradiance equal to 1000 W/m^2, cell temperature equal to 25 °C and spectral distribution AM1.5, defined by the standard IEC 60904–3 [1]. However, it is necessary to have models to get I–V curves of a photovoltaic module with flexibility under different conditions of irradiance, temperature and spectral distribution.

Mathematical procedures which can be applied to determine the *I–V* curve of a PV module under different conditions of irradiance and module temperature can be found in the literature. Herrmann et al. [2] classify them into algebraic and numerical. Algebraic methods consist of a point–by–point extrapolation in order to translate both coordinates of each individual current–voltage pair of the curve from the measured conditions to the new conditions. As a result, we obtain an approximation to the *I–V* curve that we would measure if the module was under the new conditions of irradiance and cell temperature. One of these algebraic methods was published by Sandstrom [3]. It has been widely used for decades and has become known as the standard *procedure 1* by IEC 60891 [4]. However, several alternatives improving this method include works published by Blaesser and Rossi [5], Anderson [6] and Marion [7]. In 2004, Marion et al. [8] published the bilinear interpolation method. As well as being applicable to a wide range of conditions, this method has proved suitable for different PV technologies. However, these algebraic methods do not deal with the possible difference between the spectral distribution at the time of measurement and the spectral distribution under other conditions. Depending on the spectral response of each PV module, its *I–V* curve could be significantly affected by the sunlight spectrum, which varies with atmospheric conditions, time of the day, season and location, among others. If the spectral irradiance distribution of the incoming light and the spectral response of the PV module are known, a correction could be made in order to obtain the performance under the AM1.5 spectrum (or any other desired spectrum) by means of the standard IEC 60904–7 [9]. This standard describes a mathematical procedure which could be used to correct the measurement taking into account the spectral mismatch between the measured spectrum and the spectrum under other conditions.

In addition to algebraic translation equations, there are more complex methods based on semiconductor physics, where photovoltaic devices are modelled using different equivalent circuits composed by a few discrete components. They are usually based on the one–diode solar cell model [10] but some are also based on the two–diode model [11]. In these methods, the relationship between current and voltage is given by a mathematical expression containing several parameters, in such a way that some of these parameters could be expressed as a function of the irradiance and the cell temperature. Intrinsic parameters of the module could be determined by means of a numerical procedure in order to fit the model to experimental measurements. A recent work published by Domínguez et al. [12] describes a model for multi–junction solar cells based on the one–diode equivalent circuit, where irradiance, cell temperature and spectral distribution are taken into account.

An alternative approach is the use of an artificial neural network (ANN) to create a model of the photovoltaic module. Several examples can be found in the literature where ANNs are used to generate I–V curves of photovoltaic modules, Patra [13], Karatepe et al. [14], Di Piazza et al. [15], Hontoria et al. [16], Almonacid et al. [17], Almonacid et al. [18], Almonacid et al. [19] and Zárate et al. [20]. In these works, ANNs are used in order to reconstruct the I–V curve of a module under given values of irradiance and module temperature. However, these authors do not take the spectral distribution of the incident light into account.

Different input parameters have been analyzed to model the I–V of photovoltaic modules. Specifically, the angle of incidence, the clearness index and the spectrum values has been checked. The main contribution of our work is the incorporation of the measured spectrum to develop a method based on the multilayer perceptron which allows us to determine the I–V curve at every condition of irradiance, temperature and spectral distribution. Knowing the spectral response of the PV module is not necessary with this method as the neural network is able to learn it from the set of measurements. However, the incorporation of the spectrum as an input of the ANN has a computational cost. Whereas the input parameters of the networks in previous papers are scalar values, the solar spectrum has a more complicated structure given by a sequence of wavelength–irradiance pairs (a table of points). Dealing with so much information without care being taken would lead to unworthy results. A spectral format based on the concept of average photon energy is proposed in this thesis to overcome this problem.

In addition, a suitable selection of the training set (among all acquired measurements) could enhance the output of the neural network. In this thesis a pattern selection based on the spectral distribution has been performed using a Kohonen self–organizing map.

5.2 Neural networks applied to PV simulation

ANNs have been successfully applied to solve many real life applications, including solar radiation and photovoltaic systems modelling. Neural networks have been used to estimate and forecast the global solar radiation or the clearness index such as the works of Elizondo et al. [21], Yona et al. [22] and Mora–López et al. [23]. In addition, there are also many examples where this approach has been used as a tool to track the maximum power point of a PV generator, see for instance Zhang and Bai [24] and Chao et al. [25].

Among all the existing neural networks, we propose to use the multilayer perceptron (MLP) trained with a variation of the conventional backpropagation rule based on the Levenberg–Marquardt algorithm. Principe et al. [26] describe in detail the topology of the MLP and the different training algorithms for this type of neural network. Using a neural network as a model of a specific photovoltaic module, we are able to reproduce the characteristic curve of that module at given value of irradiance and cell temperature. In order to have a tool to simulate the behaviour of the module, we should use a training set of I–V curves measured at a wide range of different conditions. Once the network has been trained, the I–V curve under the new conditions can be calculated by providing the corresponding values of both irradiance and cell temperature.

A simple example of I–V curve modelling using neural networks can be found in Patra [13]. Two different multilayer perceptrons are used to determine the I–V curve of a dual–junction solar cell in only two special cases: under darkness and under one sun irradiance (1000 W/m^2). In both cases, each neural network takes at its input a voltage value and it returns the associated current value.

Karatepe et al. [14] propose a hybrid approach consisting of the use of a multilayer perceptron which takes the values of irradiance and cell temperature as its input and returns as output the parameters required by the one–diode equivalent circuit. In a second stage, these estimations are assigned to the parameters of the electrical model in order to determine the complete set of points of the I–V curve.

In the paper by Di Piazza et al. [15] a growing neural gas (GNG) network is used in a similar way. In this case, the GNG network is used to determine a reduced number of points of the I–V curve: the short circuit current, the open circuit voltage and the maximum power point. A set of analytical expressions can be used to determine the free parameters of the two–diode model. Finally, with the help of this model, the complete set of points of the I–V curve can be generated. The main advantage of the GNG network is that, during the training phase, the number of neurons grows until the model can fit the input data.

Hontoria et al. [16] present a method to obtain the characteristic curve of a module at any given condition using a MLP. In this paper, the hypothesis that the voltage could be given as a function of the current, the irradiance and the air temperature is assumed. In the same way, Almonacid et al. [17] carried out a study for electrical characterisation of mono–crystalline and poly–crystalline silicon modules. The conditions of measurement considered here have been the irradiance and the module temperature. In a more recent article [19], the same method was applied to the electrical characterisation

of CIS modules. Finally, this technique has been also extended in order to forecast the evolution of the power produced by a complete photovoltaic plant throughout a day [18].

In the paper by Zárate et al. [20], a similar approach has been proposed. The current of the photovoltaic module is calculated based on the values of voltage, irradiance and module temperature. Then, in addition to the inputs used for irradiance and module temperature, there is an additional fictitious input which represents the voltage coordinate for each point of the I–V curve. The output layer of the network has only one neuron which represents the current coordinate of each point of the curve.

The main advantage of neural network approaches is their capacity for generalization, as they are able to reconstruct the I–V curve of a module with high fidelity, even for irradiance and temperature conditions not considered during the training of the network. However, there is another additional advantage: although it is usual to simulate ANNs by software, it is also possible to implement them on a specific electronic hardware, allowing for their integration inside other electronic systems. An example can be found in the paper of Mekki et al. [27], where a hardware implementation of a MLP is used to estimate the output of PV modules using radiation and air temperature.

5.3 Measurement system and facilities

Measurements have been carried out on the roof of the Photovoltaic Laboratory of the University of Malaga in the south of Spain, very close to the Mediterranean Sea. The typical meteorological conditions at the site of the installation are: 1890 kWh/m^2 of annual global irradiation, average daytime ambient temperature of 18 °C, relative humidity 63 % and wind speed of 1 m/s. Data used in this work was recorded from the 1 February, 2011 to the 22 May, 2011 with measurements taken at 5–minute intervals. There are several missing samples due to maintenance tasks.

A complete description of the measurement system and the estimation of the uncertainties is described in Chapter 2. The duration of the voltage sweep between I_{SC} and V_{OC} has been set to 1 second. Module temperature is measured through a RTD Pt100 sensor coupled to its backside. Irradiance incident on the module surface is measured using a pyranometer (Kipp & Zonen CMP21). These signals are recorded at the beginning and at the end of each measurement by an acquisition data system. Finally, a spectroradiometer EKO MS–710 (spectral range from 350 nm to 1050 nm) installed at the same plane as the modules and the pyranometer is connected to the control

computer through a RS–485 serial interface. The nominal specifications of the specimen used in the experiments are summarized in Table 5.1.

General features	
Manufacturer	Isofoton S.A.
Model	I-94 / 12
Serial No.	0306016407733
Dimensions	1208 × 654 × 39.5 (mm × mm × mm)
Weight	11 kg
Number of cells	66
Cells in series	33
Cells in parallel	2
NOCT	47 °C
Type of cell	m–Si
Cell dimensions	103 × 103 (mm × mm)
Cell area	104.4 cm^2
Electrical parameters at STC	
Short circuit current I_{SC}	6.54 A
Open circuit voltage V_{OC}	19.8 V
Maximum power P_M	94 W
Maximum power current I_M	5.88 A
Maximum power voltage V_M	16 V

Table 5.1: Main features of the m–Si photovoltaic module used as specimen in the experiments

5.4 Representation of current–voltage curves

To determine the evolution of the electrical parameters of the module, the best option consists of calculating these electrical parameters for each I–V curve before the network is trained. The network can then be trained to compute only the values of I_{SC}, V_{OC} or P_M. In this case we only need a network which takes the irradiance and module temperature as input and returns as its output the value of each of electrical parameter. Whereas learning a scalar parameter as I_{SC} or V_{OC} is straightforward, learning a set of points would be more complicated as it is necessary to find a format to represent I–V curves to be used in a neural network. We have I–V curve measurements with their respective irradiance and temperature values at different points in time. Our initial set of inputs consists of a list of records; one record for each point in

Date	Time	G (W/m^2)	T_m (°C)	I–V curve (V,A)				
				V_1	I_1	...	V_p	I_p
19/03/11	13:01	1034	53.7	0.015	6.390	...	17.277	0.170
19/03/11	13:11	1038	55.5	0.353	6.411		17.175	0.022
19/03/11	13:21	1042	53.9	0.407	6.419		17.378	0.186

Table 5.2: Examples of original records in the database

time. Each record comprises several measurements used as inputs for our model and an I–V curve used as the output of our model. This I–V curve is provided in terms of a table of current–voltage pairs. The problem of this representation is how to express it using the output layer of the multilayer perceptron.

In this thesis, we have solved this problem in the same way as Zárate et al. [20]. A fictitious neuron is added to the input layer in order to represent the voltage coordinate of each point of the curve. In the output layer a single neuron represents the current associated to each value of voltage. Therefore, this network has `m+1` inputs (where `m` represents the number of parameters) and a single output representing the current value of that point. So, in order to obtain an I–V curve from the network, first the `m` values of the parameters for a specific point in time must be fixed at the input layer. Furthermore, by varying the value of the fictitious input neuron, we could retrieve the current values of each point from the output neuron. For each original record `p` stored at a point in time, we must generate P patterns (as many as points belonging to the I–V curve). In mathematical terms, we are mapping the initial function Ψ into another function Γ easier to represent:

$$\Psi : \mathcal{R}^m \rightarrow \mathcal{R}^{Px2} \qquad \Psi(G, T, \dots) = \{(V_i, I_i)\}_{i=1}^{P}$$

$$\Gamma : \mathcal{R}^{m+1} \rightarrow \mathcal{R} \qquad \Gamma(G, T, \dots, V) = I$$

Table 5.2 illustrates some examples of records as they have been stored in the built database. The training set for the MLP can be generated from these original records by splitting each record into as many patterns as points of each I–V curve. The results of this process applied to this example are shown in Table 5.3.

Input			Target
$G(\mathrm{W/m^2})$	$T_m(^\circ\mathrm{C})$	$V(\mathrm{V})$	$I(\mathrm{A})$
1034	53.7	0.015	6.390
	...		
1034	53.7	17.227	0.170
1038	55.5	0.353	6.411
	...		
1038	55.5	17.175	0.022
1042	53.9	0.407	6.419
	...		
1042	53.9	17.378	0.186

Table 5.3: Patterns resulting of the application of the described process

5.5 Angle of incidence and clearness index

The MLP training process to achieve a model for a specific module of mono–crystalline (m–Si) silicon cells has been performed using different input parameters. This section describes the process and results when the angle of incidence and the clearness index are used as input parameters to train the MLP.

Table 5.4 shows the geographical coordinates required as inputs in the algorithm of Reda and Andreas [28] to estimate the solar angles (latitude, longitude and elevation with respect to the sea level) and the slope and rotation of the PV module.

Longitude	-4.478133°
Latitude	36.715174°
Elevation	50 m
PV module slope (from horizontal)	21° ($\pm 1^\circ$)
PV module rotation (from South)	4° W ($\pm 2^\circ$)

Table 5.4: Parameter values used for solar position calculations

5.5.1 Training of the multilayer perceptron

Two different sets of samples have been used as the objective is to measure the increase of performance due to the incorporation of the angle of incidence and the normalized clearness index:

- A: 5822 samples with an I–V curve with only irradiance and module temperature
- B: 5822 samples with an I–V curve, irradiance, module temperature, angle of incidence and clearness index

First, 100 samples were randomly selected from among all the measurements. These samples have been used for training the network. The remaining 5722 samples have been used for testing the network.

The next step has been the splitting of each record into 100 training patterns, one for each I–V point of the curve as it has been previously described: for each curve from the training set, we will get as many patterns as points belong to that curve. Therefore, each input pattern of the MLP contains the measure of irradiance, module temperature, angle of incidence, clearness index and each voltage component for each I–V pair. In contrast, the new output for such pattern consists of the current component of each I–V pair only. This process has been performed for the sets A and B. In summary, there are 2 training and 2 testing sets of patterns. Table 5.5 shows these datasets.

A	5822 records with only G and T_m
A_1	100 I–V curves with irradiance and temperature selected randomly for training
A_2	5722 I–V remaining curves with irradiance and temperature for testing
B	5822 records with G, T_m, AOI and $K_T^{'}$
B_1	I–V 100 curves with G, T_m, AOI and $K_T^{'}$ selected randomly for training
B_2	5722 I–V remaining curves with G, T_m, AOI and $K_T^{'}$ for testing

Table 5.5: Description of the training and testing sets used when the clearness index and the angle of incidence are used as input parameters

There are several stop criteria in order to finish the training phase. One of them is called validation check and it seeks to avoid over–fitting. Over–fitting occurs when the network learns the training set but presents difficulties generalizing with unseen patterns (testing set). Each time training takes place, the training routine automatically divides the set of patterns into two groups. Most of the patterns, known as the training set, are used in order to adjust the weights depending on the error between the output of the network and the desired target.

A small percentage of those patterns, known as the validation set, are not used to update the weights and only its error is monitored. The training and validation errors usually decrease at the beginning of the training process. When the MLP begins to over–fit data, the validation error starts to rise. The training process is stopped when this error has been increased a number of times consecutively. We have set this parameter to 10 times and configured the network in order to use only a 10 % of patterns for validation.

The number of neurons in the input and output layers have been determined from the set of patterns and its representation. There is no rule to determine the number of hidden units in a MLP beforehand. We must experiment with different number of neurons performing multiple trainings and studying how it affects the output and mean error of the network. For each combination, we obtained a different trained MLP and the performance of each one must be evaluated.

The generalization error of each MLP can be computed using all the curves of the dataset not used during the training phase, i.e. the sets in Table 5.5 referred as A_2 and B_2, each one with the 5722 I–V curves which are independent from the training set of records. Given a trained network *mlp* and a target record $\boldsymbol{R}_j = \{< \boldsymbol{V}_j, \boldsymbol{I}_j > \| G_j, T_j, \dots\}$ from the testing set (where $< \boldsymbol{V}_j, \boldsymbol{I}_j >$ is an I–V curve measured under specific conditions), its associated approximation by the network (output curve) must be computed as it is shown in Figure 5.1.

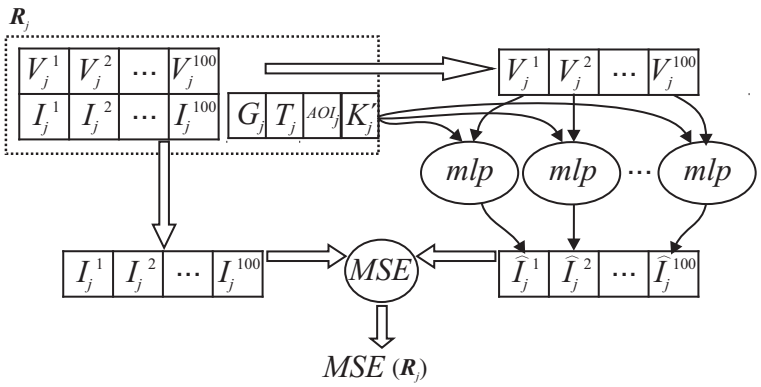

Figure 5.1: Scheme of the calculus of MSE of a trained network over a record of the testing set.

Fixing the conditions of the measurement $(G_j, T_j, \dots, V_j^p)$, at the network input and varying the fictitious voltage input V_j^p (using the voltage component of each I–V point p of the target curve), the network will return a sequence of current values $\hat{I}_j^p$ defined as:

$$\hat{I}_j^p = mlp(G_j, T_j, \ldots, V_j^p) \qquad p = 1, \ldots, 100$$

The output curve $< \boldsymbol{V}_j, \hat{\boldsymbol{I}}_j >$ will be the list of points composed by the voltage components of the target curve and the current values returned by the network. Hence, the measured target curve and the approximate output curve share the voltage components, differing only in the current component. The mean squared error of the differences between the current components $MSE(\boldsymbol{I}_j, \hat{\boldsymbol{I}}_j)$ will be the error of the trained network $mlp(\boldsymbol{R}_j)$ for the record $\boldsymbol{R}_j$ of the testing set:

$$MSE(\boldsymbol{R}_j) = MSE(\boldsymbol{I}_j, \hat{\boldsymbol{I}}_j)$$

Finally, the generalization error of the trained network will be the mean value of MSEs values for all the curves in the testing set (where N is the number of records stored in the testing set):

$$MSE_{mlp} = \frac{1}{N}\sum_{j=1}^{N} MSE(\boldsymbol{R}_j) = \frac{1}{N}\sum_{j=1}^{N} MSE(\boldsymbol{I}_j, \hat{\boldsymbol{I}}_j)$$

5.5.2 Results and discussion

For the discussion, the trained network with the smallest MSE value when using as input parameters G and T_m will be denoted as $\mathrm{MLP_{GT}}$. Similarly, the trained network with the smallest MSE when using as input parameters G, T_m, AOI and K_T' will be denoted as $\mathrm{MLP_{ALL}}$. The individual curve results of both networks over the testing set of samples have been compared.

Taken into account the complete testing set (5722 samples not selected for training), the $\mathrm{MLP_{ALL}}$ returns a better approximation (closer to the measured curve) than the $\mathrm{MLP_{GT}}$ in a total of 2889 examples (50.5 %), whereas in the 2833 remaining examples (49.5 %) $\mathrm{MLP_{GT}}$ is better. Although the global mean MSE is smaller than the MSE of the MLP trained with AOI and K_T', if we study the number of I–V curves in which the introduction of these parameters into the network has implied an improvement, the results are not so good. However, if only the I–V curves measured at irradiance lower than 400 W/m^2 are taken into account (there are 1408 samples that satisfy this condition), then the approximation given by the $\mathrm{MLP_{ALL}}$ model has a mean squared error lower than the approximation given by the $\mathrm{MLP_{GT}}$ one in a total of 934 cases. Consequently, at low irradiance values ($<$ 400 W/m^2), in 66.3 % of the cases, the introduction of AOI and K_T' in the network implies

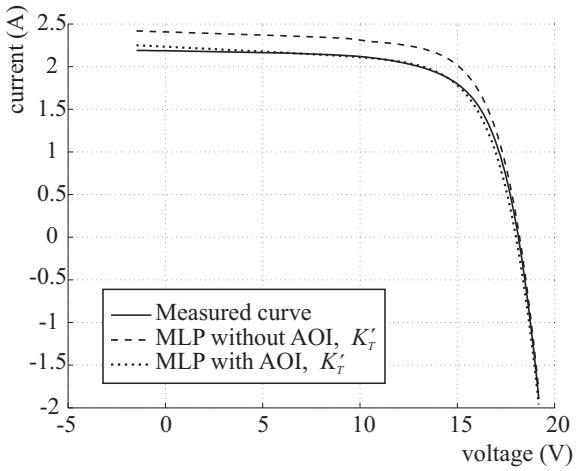

Figure 5.2: Results obtained by the MLP_{ALL} and MLP_{GT} models with low irradiance (11 February).

an improvement of the results. This means that the proposed model MLP_{ALL} is only better than the MLP_{GT} model at low irradiance.

A more detailed study curve by curve is now performed. In order to illustrate the behaviour of both models, only a few examples (4 selected I–V curves) among the 5722 records of the testing set will be analyzed. Figure 5.2 is a typical example of an I–V curve acquired at a low irradiance value. It was taken at 17:06 on the 11 February, 2011 at with a global irradiance of 383 W/m^2 and a module temperature of 26.7 °C. As can be seen, in this example the approximation given by the MLP model trained with AOI and K_T' is significantly better than the approximation given by the one with only G and T_m.

The previous situation is often found in most of the I–V curves with low irradiance. For instance, the I–V curve corresponding to the 21 March, 2011 at 8:41, with $G = 287$ W/m^2 and $T_m = 15.6$ °C (Figure 5.3) is another example that confirms that the behaviour of the MLP_{ALL} model is better than the behaviour of the MLP_{GT} one in cases with low irradiance.

However, there are examples where neither model gives a satisfactory approximation. For example, in Figure 5.4 an I–V curve is shown. It was measured at 17:41 on 28 February 2011, with $G = 349$ W/m^2 and $T_m = 22.4$ °C. Both approximations are far from the measured curve (although MLP_{ALL} has a slightly small error).

Finally, there are a few exceptions, even at a low value of irradiance, where the behaviour of network with AOI and K_T' is worse than the approximation given by the one with only G and T_m. Figure 5.5 shows an I–V curve

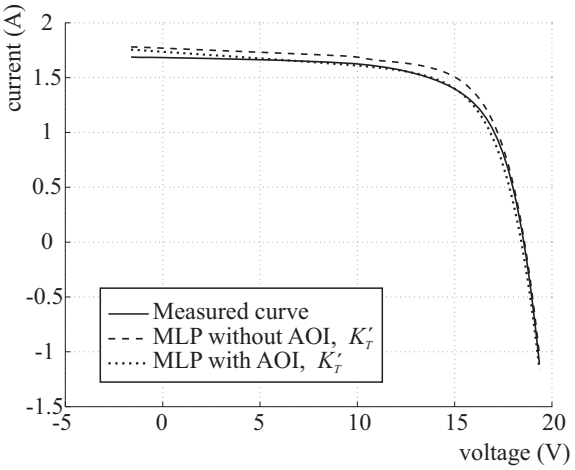

Figure 5.3: Result obtained by the $\mathrm{MLP_{ALL}}$ and $\mathrm{MLP_{GT}}$ models with low irradiance (21 March).

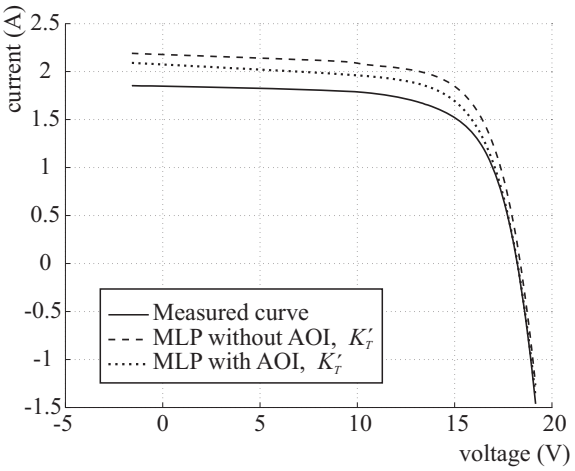

Figure 5.4: I–V curves for the measurement acquired on 28 February.

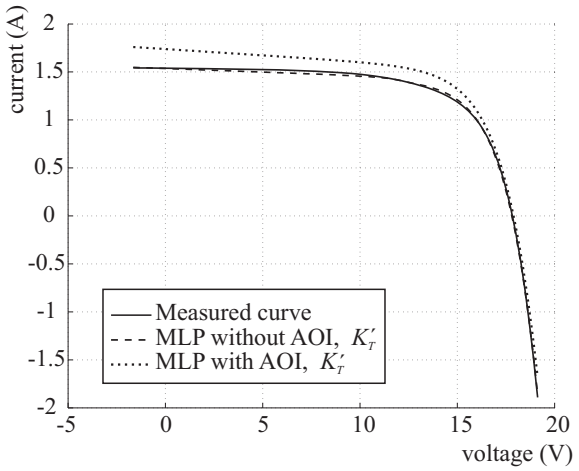

Figure 5.5: I–V curves for the measurement acquired on 13 March.

measured at 15:21 on 13 March 2011, with $G = 236$ W/m^2 and $T_m = 25.3$ °C. Whereas the MLP_{GT} model has obtained a good result, the MLP_{ALL} model gives an approximation quite far from the measured I–V curve.

5.5.3 Results for clear–sky days

The AOI is very important when most of the incoming radiation is direct radiation, but it is not so important in the presence of clouds. Therefore, it is possible to perform a new selection among all the measurements stored in the initial dataset. The idea is to select only those measurements taken on perfectly clear–sky days, and then repeat the training process.

These days have been selected from the measuring period: 18, 23, 24, 25, and 28 February; 1, 2, 17, 18, 19, 24, 27, 30 and 31 March; 1, 7, 8, 9, 10, 12, 13, 14, 16, 26, 27 and 28 April; 5, 8, 9, 14, 21 and 22 May. The number of samples was then reduced to 3156. The initial datasets will now be: A$'$ (3156 samples with an I–V curve with only irradiance and module temperature) and B$'$ (3156 samples with an I–V curve, irradiance, module temperature, angle of incidence and clearness index). Table 5.6 shows these data sets.

One hundred samples have been selected randomly from among all the measurements to train the network and the remaining 3056 samples have been used to test the network. Finally, each record is split into 100 training patterns, one for each I–V point of the curve. Both networks (with and without AOI and K_T') have been trained in accordance the aforementioned procedure.

The trained network with the smallest MSE value when using as input

A	3156 records with only G and T_m
$A_1^{'}$	100 I–V curves with irradiance and temperature selected randomly for training
$A_2^{'}$	3056 I–V remaining curves with irradiance and temperature for testing
$B^{'}$	3156 records with G, T_m, AOI and $K_T^{'}$
$B_1^{'}$	I–V 100 curves with G, T_m, AOI and $K_T^{'}$ selected randomly for training
$B_2^{'}$	3056 I–V remaining curves with G, T_m, AOI and $K_T^{'}$ for testing

Table 5.6: Description of the training and testing sets used when the clearness index and the angle of incidence are used as inputs over clear–sky days

parameters G and T_m will be denoted by $\text{MLP}_{\text{GT}}^{'}$. The trained network with the smallest MSE when using as input parameters G, T_m, AOI and $K_T^{'}$ will be denoted as $\text{MLP}_{\text{ALL}}^{'}$. The individual curve results of both networks over the testing set of samples have been also compared.

Given the complete testing set the $\text{MLP}_{\text{ALL}}^{'}$ returns a better approximation (closer to the measured curve) than the $\text{MLP}_{\text{GT}}^{'}$ in a total of 1972 examples (64.5 %), whereas in the 1084 remaining examples (35.5 %) the $\text{MLP}_{\text{GT}}^{'}$ gives better results. The mean squared error of the $\text{MLP}_{\text{ALL}}^{'}$ is lower than the mean square error of the $\text{MLP}_{\text{GT}}^{'}$ in a total of 529 cases for irradiance lower than 500 W/m^2 (there are 694 samples that satisfy this condition). Consequently, at low irradiance values (< 500 W/m^2), in 76.2 % of the cases, the introduction of AOI and $K_T^{'}$ in the network implies a significant improvement of the results.

5.6 Spectral measurements

This section describes the process and results when the spectral measurements are used as input parameters to train the MLP.

5.6.1 Representation of spectral measurements

The network inputs were simple scalar values in previous methods that use ANNs to learn the behaviour PV modules. Using an input neuron for each different input parameter is enough in these cases. However, the incorporation of the solar spectral distribution cannot be addressed in this

way and therefore a more complex structure is needed to represent this information. Theoretically, a spectrum is a function that returns the spectral irradiance (Wm^{-2}/nm) associated to each possible value of wavelength (nm). When a spectroradiometer measures a spectrum, it acquires values of spectral irradiance at specific points of a grid of wavelengths, returning a table with wavelength–irradiance values. Different spectroradiometers take measures following different grids of wavelengths. Therefore, each model returns a table with a specific number of points at different wavelength intervals . Even the AM1.5 specification, given by IEC 60904–3 [1], is expressed as a table of measurements with its own grid of wavelength values.

The management and representation of spectral distribution brings several problems. First, the same solar spectral distribution will have different representations depending on the equipment used to measure it. Second, the amount of data given by each table is very large. Thus, the dimensionality of this data will affect the accuracy and training time of the neural network negatively. Finally, if a neural network was trained using raw data measured by a specific spectroradiometer, the network will always expect a list of values with the spectrum in the same format (the same number of points at the same wavelength intervals). This neural network could not be used with an input spectrum measured with another spectroradiometer. Neither could it be used with the AM1.5 spectrum given by the standard. Consequently, the information captured in each spectrum needs to be expressed using another format independent from the wavelength grid used. This means that before training the network, all measured spectra will be converted to this format and, once the network has been trained, the input spectra will need to be expressed in this format in order to use the network.

A possible solution is to use the average photon energy (APE) index in an attempt to characterize the spectrum shape using a unique value. The APE is an instantaneous value defined as the ratio of the total irradiance of the spectrum over the photon flux density. However, spectroradiometers do not have enough spectral range to cover the entire solar spectrum. Consequently, the definition of APE is usually referred to as a finite integration interval [29]. There are statistical studies [30] that support the idea that the APE value uniquely characterises the shape of a solar spectrum. However, thinking that all the information of the whole spectrum can be summarized in a unique value is not useful for our purposes. This is because we are ignoring a great amount of information that the neural network could take into account. Instead of evaluating the APE value along a unique range of wavelength, we propose the evaluation of this index along several contiguous integration ranges. In this thesis 7 intervals of 100 nm between 350 nm and 1050 nm have been used:

$$APE_{350nm}^{450nm},\ APE_{450nm}^{550nm}, , \ldots, APE_{950nm}^{1050nm}$$

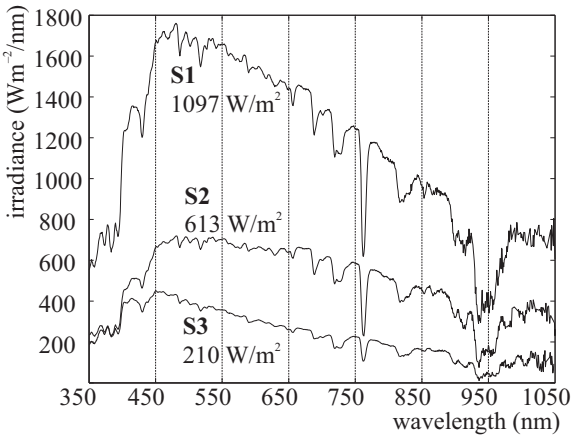

Figure 5.6: Representation of three spectra measured at different irradiance values

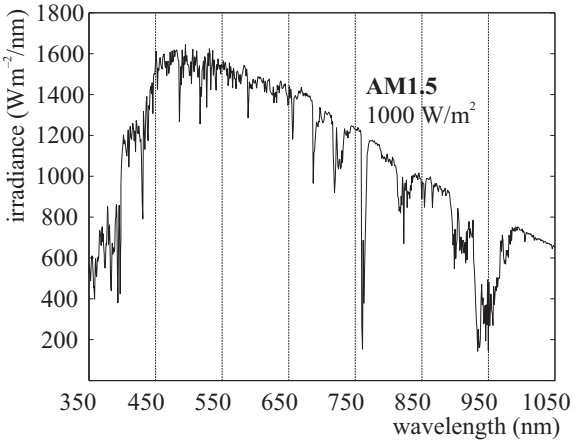

Figure 5.7: Graphical representation of AM1.5

More information from the original spectral is thus taken into account. Moreover, the spectral range has been split into intervals. Depending on the spectral response of each photovoltaic technology each interval will have more or less influence in the power output of the cell or module. For example, Figure 5.6 shows three typical spectral measurements taken with a spectroradiometer at different times and days. Figure 5.7 shows the AM1.5 spectra as it is defined by IEC 60904–3 [1] (it is only plotted between 350 nm and 1050 nm). For each spectrum in Figure 5.6, Table 5.7 shows its

	AM1.5	S1	S2	S3
Date		16/03	02/03	02/02
Time		13:46	16:31	09:11
$G(\mathrm{W/m^2})$	1000	1097	613	210
350-1050	1.876	1.892	1.860	1.753
350-450	3.032	3.029	3.023	3.012
450-550	2.481	2.481	2.479	2.473
550-650	2.069	2.071	2.069	2.063
650-750	1.776	1.776	1.775	1.772
750-850	1.552	1.552	1.551	1.549
850-950	1.391	1.390	1.390	1.394
950-1050	1.236	1.237	1.234	1.233
350-400	3.293	3.291	3.289	3.287
400-450	2.911	2.908	2.907	2.903
450-500	2.610	2.609	2.608	2.606
500-550	2.362	2.362	2.361	2.361
550-600	2.157	2.158	2.158	2.157
600-650	1.984	1.985	1.984	1.982
650-700	1.838	1.838	1.838	1.837
700-750	1.711	1.710	1.710	1.709
750-800	1.599	1.599	1.598	1.597
800-850	1.503	1.504	1.504	1.503
850-900	1.418	1.418	1.418	1.418
900-950	1.347	1.346	1.346	1.348
950-1000	1.267	1.268	1.269	1.266
1000-1050	1.210	1.210	1.208	1.209

Table 5.7: APE values (eV) at different intervals for the three spectra and for AM1.5 spectrum

date and time values, its irradiance and the APE values. We have calculated the global APE between 350 nm and 1050 nm, the 7 APE values for each 100–nm interval and the 14 APE values for each 50–nm interval. All these calculations have been also performed for the standard AM1.5 spectrum.

We propose to divide the range between 350 nm and 1050 nm into 7 intervals of 100 nm after doing several trials (full range, 100 nm, 50 nm and 25 nm). Note that if the length of the interval is very short the differences between values of APE could not be significant enough. An optimal partition of the range should take into account the absorption bands of the main

gases with presence in the atmosphere. It would be possible to use a genetic algorithm to determine these intervals by searching a good solution. However, this is beyond the scope of this thesis.

In summary, for each table of 1024 wavelength–irradiance pairs returned by the spectroradiometer we will obtain a vector with the 7 values of APE at the 100–nm intervals from 350 nm to 1050 nm, which will be used as input of the MLP instead of the raw values.

5.6.2 Selection of spectra using Kohonen maps

Thousand of *I–V* curves have been stored. Only those samples measured at irradiance above 200 W/m^2 have been taken into account for our study. The irradiance is measured at the beginning and end of the acquisition of the *I–V* curve. Only samples with a difference between these measurements of less than 1 % were used. After this selection the number of available *I–V* curves has been reduced to a total of 5822.

In order to select a set of *I–V* curves to train the MLP, a random selection (100 *I–V* curves among the 5822 available measurements) can be performed. However, there are better alternatives which could improve results. One of them would be to classify the measurements into 100 clusters. Once all the *I–V* curves have been classified, the set of curves for training the network can be determined by selecting one element of each group (the closest to the prototype of the cluster).

This classification can be performed using a self–organizing map (SOM). This is a special type of neural network using unsupervised learning and developed by Kohonen [31]. This type of network is able to detect correlations and regularities among patterns. The network groups together samples with similar characteristics taking into account their features. This can be done in an unsupervised manner. The user only needs to specify the number of groups.

The idea of using a Kohonen network in the preparation phase of the multilayer perceptron network is not new. Boznar and Mlakar [32] have developed a selection technique based on the Kohonen network to find clusters of similar input patterns and to take only a representative pattern of each cluster in order to train a MLP. In our case, it could be interesting to classify the initial set of measurements attending the spectrum associated to each *I–V* curve (this selection has actually been performed taking into account the 7 values of APE at each 100–nm interval from 350 nm to 1050 nm). As we want to select the 100 most representative cases, the output layer must have 100 neurons. These neurons have been arranged in a two–dimensional lattice containing 10 rows and 10 columns. The input layer of the Kohonen

11	24	66	71	42	92	89	64	52	60
18	44	86	75	62	50	57	89	68	38
40	65	70	80	68	69	74	68	92	49
72	23	64	76	83	72	34	84	51	59
46	59	61	69	73	60	83	79	86	62
19	34	42	48	43	94	78	101	66	45
23	27	61	81	76	75	104	112	60	63
18	43	24	35	76	65	110	118	62	42
38	57	51	70	72	79	59	41	44	57
18	13	15	17	56	40	39	21	12	49

Table 5.8: Distribution of the input patterns into 100 classes using a 10×10 output lattice.

network contains 7 neurons, one per each different interval of 100 nm. The network has been trained with the complete set of spectral measurements (exactly 5822 spectra). After 5000 iterations, the input vectors were classified getting a good distribution among the 100 output neurons. Table 5.8 reports the number of input patterns classified in each class.

Due to the topological property of the SOM network the intrinsic relationships between different spectral measurements are captured. If some weather parameter has a high effect on the shape of the spectrum, the spectra measured with similar values of this parameter will be classified as the same class or as neighbour classes in the lattice. For example, all the spectral measurements taken with an air temperature higher than 25 °C are classified by the SOM into neighbour neurons of the lattice (their associated classes are plot in Figure 5.8 with circles). On the other hand, all the measurements with an air temperature lower than 15 °C are classified into a different area within the lattice (these classes are marked with stars). A few classes present an overlap within boundary samples.

Another example of this property of Kohonen maps can be obtained by studying the relative humidity. Figure 5.9 shows the results obtained when all the spectral measurements with relative humidity higher than 70 % are selected and the Kohonen map is used to locate the position of their classes in the lattice (circles in Figure 5.9). If all the measurements with a relative humidity lower than 35 % are selected, the associated classes have been mapped into different areas within the lattice (stars in Figure 5.9). As in the previous example there are a few overlaps.

At this point, we are able to select the 100 most representative measurements from the initial set of records. In order to perform this task, for each class of the 10×10 lattice, we must identify the record whose spectrum is

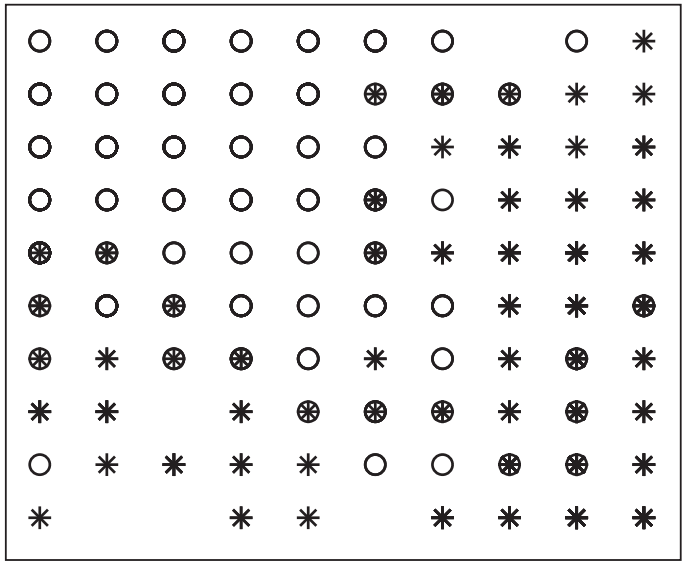

Figure 5.8: Classes associated to spectra measured at air temperature higher than 25 °C (circles) versus spectra at air temperature lower than 15 °C (stars).

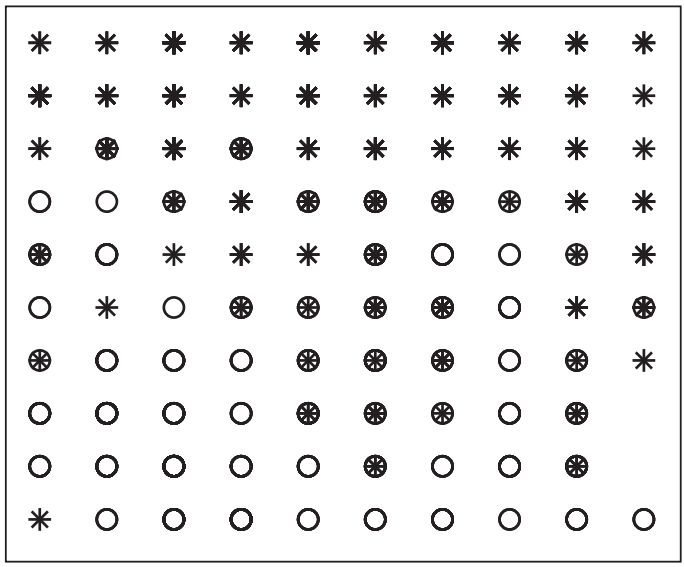

Figure 5.9: Classes associated to spectra measured at a relative humidity greater than 70 % (circles) versus spectra measured at a relative humidity lower than 35 % (stars).

closer to the prototype of that class (i.e. the record whose array of APEs has the minimum Euclidean distance to the vector weight of each neuron of the output layer). Once we have selected these 100 records we are ready to train the MLP using this set of measurements. The rest of measurements in our dataset will be used after the training in order to test the generalization performance of the neural network (i.e. how it behaves when previously unseen patterns are presented to that network).

5.6.3 Multilayer perceptron training

On the one hand, as our aim is to measure the increase of performance due to the incorporation of spectral data to the neural network, we must take into account two different sets of samples: GT (5822 samples with an *I–V* curve with only irradiance and module temperature) and SP (5822 samples with an *I–V* curve, irradiance, module temperature and spectrum). On the other hand, using the Kohonen self–organizing map as we explained in the previous section, we have split each previous set of samples into two sets: the *Kohonen training records* (100 samples for training the network) and *Kohonen testing records* (5722 samples for testing the network). However, in order to illustrate the advantages of using the Kohonen maps versus a random selection, both sets of measurements have been also splitted following a random strategy: a set called *random training records* (also with 100 measurements) and another set called *random testing records* (with the 5722 remaining measurements). Table 5.9 summarizes the sets generated using all these possibilities.

The next step is the splitting of each record into 100 training patterns, one for each *I–V* point of the curve as it has been described in section 4: for each curve from the training set we will get as many patterns as points belong to that curve. Therefore, each input pattern of the MLP contains the measure of irradiance and module temperature, the 7 values of APE at 100–nm intervals and the voltage component of each *I–V* pair. In contrast, the output for such pattern only consists of the current component of each *I–V* pair. This process has been performed for GT_Ra, GT_Rb, GT_Ka, GT_Kb, SP_Ra, SP_Rb, SP_Ka and SP_Kb. Then, 4 training sets of patterns and 4 testing sets of patterns have been used.

In order to determine the optimal number of neurons in the hidden layer, we have repeated the training process several times, ranging from 2 hidden units to 8 hidden units. However, as each execution of the training algorithm is different we must repeat the process a significant number of times (in our case we have repeated each possibility 10 times). In summary, we have 7 different topologies (from 2 to 8 hidden units) and each one will be trained 10 times (actually 40 times taking into account that we have 4 training sets).

	GT	5822 records without spectra
random	GTRa	100 I–V curves with irradiance and temperature selected randomly for training
	GTRb	5722 I–V curves with irradiance and temperature for testing
Kohonen	GTKa	100 I–V curves with irradiance and temperature selected by Kohonen for training
	GTKb	5722 I–V curves with irradiance and temperature for testing
	SP	5822 records with spectra
random	SPRa	100 I–V curves with irradiance, temperature and APE values selected randomly for training
	SPRb	5722 I–V curves with irradiance, temperature and APE values for testing
Kohonen	SPKa	100 I–V curves with irradiance, temperature and APE values selected by Kohonen for training
	SPKb	5722 I–V curves with irradiance, temperature and APE values for testing

Table 5.9: Description of the training and testing sets

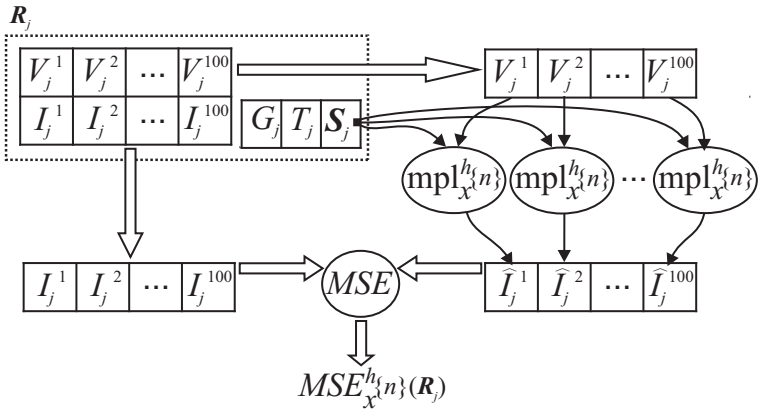

Figure 5.10: Scheme of the calculus of MSE of a trained network over a record of the testing set.

We obtained a different trained MLP for each combination. Let $mlp_x^h\{n\}$ be the trained multilayer perceptron obtained in the n-th execution of the training routine using h neurons in the hidden layer and the training set x (where $n = 1 \ldots 10$, $h = 2 \ldots 8$ and x can be $\mathrm{GT_R a}$, $\mathrm{GT_K a}$, $\mathrm{SP_R a}$ or $\mathrm{SP_K a}$). Now the performance of each MLP must be evaluated.

The generalization error of each MLP can be computed using all the curves of our dataset not seen during the training phase, i.e. the sets in Table 5.9 referred as $\mathrm{GT_R b}$, $\mathrm{GT_K b}$, $\mathrm{SP_R b}$ or $\mathrm{SP_K b}$, each one with the 5722 I–V curves which are independent from the training set of records. Given a trained network $mlp_x^h\{n\}$ and a target record $\boldsymbol{R}_j = \{< \boldsymbol{V}_j, \boldsymbol{I}_j > | G_j, T_j, \ldots\}$ from the testing set (where $< \boldsymbol{V}_j, \boldsymbol{I}_j >$ is an I–V curve measured at specific conditions, its associated approximation by the network (output curve) must be computed (see Figure 5.10).

Fixing the conditions of the measurement $(G_j, T_j, \ldots, V_j^p)$ at the network input, and varying the fictitious voltage input V_j^p (using the voltage component of each I–V point p of the target curve), the network will return a sequence of current values $\hat{I}_j^p$ defined as:

$$\hat{I}_j^p = mlp_x^h\{n\}(G_j, T_j, \ldots, V_j^p) \qquad p = 1, \ldots, 100$$

The output curve $< \boldsymbol{V}_j, \hat{\boldsymbol{I}}_j >$ will be the list of points comprising the voltage components of the target curve and the current values returned by the network. The mean squared error of the differences between the current components $MSE(\boldsymbol{I}_j, \hat{\boldsymbol{I}}_j)$ is the error of the trained network $mlp_x^h\{n\}(\boldsymbol{R}_j)$ for the record $\boldsymbol{R}_j$ of the testing set.

		Mean squared error (%)					
		without spectrum			with spectrum		
	h	mean	min	max	mean	min	max
random selection	2	0.78	0.35	4.6	0.28	0.27	0.28
	3	0.38	0.33	0.45	35	0.23	350
	4	0.38	0.33	0.47	93	0.29	640
	5	0.38	0.33	0.46	1.3	0.45	3.8
	6	0.46	0.33	0.83	4.9	0.42	35
	7	0.76	0.33	2.0	74	0.79	720
	8	0.40	0.32	0.67	7.4	0.96	27
		without spectrum			with spectrum		
	h	mean	min	max	mean	min	max
Kohonen selection	2	0.50	0.28	2.5	0.13	0.13	0.13
	3	0.27	0.27	0.28	0.13	0.11	0.17
	4	0.27	0.27	0.28	0.14	0.10	0.20
	5	0.27	0.27	0.29	0.13	0.12	0.16
	6	0.30	0.27	0.38	0.19	0.12	0.26
	7	0.28	0.27	0.29	0.31	0.11	0.99
	8	0.29	0.27	0.35	0.67	0.17	2.0

Table 5.10: Mean, maximum and minimum MSE (%) for each possible combination considered in this experiment

$$MSE_x^j\{n\}(\boldsymbol{R}_j) = MSE(\boldsymbol{I}_j, \hat{\boldsymbol{I}}_j)$$

Finally, the generalization error of the trained network is the mean value of MSEs for all the curves in the testing set (where N is the number of records stored in the training set):

$$MSE_x^h\{n\} = \frac{1}{N}\sum_{j=1}^{N} MSE_x^h\{n\}(\boldsymbol{R}_j) = \frac{1}{N}\sum_{j=1}^{N} MSE(\boldsymbol{I}_j, \hat{\boldsymbol{I}}_j)$$

Numerical values for these MSEs are summarized in Table 5.10.

For each combination of training set (GT_Ra, GT_Ka, SP_Ra or SP_Ka) and number of hidden units ($h = 2, \ldots, 8$), the maximum, minimum and mean value among the 10 repetitions of the same configuration have been stated . In addition, the mean values of MSE for the different training sets (except for SP_Ra) have been plotted as a function of the number of hidden units in Figure 5.11.

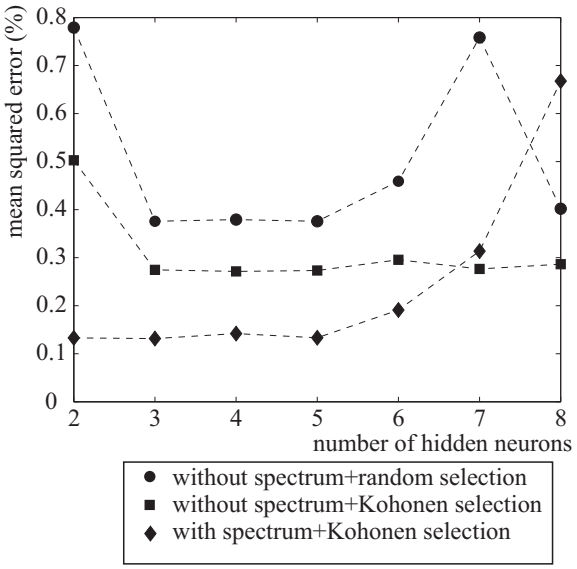

Figure 5.11: MSE (%) as a function of the number of hidden units for different combinations.

Several conclusions can be stated from these results. First, some MLPs trained with spectral information and using random selection of the records ($SP_{R}a$) present unacceptable results (relative MSE values greater than 300 %). The MSE over the testing records is completely off and significantly worse than those obtained by the MLPs without spectral information. In these cases the MLP has not been able to find the global minimum during the training process and eventually the maximum number of iterations is reached. This means that, with the introduction of the spectral information, the subjacent function to optimize presents a bad conditioned surface. Depending on the starting point, the training algorithm could find or not the true global minimum.

Second, the MLPs trained without spectral information improve their performance by means of the Kohonen based selection. This improvement is due to the use of the previous selection. Typical samples, which are very similar between them, might be classified into the same cluster. Atypical samples with low frequency might be classified into their own class. Getting only one example per cluster, the probability of selecting a typical example is equal to the probability of selecting an atypical example. We are thus avoiding over–fitting of the network with the typical examples. This problem happens when we perform a random sample selection, which follows the original distribution of the data. In some sense, the Kohonen based selection could be seen as a probability normalization process.

Third, performance of the results is enhanced with the combination of both a Kohonen based sample selection and the introduction of spectral information (SP_Ka) as input to the MLPs.

Finally, as we can see in Figure 5.11, the best results for all cases are achieved with a number of neurons in the hidden layer between 3 and 5 (similar number of hidden units has been used in previous works in the literature).

In summary, the introduction of spectral information into the training process of the multilayer perceptron improves the global generalization performance of the network, but only if a previous selection of the most representative spectra has been performed using the Kohonen self–organizing map.

5.6.4 Results for spectral input data

In this section a more detailed study curve by curve is performed. We will now get the best trained network without spectral information (the one with the smallest MSE value, denominated MLP_{GT}) and the best trained network with spectral information (represented by MLP_{SP}). We then compare their individual curve results over the testing set of samples. Taken into account the complete testing set (5722 samples not selected for training), the MLP_{SP} returns a better approximation (closer to the measured curve) than MLP_{GT} in a total of 3422 examples (59.8 %), whereas in the 2300 remaining examples (40.2 %) MLP_{GT} is better. Although the global mean MSE is smaller for the MLP trained with spectral information, if we study the number of I–V curves in which the introduction of the spectrum into the network has implied an improvement, the results are not so good.

In order to illustrate the behaviour of both models, let us study a few examples (5 selected I–V curves) from among the 5722 records of the testing set. Figure 5.12.a is a typical example of I–V curve acquired at a high irradiance value. It was taken at 13:21 on 14 February, 2011 with a global irradiance of 1032 W/m^2, a module temperature of 34.1 °C and a global APE value (from 350 nm to 1050 nm) of 1.885 eV. In most of these cases the visual difference between the true measured curve, the approximation given by MLP_{GT} and the approximation given by MLP_{SP} is very small. In the same graphic the measured curve and both approximations have been plotted, and it is difficult to highlight the best performer. It is necessary to zoom in to be able to see a small difference between them. Figure 5.12.b presents a zoom of the region of the maximum power point. We can see that the MLP with spectral information is closer to the measured curve than the MLP without spectrum. Actually the MSE of MLP_{GT} for this curve is 0.003 % whereas

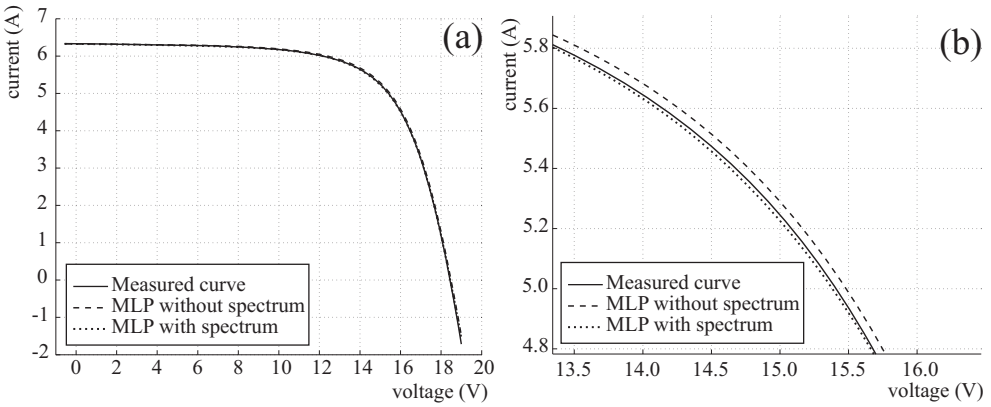

Figure 5.12: Results of the measurement acquired on 14 February (a). Zoom detail of the knee of the curve (b).

the MSE of MLP_{SP} is 0.0002 %.

In last example MLP_{SP} has a better behaviour than MLP_{GT}. However, if we analyze more examples we can realize that there are many cases where the approximation given MLP_{GT} is closer to the measured curve than the output given by MLP_{SP}, especially when the curve has been acquired at a high irradiance value. Figure 5.13.a shows an example of this fact. This I–V curve has been acquired at 12:45 on 9 April, 2011 with a global irradiance of 961 W/m^2, a module temperature of 59.2 °C and with a spectrum with an APE value equal to 1.888 eV. Although the difference is not very large, a zoom around the knee of the curve shows that the values given by MLP_{GT}, trained without spectral information are closer to the measured values (MSE=0.0003 %) than those ones given by MLP_{SP} (MSE=0.013 %), trained with spectral information, see Figure 5.13.b.

When focusing on I–V curves taken under low irradiance values the improvement achieved with the introduction of spectral measurements can be appreciated. For example, Figure 5.14 is an I–V curve acquired at 18:01 on 2 March, 2011 with a global irradiance of 231 W/m^2, a module temperature equal to 20.1 °C, and with an APE value of 1.819 eV. As it can be seen with a naked eye, the approximation given by the MLP trained with spectral data is significantly better (MSE=0.06 %) than the approximation given by the one without spectral data (MSE=3 %).

In most of the I–V curves with a low irradiance the previous situation is often found. For instance, the I–V curve corresponding to 19 April, 2011 at 15:44, with $G = 437$ W/m^2, $T_m = 30.2$ °C and APE=1.928 eV (Figure 5.15) is another example that confirms that the behaviour of MLP_{SP} is better than the behaviour of MLP_{GT} in cases with low irradiance.

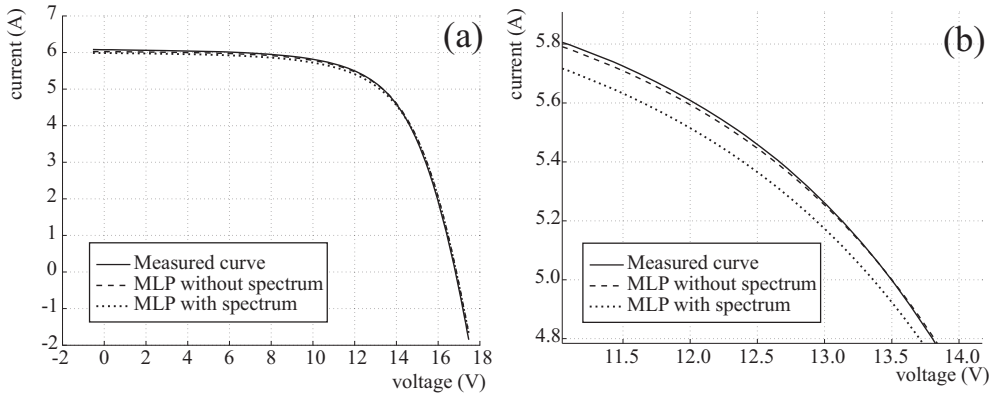

Figure 5.13: Results of the measurement acquired on 9 April (a). Zoom detail of the knee of the curve (b).

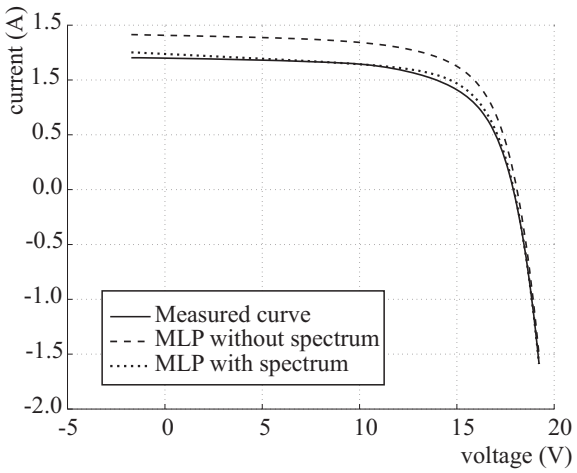

Figure 5.14: Results of the measurement acquired on 2 March.

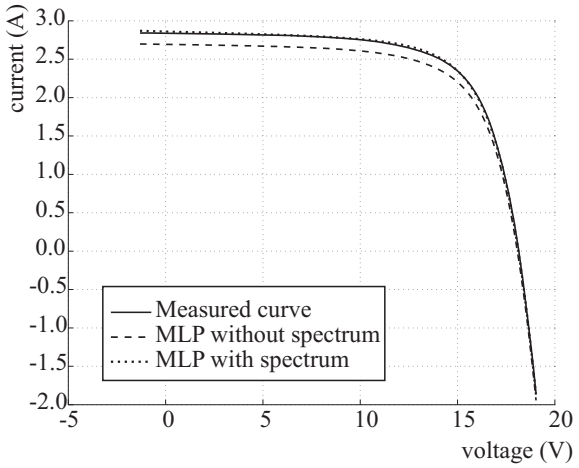

Figure 5.15: Results of the measurement acquired on 19 April.

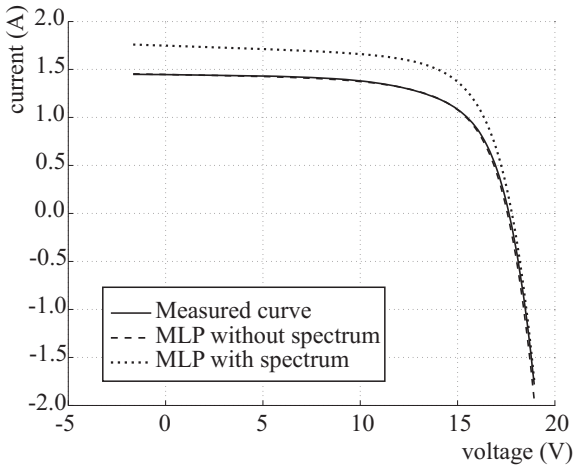

Figure 5.16: Results of the measurement acquired on 21 March.

However, there are a few exceptions, even at a low value of irradiance, where the behaviour of networks trained with spectral data is anomalous. Figure 5.16 shows an I–V curve measured at 11:21 on 21 March, 2011 with $G = 231$ W/m^2, $T_m = 28.2$ °C and APE=1.943 eV. Whereas MLP_{GT} has obtained a very good result (MSE=0.006 %), MLP_{SP} gives an approximation quite far from the measured I–V curve (MSE=4 %).

We started this section stating that only in around 60 % of the cases the approximation given by MLP_{SP} is better than the approximation given by MLP_{GT}. However, if we only take into account the I–V curves measured at irradiance lower than 500 W/m^2 (there are 1901 samples that satisfy this condition), then the approximation given by MLP_{SP} has a mean squared error

lower than the approximation given by $\mathrm{MLP_{GT}}$ in a total of 1685 cases. Consequently, at low irradiance values (< 500 W/m^2), in 89 % of the cases, the introduction of spectral information in the network implies an improvement of the results. However, if we take only I–V curves acquired at irradiance values greater than 800 W/m^2 that percentage is only 50 %.

The spectral differences between clear–sky days are very little and the irradiance and cell temperature are the most important factors which determine the I–V curve. The irradiance is high throughout the day in all these cases. However, on cloudy days, when curves are measured at low irradiance values, the variability of the spectral distribution is greater: there are different types of clouds, clouds at different altitudes in the atmosphere and with different shapes and patterns. This fact implies that at low irradiances, other factors like the spectral distribution have more relative weight in the shape and height of the I–V curve.

5.7 Conclusions

A multilayer perceptron neural network has been used to characterise the I–V curve of photovoltaic modules. First, the angle of incidence and the instantaneous clearness has been incorporated as inputs to the network in order to generate the I–V curve under different conditions. A fictitious neuron has been added to the input layer to represent the voltage coordinate of each point of the curve whereas there is only one neuron in the output layer representing the associated current. In some cases, the introduction of these new parameters could imply a improvement of the results.

The spectral distribution measurement has also been incorporated as an input to the neural network. In order to represent the spectral information with a suitable format, the raw table of values returned by the spectroradiometer has been converted into a vector with the 7 values of APE at the 100–nm intervals from 350 nm to 1050 nm.

The 100 most representative measurements have been selected from all records stored in the database. It has been proved that a selection based on a previous classification using a Kohonen self–organizing map is fundamental when spectral data is incorporated to the network (otherwise the network might return unacceptable values). Only by using this Kohonen based selection, the performance of the network trained with spectral information improves the performance of the network trained without spectral information.

A detail study curve by curve has also been performed over a few examples among the testing set. In most of the curves acquired at high irradiance

values, the introduction of spectral data as an input to the network does not imply a significant improvement of the results. Even in many cases, the approximation given by the network trained without spectral information is better than the one obtained with the network trained using spectral data. However, if we take only into account I–V curves acquired under low irradiance values the network trained with spectral information gives better results with most of the curves.

The methodology proposed in this work can be applied to other photovoltaic technologies, such as poly–crystalline silicon, amorphous silicon or cadmium telluride. A new set of measurements has been started in order to analyze the improvement achieved on these technologies, which have a spectral response narrower than mono–crystalline silicon.

In this thesis, only the multilayer perceptron neural network has been used in order to learn the behaviour of the module. However, we want to focus future research to test another types of neural networks suitable for the same purpose and compare the results obtained among them. Such networks might include radial basis function networks, growing neural gas networks and vector support machines.

We want to focus future work to search for a better partition of the spectral range taking into account the absorption bands of the main gases with presence in the atmosphere. Another approach could be the use of a genetic algorithm in order to search a better partition of the spectral range.

Bibliography

[1] IEC 60904–3. *Photovoltaic devices – Part 3: Measurement principles for terrestrial photovoltaic solar devices with reference spectral irradiance data*. International Electrotechnical Commission, Geneva (Switzerland), 2nd edition, 2008. ISBN 978-2-8318-9705-9.

[2] W. Herrmann, H. Becker, and W. Wiesner. Round robin test on translation procedures for measured PV generator characteristics. In *14th European Photovoltaic Solar Energy Conference*, pages 203–206, Barcelona (Spain), 1997.

[3] J.D. Sandstrom. Method for predicting solar cell current voltage curve characteristics as a function of incident solar intensity and cell temperature. Technical Report 32–7742, Jet Propulsion Laboratory, California Institute of Technology, National Aeronautics and Space Administration (NASA), Pasadena (CA, USA), 1967.

[4] IEC 60891. *Procedures for temperature and irradiance corrections to measure I–V characteristics of crystalline silicon photovoltaic devices*. International Electrotechnical Commission, Geneva (Switzerland), 2nd edition, 2009. ISBN 978-2-88910-316-4.

[5] G. Blaesser and E. Rossi. Extrapolation of outdoor measurements of PV array *I–V* characteristics to standard test conditions. *Solar Cells*, 25(2):91–96, 1988. doi: 10.1016/0379-6787(88)90014-2.

[6] A.J. Anderson. Photovoltaic translation equations: A new approach. Technical Report NREL/TP–411–20279, National Renewable Energy Laboratory (NREL), Golden (CO, USA), 1996.

[7] B. Marion. A method for modeling the current–voltage curve on a PV module for outdoor conditions. *Progress in Photovoltaics: Research and Applications*, 10(3):205–214, 2002. doi: 10.1002/pip.403.

[8] B. Marion, S. Rummel, and A. Anderberg. Current–voltage curve translation by bilinear interpolation. *Progress in Photovoltaics: Research and Applications*, 12(8):593–607, 2004. doi: 10.1002/pip.551.

[9] IEC 60904–7. *Photovoltaic devices – Part 7: Computation of the spectral mismatch correction for measurements of photovoltaic devices*. International Electrotechnical Commission, Geneva (Switzerland), 3rd edition, 2008. ISBN 978-2-88910-324-9.

[10] J.I. Rosell and M. Ibáñez. Modelling power output in photovoltaic modules for outdoor operating conditions. *Energy Conversion & Management*, 47(15–16):2424–2430, 2006. doi: 10.1016/j.enconman.2005.11.004.

[11] K. Ishaque, Z. Salam, and H. Taheri. Simple, fast and accurate two–diode model for photovoltaic modules. *Solar Energy Materials & Solar Cells*, 95(2):586–594, 2011. doi: 10.1016/j.solmat.2010.09.023.

[12] C. Domínguez, I. Antón, and G. Sala. Multijunction solar cell model for translating I–V characteristics as a function of irradiance, spectrum, and cell temperature. *Progress in Photovoltaics: Research and Applications*, 18(4):272–284, 2010. doi: 1010.1002/pip.965.

[13] J.C. Patra. Neural network–based model for dual–junction solar cells. *Progress in Photovoltaics: Research and Applications*, 19(1):33–44, 2011. doi: 10.1002/pip.985.

[14] E. Karatepe, M. Boztepe, and M. Colak. Neural network based solar cell model. *Energy Conversion & Management*, 47(9–10):1159–1178, 2006. doi: 10.1016/j.enconman.2005.07.007.

[15] M.C. Di Piazza, M. Pucci, A. Ragusa, and G. Vitale. Analytical versus neural Real–Time simulation of a photovoltaic generator based on a DC–DC converter. *IEEE Transactions on Industry Applications*, 46 (10):2501–2510, 2010. doi: 10.1109/TIA.2010.2072975.

[16] L. Hontoria, J. Aguilera, F. Almonacid, G. Nofuentes, and P. Zufiria. Artificial neural networks applied in PV systems and solar radiation. In S. Kalogirou, editor, *Artificial Intelligence in Energy and Renewable Energy Systems*, chapter 5, pages 163–200. Nova Science Publishers Inc, UK, 2006. ISBN 978-1-60021-261-1.

[17] F. Almonacid, C. Rus, L. Hontoria, M. Fuentes, and G. Nofuentes. Characterisation of Si–crystalline PV modules by artificial neural networks. *Renewable Energy*, 34(4):941–949, 2009. doi: 10.1016/j.renene.2008.06.010.

[18] F. Almonacid, C. Rus, P.J. Pérez, and L. Hontoria. Estimation of the energy of a PV generator using artificial neural network. *Renewable Energy*, 34(12):2743–2750, 2009. doi: 10.1016/j.renene.2009.05.020.

[19] F. Almonacid, C. Rus, L. Hontoria, and F.J. Muñoz. Characterisation of PV CIS module by artificial neural networks. A comparative study with other methods. *Renewable Energy*, 35(5):973–980, 2010. doi: 10.1016/j.renene.2009.11.018.

[20] L.E. Zárate, L.V.B.M. Neto, D.A. Soares, and F.R. Bittencout. Artificial neural networks applied for representation of curves Current–Voltage of photovoltaic modules. In *IEEE International Conference on Industrial Informatics*, pages 1644–1649, Daejeon (Korea), 2008. doi: 10.1109/INDIN.2008.4618367.

[21] D. Elizondo, G. Hoogenboom, and R.W. McClendon. Development of a neural network model to predict daily solar radiation. *Agricultural and Forest Meteorology*, 71(1–2):115–132, 1994. doi: 10.1016/0168-1923(94)90103-1.

[22] A. Yona, T. Senjyu, A.Y. Saber, T. Funabashi, H. Sekine, and C.H. Kim. Application of neural network to 24–hour–ahead generating power forecasting for PV system. In *IEEE Power and Energy Society General Meeting*, pages 1–6, Pittsburgh (PA, USA), 2008. doi: 10.1109/PES.2008.4596295.

[23] L. Mora–López, M. Piliougine, J. Carretero, and M. Sidrach–de–Cardona. Integration of statistical and machine learning models for short–term forecasting of the atmospheric clearness index. In *5th Biennial Meeting of International Congress on Environmental Modelling and Software (iEMSs)*, Ottawa (Canada), 2010.

[24] L. Zhang and Y.F. Bai. On–line neural network training for maximum power point tracking of PV power plant. *Transactions of the Institute of Measurement and Control*, 30(1):77–96, 2008. doi: 10.1177/0142331207076374.

[25] K.H. Chao, C.J. Li, and M.H. Wang. A maximum power point tracking method based on extension neural network for PV systems. In

6th International Symposium on Neural Networks on Advances in Neural Networks, volume 1, pages 745–755, Wuhan (China), 2009. doi: 10.1007/978-3-642-01507-6_84.

[26] J.C. Principe, J.R. Euliano, and W.C. Lefebvre. *Neural and Adaptive Systems: Fundamentals through Simulations*. John Wiley & Sons, New York (NY, USA), 2000. ISBN 978-0-471-35167-2.

[27] H. Mekki, A. Mellit, S.A. Kalogirou, A. Messai, and G. Furlan. FPGA–based implementation of a real time photovoltaic module simulator. *Progress in Photovoltaics: Research and Applications*, 18(2):115–127, 2010. doi: 10.1002/pip.950.

[28] I. Reda and A. Andreas. Solar position algorithm for solar radiation applications. Technical Report NREL/TP–560–34302, National Renewable Energy Laboratory (NREL), Golden (CO, USA), 2008.

[29] T. Minemoto, S. Nagae, and H. Takakura. Impact of spectral irradiance distribution and temperature on the outdoor performance of amorphous Si photovoltaic modules. *Solar Energy Materials & Solar Cells*, 91(10): 919–923, 2007. doi: 10.1016/j.solmat.2007.02.012.

[30] T. Minemoto, Y. Nakada, H. Takahashi, and H. Takakura. Uniqueness verification of solar spectrum index of average photon energy for evaluating outdoor performance of photovoltaic modules. *Solar Energy*, 83 (8):1294–1299, 2009. doi: 10.1016/j.solener.2009.03.004.

[31] T. Kohonen. The self–organizing map. *Proceedings of the IEEE*, 78(9): 1464–1480, 1990. doi: 10.1109/5.58325.

[32] M.Z. Boznar and P. Mlakar. Use of neural networks in the field of air pollution modeling. *Air Pollution Modeling and Its Application XV*, pages 375–383, 2002.

Chapter 6

Conclusiones

En esta tesis se planteó como objetivo el desarrollo de una metodología de medida, caracterización y simulación de módulos fotovoltaicos que pudiera ser de utilidad para los investigadores e ingenieros del campo de la tecnología solar fotovoltaica. Para la parte de medida, en el marco de esta tesis, se ha desarrollado un nuevo sistema de medida de curvas I–V para módulos fotovoltaicos. En la parte de caracterización y simulación, se ha propuesto un modelo basado en redes neuronales que permite extrapolar estas curvas a distintas condiciones reales de funcionamiento. Así, los objetivos que se plantearon a la hora de elaborar esta tesis se han alcanzado en los trabajos que se presentan en los distintos capítulos de la misma.

El primer objetivo planteado era el desarrollo de una metodología de medida de las curvas I–V que resolviera los problemas detectados en los métodos que se están utilizando en la actualidad. En concreto, se ha dado respuesta a la necesidad de obtener los valores de los dos parámetros que configuran estas curvas, a saber, corriente y tensión, de manera simultánea.

Para ello, en el capítulo segundo de esta tesis se ha propuesto un nuevo sistema de medida de las curvas I–V de módulos fotovoltaicos. El sistema propuesto está basado en la utilización de una carga electrónica de cuatro cuadrantes y dos multímetros digitales sincronizados con un generador de ondas que crea una señal cuadrada para disparar ambos multímetros. Este método de sincronización asegura que las medidas de tensión y corriente se efectúan de manera simultánea; esto no se asegura con otros métodos previamente usados que utilizan sincronización vía GPIB.

La aplicación de control que se ejecuta en el ordenador principal permite al usuario configurar y definir varias campañas de medida para diferentes módulos. Además, estas medidas pueden ser visualizadas y exportadas de manera remota a través de una interfaz web amigable.

También se pueden estimar los parámetros eléctricos de cada módulo

medido. Se ha hecho un análisis de incertidumbre del cálculo de los mismos. Este análisis incluye tanto errores debidos a la resolución y precisión de los equipos electrónicos como los debidos a los métodos utilizados para estimar los parámetros eléctricos.

La metodología propuesta permite además la medida, caracterización y simulación del comportamiento de módulos fotovoltaicos en exteriores. Normalmente, los parámetros eléctricos de los módulos se miden en condiciones controladas de laboratorio (indoor testing). Sin embargo, las medidas en exteriores proporcionan importantes ventajas, como es la utilización de fuentes de luz artificial, la mayor homogeneidad de la fuente solar, y lo que es más importante, el tamaño de las muestras que se miden no está limitado.

Relacionado con el primer objetivo que se planteó en esta tesis, en el capítulo tercero se propone utilizar el lenguaje XML para el formato de los datos registrados en laboratorios fotovoltaicos. Este formato puede contribuir a una estandarización de los datos que se utilizan para la caracterización de módulos fotovoltaicos por distintos laboratorios de medida. Esto facilitará el intercambio de información entre estos laboratorios. Además, se facilita el desarrollo de análisis y distintos tipos de test (round–robin) por distintos laboratorios utilizando bases de datos comunes. Para la definición de estos esquemas se propone una estructura jerárquica de los elementos y parámetros que se utilizando normalmente en la medida y caracterización de dispositivos fotovoltaicos. Así, la propuesta que se hace en el capítulo tercero puede ser muy útil para el intercambio de datos entre investigadores, fabricantes y laboratorios de medida.

El segundo objetivo que se planteó en esta tesis fue la caracterización y simulación de módulos fotovoltaicos utilizando redes neuronales, como alternativa a los métodos algebraicos y numéricos que se han venido utilizando hasta la fecha.

Para la caracterización de la curva I–V de los módulos fotovoltaicos se ha propuesto la utilización de un perceptrón multicapa. Se han evaluado cómo contribuyen a esta caracterización distintos parámetros de entrada, como son el ángulo de incidencia, el índice de transparencia atmosférico y la distribución espectral de la radiación. Para poder trabajar con los pares de corriente y tensión de una curva, se ha añadido una neurona ficticia a la capa de entrada para representar la coordenada de tensión de cada punto de la curva, mientras sólo se ha utilizado una neurona en la capa de salida para representar la corriente asociada. Para poder representar la información espectral, la tabla de valores que suministra el espectroradiómetro se ha convertido en un vector que tiene siete valores de APE, correspondientes a los 7 intervalos de 100–nm que hay desde 350 nm a 1050 nm.

Se han seleccionado las 100 muestras más representativas de entre to-

das las medidas registradas en la base de datos. Se ha comprobado que una selección de medidas basada en una clasificación previa utilizando los mapas auto–organizados de Kohonen es fundamental para poder incorporar los datos de medidas espectrales en la red neuronal. Sólo utilizando esta selección previa, el funcionamiento de la red neuronal entrenada con información espectral mejora al funcionamiento de la red neuronal entrenada sin esa información espectral.

En el capítulo quinto se ha hecho también un estudio detallado de algunas curvas seleccionadas de entre las pertenecientes al conjunto de test. Como conclusión se puede afirmar que para la mayoría de las curvas adquiridas a valores de irradiancia altos, la introducción del espectro como dato de entrada no supone una mejora significativa respecto a los resultados que se obtienen cuando no se utiliza esta información. Sin embargo, si se consideran sólo las curvas adquiridas a bajos niveles de irradiancia, en la mayoría de los casos la red neuronal entrenada con información espectral funciona mejor que la que no incluye este tipo de información.

Para concluir, se puede afirmar que la metodología que se ha desarrollado en esta tesis puede ser aplicada a otras tecnologías fotovoltaicas, como son el silicio policristalino, el silicio amorfo o el telururo de cadmio.

Appendices

Appendix A

XSD Schema

```
<?xml version="1.0" encoding="utf-8" ?>
<xs:schema attributeFormDefault="unqualified" elementFormDefault="qualified" ...
xmlns:xs="http://www.w3.org/2001/XMLSchema">
    <xs:element name="pv-device-characterization">
        <xs:complexType>
            <xs:all>
                <xs:element name="pv-device-description" ...
                type="specimen-description" />
                <xs:element name="enviroment" type="environment-type" />
                <xs:element name="measurement-equipment" ...
                type="measurement-system-type" />
                <xs:element name="administrative-information" ...
                type="administrative-information" />
                <xs:element name="iv-curve-list" minOccurs="0" ...
                maxOccurs="1">
                    <xs:complexType>
                        <xs:sequence>
                          <xs:element name="iv-curve" type="iv-curve-type" ...
                          maxOccurs="unbounded" />
                        </xs:sequence>
                    </xs:complexType>
                </xs:element>
            </xs:all>
        </xs:complexType>
    </xs:element>
    <xs:complexType name="measurement-type">
        <xs:all>
            <xs:element name="value" type="xs:double" />
            <xs:element name="uncertainty" minOccurs="0">
                <xs:complexType>
                    <xs:simpleContent>
                        <xs:extension base="xs:double">
                            <xs:attribute name="coverage" ...
                            type="xs:double" default="2" />
                            <xs:attribute name="confidence" default="95">
                                <xs:simpleType>
                                    <xs:restriction base="xs:double">
                                        <xs:minInclusive value="0" />
                                        <xs:maxInclusive value="100" />
                                    </xs:restriction>
                                </xs:simpleType>
                            </xs:attribute>
```

```
                    </xs:extension>
                </xs:simpleContent>
            </xs:complexType>
        </xs:element>
    </xs:all>
    <xs:attribute name="unit" type="xs:string" />
    <xs:attribute name="magnitude" type="xs:string" />
</xs:complexType>
<xs:complexType name="electrical-parameters-type">
    <xs:all>
        <xs:element name="isc" type="measurement-type" minOccurs="0" />
        <xs:element name="voc" type="measurement-type" minOccurs="0" />
        <xs:element name="pmax" type="measurement-type" minOccurs="0" />
        <xs:element name="ipmax" type="measurement-type" minOccurs="0" />
        <xs:element name="vpmax" type="measurement-type" minOccurs="0" />
        <xs:element name="ff" type="measurement-type" minOccurs="0" />
        <xs:element name="efficiency" type="measurement-type" ...
        minOccurs="0" />
        <xs:element name="ideality-factor" type="measurement-type" ...
        minOccurs="0" />
        <xs:element name="series-resistance" type="measurement-type" ...
        minOccurs="0" />
        <xs:element name="shunt-resistance" type="measurement-type" ...
        minOccurs="0" />
        <xs:element name="parameter-list" minOccurs="0">
            <xs:complexType>
                <xs:sequence>
                    <xs:element name="measure" type="measurement-type" ...
                    minOccurs="1" maxOccurs="unbounded" />
                </xs:sequence>
            </xs:complexType>
        </xs:element>
    </xs:all>
</xs:complexType>
<xs:complexType name="dimensions-type">
    <xs:all>
        <xs:element name="height" type="measurement-type" />
        <xs:element name="width" type="measurement-type" />
        <xs:element name="depth" type="measurement-type" />
        <xs:element name="active-area" type="measurement-type" />
    </xs:all>
</xs:complexType>
<xs:complexType name="iv-array-type">
    <xs:sequence>
        <xs:element name="iv-pair" type="iv-pair-type" ...
        minOccurs="1" maxOccurs="unbounded" />
    </xs:sequence>
</xs:complexType>
<xs:complexType name="iv-pair-type">
    <xs:all>
        <xs:element name="voltage" type="measurement-type" minOccurs="1" />
        <xs:element name="current" type="measurement-type" minOccurs="1" />
        <xs:element name="power" type="measurement-type" minOccurs="0" />
        <xs:element name="irradiance" type="measurement-type" ...
        minOccurs="0" />
    </xs:all>
</xs:complexType>
<xs:complexType name="measurement-list-type">
    <xs:sequence>
        <xs:element name="measurement" type="measurement-type"  ...
        minOccurs="1" maxOccurs="unbounded" />
    </xs:sequence>
```

```
</xs:complexType>
<xs:complexType name="spectrum-type">
    <xs:sequence>
        <xs:element name="spectrum-point" type="spectrum-point-type"  ...
        minOccurs="1" maxOccurs="unbounded" />
    </xs:sequence>
</xs:complexType>
<xs:complexType name="measured-curve-type">
    <xs:all>
        <xs:element name="iv-array" type="iv-array-type" minOccurs="1" />
        <xs:element name="measurement-list" ...
          type="measurement-list-type" ...
          minOccurs="0" />
        <xs:element name="light-spectrum" type="spectrum-type" ...
        minOccurs="0" />
        <xs:element name="electrical-parameters" ...
        type="electrical-parameters-type" minOccurs="0" />
    </xs:all>
</xs:complexType>
<xs:complexType name="corrected-curve-type">
    <xs:all>
        <xs:element name="iv-array" type="iv-array-type" minOccurs="1" />
        <xs:element name="electrical-parameters" ...
        type="electrical-parameters-type" minOccurs="0" />
        <xs:element name="desired-conditons" ...
          type="measurement-list-type" ...
          minOccurs="0" />
    </xs:all>
    <xs:attribute name="correction-method" type="xs:string" ..
      use="required" />
</xs:complexType>
<xs:complexType name="iv-curve-type">
    <xs:all>
        <xs:element name="measured-curve" type="measured-curve-type" />
        <xs:element name="corrected-curve-list" minOccurs="0">
            <xs:complexType>
                <xs:sequence>
                    <xs:element name="corrected-curve" minOccurs="1" ...
                    maxOccurs="unbounded">
                        <xs:complexType>
                            <xs:complexContent>
                              <xs:extension base="corrected-curve-type" />
                            </xs:complexContent>
                        </xs:complexType>
                    </xs:element>
                </xs:sequence>
            </xs:complexType>
        </xs:element>
    </xs:all>
    <xs:attribute name="date" type="xs:dateTime" use="required" />
</xs:complexType>
<xs:complexType name="pv-device-description-type">
    <xs:choice>
        <xs:element name="pv-cell" type="pv-cell-type" />
        <xs:element name="pv-module" type="pv-module-type" />
        <xs:element name="pv-generator">
            <xs:complexType>
                <xs:sequence>
                    <xs:element name="pv-string" minOccurs="0">
                        <xs:complexType>
                            <xs:sequence>
                                <xs:element name="pv-module" ...
```

```
                                type="pv-module-type" minOccurs="0" />
                            </xs:sequence>
                            <xs:attribute name="number-of-modules" ...
                            type="xs:positiveInteger" />
                        </xs:complexType>
                    </xs:element>
                </xs:sequence>
                <xs:attribute name="number-of-strings" ...
                type="xs:positiveInteger" />
                <xs:attribute name="internal-idetification" ...
                  type="xs:string" />
            </xs:complexType>
        </xs:element>
    </xs:choice>
</xs:complexType>
<xs:complexType name="pv-module-type">
    <xs:all>
        <xs:element name="specification-sheet" ...
          type="xs:anyURI" minOccurs="0" />
        <xs:element name="serial-number" type="xs:string" minOccurs="0" />
        <xs:element name="internal-identification" ...
        type="xs:string" minOccurs="0" />
    </xs:all>
</xs:complexType>
<xs:complexType name="pv-cell-type">
    <xs:all>
        <xs:element name="specification-sheet" type="xs:anyURI" />
        <xs:element name="serial-number" type="xs:string" />
        <xs:element name="internal-identification" type="xs:string" />
    </xs:all>
</xs:complexType>
<xs:complexType name="environment-type">
    <xs:choice>
        <xs:element name="indoor-measurement">
            <xs:complexType>
                <xs:all>
                    <xs:element name="sun-simulator-description" ...
                    type="xs:string" />
                </xs:all>
            </xs:complexType>
        </xs:element>
        <xs:element name="outdoor-measurement">
            <xs:complexType>
                <xs:all>
                    <xs:element name="latitude" type="measurement-type" />
                    <xs:element name="longitude" type="measurement-type" />
                    <xs:element name="altitude" type="measurement-type" />
                </xs:all>
            </xs:complexType>
        </xs:element>
    </xs:choice>
</xs:complexType>
<xs:complexType name="measure-array-type">
    <xs:all>
        <xs:element name="value-array" minOccurs="1" maxOccurs="1">
            <xs:complexType>
                <xs:sequence>
                    <xs:element name="value" type="xs:double" ...
                       minOccurs="1" ...
                       maxOccurs="unbounded" />
                </xs:sequence>
            </xs:complexType>
```


```
        </xs:element>
        <xs:element name="uncertainty-array" minOccurs="0" maxOccurs="1">
            <xs:complexType>
                <xs:sequence>
                    <xs:element name="uncertainty" type="xs:double" ...
                    minOccurs="1" maxOccurs="unbounded" />
                </xs:sequence>
            </xs:complexType>
        </xs:element>
    </xs:all>
    <xs:attribute name="magnitude" type="xs:string" />
    <xs:attribute name="unit" type="xs:string" />
</xs:complexType>
<xs:complexType name="spectrum-point-type">
    <xs:all>
        <xs:element name="wavelenght" type="measurement-type" ...
          minOccurs="1" />
        <xs:element name="spectrum" type="measurement-type" ...
          minOccurs="1" />
    </xs:all>
</xs:complexType>
<xs:complexType name="administrative-information">
    <xs:all>
        <xs:element name="laboratory-name" type="xs:string" />
        <xs:element name="laboratory-address" type="xs:string" />
        <xs:element name="client-name" type="xs:string" />
        <xs:element name="client-address" type="xs:string" />
        <xs:element name="responsible-employee" type="xs:string" />
    </xs:all>
</xs:complexType>
<xs:complexType name="specimen-description">
    <xs:choice>
        <xs:element name="cell-description" type="cell-description" />
        <xs:element name="module-description" type="module-description" />
        <xs:element name="string-description" type="string-description" />
    </xs:choice>
    <xs:attribute name="date-of-receipt" />
</xs:complexType>
<xs:complexType name="cell-description">
    <xs:all>
        <xs:element name="manufacturer" type="xs:string" />
        <xs:element name="model" type="xs:string" />
        <xs:element name="technology-identification" type="xs:string" />
        <xs:element name="electrical-parameters" ...
        type="electrical-parameters-type" />
        <xs:element name="cell-dimensions" type="dimensions-type" />
    </xs:all>
</xs:complexType>
<xs:complexType name="module-description">
    <xs:all>
        <xs:element name="manufacturer" type="xs:string" />
        <xs:element name="model" type="xs:string" />
        <xs:element name="electrical-parameters" ...
        type="electrical-parameters-type" />
        <xs:element name="module-dimensions" type="dimensions-type" />
        <xs:element name="cell-description" type="cell-description" />
        <xs:element name="cells-in-series" type="xs:int" />
        <xs:element name="cells-in-parallel" type="xs:int" />
    </xs:all>
</xs:complexType>
<xs:complexType name="string-description">
    <xs:all>
```

```
            <xs:element name="modules-in-series" type="xs:int" />
            <xs:element name="modules-in-parallel" type="xs:int" />
            <xs:element name="module-description" type="module-description" />
            <xs:element name="electrical-parameters" ...
            type="electrical-parameters-type" />
        </xs:all>
    </xs:complexType>
    <xs:complexType name="measurement-system-type">
        <xs:all>
            <xs:element name="module-bias-method" type="xs:string" />
            <xs:element name="iv-sampling-method" type="xs:string" />
            <xs:element name="irradiance-sensor" type="xs:string" />
            <xs:element name="temperature-sensor" type="xs:string" />
        </xs:all>
    </xs:complexType>
</xs:schema>
```

Appendix B

Resumen de la tesis

B.1 Sistema de medida de curvas *I–V*

B.1.1 Introducción

La medida experimental de la curva *I–V* nos permite conocer con precisión los parámetros eléctricos de un dispositivo fotovoltaico. Esta medida proporciona información muy relevante para el diseño, instalación y mantenimiento de sistemas fotovoltaicos. A partir de la curva *I–V* de un módulo fotovoltaico podemos obtener información muy útil relativa a su calidad y rendimiento. Por esta razón se ha diseñado un sistema experimental para la caracterización en exteriores de módulos fotovoltaicos. En comparación con las medidas con simulador solar, las principales ventajas de las medidas en exteriores son que no se requiere ninguna fuente de luz artificial, no hay ninguna limitación en el tamaño de las muestras y la iluminación de las muestras es más homogénea [1].

Durán et al. [2] presentan una revisión de los diferentes métodos para medir la curva *I–V* de módulos fotovoltaicos. Estos pueden clasificarse en cinco categorías: basados en una resistencia variable, basados en una carga capacitiva, basados en una carga electrónica, basados en convertidores DC–DC y basados en una fuente de alimentación de cuatro cuadrantes, encuadrándose nuestro equipo en esta última variante. Las fuentes de alimentación de cuatro cuadrantes son capaces tanto entregar como de disipar energía, en otras palabras, pueden actuar bien como fuente o bien como carga. Con los módulos fotovoltaicos el principal interés está en la obtención la curva *I–V* en el primer cuadrante, pero la exploración de los puntos que están en el segundo y cuarto cuadrante podría ser una importante herramienta de diagnóstico además de permitir la obtención de puntos experimentales en torno a los ejes, lo que nos permitiría calcular los parámetros eléctricos con mayor

precisión (ver Figura 2.5). Hecktheuer et al. [3] describen un sistema controlado por computadora en el que se usa una fuente de alimentación de cuatro cuadrantes para hacer un barrido en voltaje de los módulos, mientras que dos multímetros digitales miden los pares I–V cada vez que les llega una orden de medida desde la computadora. Varios autores, De Blas et al. [4], Malik and Damit [5], Granek and Zdanowicz [6] y Fernández–Reche et al. [7], proponen otros sistemas similares basados también en una fuente de alimentación de cuatro cuadrantes.

B.1.2 Arquitectura del sistema

El principio básico general que se utiliza para medir la curva I–V de un módulo fotovoltaico se basa en la lectura de la corriente que circula por el módulo cuando la tensión se incrementa gradualmente entre el punto de cortocircuito y el punto de circuito abierto. En nuestro sistema, para hacer el barrido en tensión usamos una fuente de alimentación de cuatro cuadrantes Kepco BOP 100-100MG. Un ordenador conectado a la fuente mediante GPIB controla el barrido de forma automática. Para programar el barrido y controlar la fuente se usa el lenguaje de programación SCPI. El esquema utilizado para medir la curva I–V se muestra en la Figura 2.7.

Para hacer la medida se utiliza una configuración a cuatro hilos, evitando así errores derivados de la caída de tensión en los cables. La tensión del módulo se mide con un multímetro digital Agilent 34411A utilizando el rango de ±100 V. Por otra parte, la corriente del módulo se mide con la ayuda de un shunt en serie entre el módulo y la fuente. El shunt a usar se selecciona dependiendo de la corriente máxima que den los módulos a medir (para las medidas que aparecen en este trabajo se ha utilizado un shunt de 10 A de valor nominal y una salida de 100 mV). La caída de tensión a través del shunt se mide con otro multímetro digital idéntico al anterior, pero configurado para medir en el rango de ±100 mV. Ambos multímetros están conectados a través de GPIB y se han programado para hacer una medida cada vez que les llega un pulso a sus respectivas entradas de disparo externas. La sincronización se lleva a cabo mediante un generador de forma de onda Agilent 33220A, que crea una señal cuadrada que llega de forma simultánea a los dos multímetros, siendo la frecuencia de la señal generada la tasa de pares I–V que se registran cada segundo. Mientras se realiza el barrido, los multímetros almacenan en su memoria interna las medidas y cuando el proceso ha terminado la computadora recupera los datos almacenados.

En este sistema podemos realizar la medida de la curva I–V de un módulo de dos maneras diferentes: con una curva de una rampa o con una curva de dos rampas. En el primer caso todas las medidas aparecen equiespaciadas

a lo largo del eje de tensión. Sin embargo, en el segundo caso se realizan dos rampas, una primera rampa muy rápida entre la tensión inicial y una tensión intermedia (antes del codo de la curva I–V), y otra rampa lenta entre la tensión intermedia y el valor de tensión final. Esto implica que se van a capturar muchos más puntos en la parte de la curva I–V con más pendiente (en la parte plana de la curva no es necesario tener muchos puntos). Esto nos permite medir muchos puntos experimentales alrededor del punto de máxima potencia y del punto de circuito abierto, de modo que estos valores se podrán determinar con mayor precisión.

Al mismo tiempo en el que se mide la curva I–V se registran las variables meteorológicas. La temperatura del módulo se mide a través de un sensor Pt100 adherido a la parte trasera del mismo, mientras que la irradiancia incidente sobre la superficie del módulo se mide a través de un piranómetro Kipp & Zonen CMP21. Estas señales se registran al comienzo y al final de cada medida, y sólo si la diferencia entre ellas es inferior a un umbral fijado por el usuario, se almacena la curva. Estos y otros sensores (como anemómetro, veleta, pluviómetro, barómetro ...) están conectados a un sistema modular de adquisición de datos conectado a la computadora de control mediante interfaz Ethernet. El sistema integra una caja de relés que multiplexa hasta ocho módulos fotovoltaicos. El control de la caja de relés se realiza a través del sistema de adquisición de datos en el que se ha instalado un módulo específico con tal fin.

B.1.3 Método de sincronización

Tradicionalmente se usa una fuente de alimentación de cuatro cuadrantes para hacer un barrido en tensión del dispositivo fotovoltaico, mientras un par de multímetros registran los valores de tensión y corriente correspondientes a cada uno de los puntos de la curva I–V. Estos multímetros suelen sincronizarse por software, utilizando una instrucción GPIB que permite el disparo simultáneo de la medida de ambos multímetros. Una pequeña diferencia de tiempo en el disparo de ambos multímetros implica que las lecturas de tensión y de corriente no corresponden al mismo punto de trabajo del dispositivo, con lo que el punto medido no corresponde con ningún punto real de la curva I–V. Esta diferencia podría ser especialmente significativa en las inmediaciones de V_{OC} donde la pendiente de la curva es máxima.

Se han llevado a cabo dos pruebas para comparar el método de sincronización software mediante instrucciones GPIB con el método que se presenta en esta tesis, o sea, mediante una señal externa que dispara ambos multímetros. En ambas pruebas se ha generado una rampa en tensión desde -50 V hasta $+50$ V, con una duración de un segundo. En cada prueba se

han tomado un total de 100 medidas de la misma señal usando un par de multímetros (Agilent 34411A) conectados a los mismos terminales. En la primera prueba ambos multímetros se han sincronizado usando GPIB (software) mientras que en la segunda prueba los mismos multímetros se han sincronizado mediante una señal cuadrada que se bifurca y se conecta a la entrada de disparo externo de ambos multímetros. Si la medida se hace realmente de forma simultánea, ambos multímetros deberían leer el mismo valor de tensión. Una vez registradas las medidas en cada una de las pruebas se calcula la diferencia entre los valores registrados por cada uno de los multímetros correspondientes al mismo instante de tiempo. En la Figura 2.9 se pueden observar las diferencias correspondientes a la primera prueba (sincronización por GPIB). Los resultados muestran claramente que la diferencia entre los valores registrados por cada uno de los multímetros es significativamente mayor que la incertidumbre asociada a la medida de tensión. Esto significa que la medida no puede ser considerada realmente simultánea.

Los resultados que se obtienen usando el método de sincronización propuesto en este trabajo se presentan en la Figura 2.10. En este caso, las diferencias entre las medidas de ambos multímetros son mucho menores que las que se obtienen mediante el método anterior, y además son menores que la incertidumbre asociada a cada valor de tensión. Así que en este caso sí que es razonable considerar que las medidas se hacen de forma simultánea.

B.1.4 Análisis de incertidumbre

En esta sección se estima la incertidumbre asociada a cada una de las medidas de los puntos discretos que forman la curva *I–V* (la estimación de los parámetros eléctricos y sus incertidumbres se abordan en la siguiente sección). En esta sección se ha seguido la notación recomendada por ISO–GUM [8] y los procedimientos descritos por Whitfield and Osterwald [9]. Además, se ha tenido en cuenta la ficha de especificaciones del modelo de multímetro utilizado [10]. Siguiendo estas referencias ha sido posible determinar la incertidumbre expandida con un 95 % de nivel de confianza asociada a cada medida de tensión que se puede dar mediante la siguiente expresión:

$$\begin{aligned} U_V(\mathrm{V}) &= 2 \cdot \sqrt{\left(\frac{200}{2^{18}\sqrt{12}}\right)^2 + \left(\frac{e_V}{\sqrt{3}}\right)^2 + \left(\frac{e_V}{4 \cdot 2}\right)^2} \\ &= 2 \cdot \sqrt{7.1 \cdot 10^{-10} \cdot V^2 + 6.9 \cdot 10^{-8} \cdot |V| + 1.7 \cdot 10^{-6}} \end{aligned}$$

Esta incertidumbre depende del valor de tensión que se haya medido. Esto significa que cada punto de la curva *I–V* tendrá una incertidumbre diferente.

El peor caso ocurre cuando se mide el mayor valor de tensión posible con muestro sistema, o sea, 100 V. Así que la incertidumbre en tensión asociada al peor caso sería $U_{V,worst} = 0,008$ V.

De igual forma, la incertidumbre expandida U_I con un nivel de confianza del 95 % para la medida de corriente sería:

$$\begin{aligned} U_I(\mathrm{A}) &= \frac{10\ \mathrm{A}}{100\ \mathrm{mV}} \cdot U_I^V \\ &= 0.1 \cdot 2 \cdot \sqrt{3.3 \cdot 10^{-7} \cdot V_{shunt}^2 + 7.3 \cdot 10^{-7} \cdot |V_{shunt}| + 1.3 \cdot 10^{-4}} \\ &= 2 \cdot \sqrt{3.3 \cdot 10^{-7} \cdot I^2 + 7.3 \cdot 10^{-8} \cdot |I| + 1.3 \cdot 10^{-6}} \end{aligned}$$

Ahora, el peor caso ocurre cuando la corriente igual a la máxima corriente que podemos medir con el shunt seleccionado (10 A). Así que la incertidumbre expandida en el peor caso para la medida de corriente sería $U_{I,worst} = 0,01$ A.

Según ISO–GUM [8], y teniendo en cuanta que $P = V \times I$, la incertidumbre expandida con un nivel de confianza del 95 % para cada valor te potencia asociado a cada uno de los puntos se calcula como:

$$\begin{aligned} U_P(\mathrm{W}) &= 2 \cdot \sqrt{\left(\frac{\partial P}{\partial V}\right)^2 \cdot \left(\frac{U_V}{2}\right)^2 + \left(\frac{\partial P}{\partial I}\right)^2 \cdot \left(\frac{U_I}{2}\right)^2} \\ &= 2 \cdot \sqrt{I^2 \cdot \left(\frac{U_V}{2}\right)^2 + V^2 \cdot \left(\frac{U_I}{2}\right)^2} \\ &= 2 \cdot \sqrt{\begin{array}{l} 6.9 \cdot 10^{-8} \cdot |V| \cdot I^2 + 1.7 \cdot 10^{-6} \cdot I^2 + 7.3 \cdot 10^{-8} \cdot |I| \cdot V^2 + \\ +1.3 \cdot 10^{-6} \cdot V^2 + 3.4 \cdot 10^{-7} \cdot V^2 \cdot I^2 \end{array}} \end{aligned}$$

Finalmente, el peor caso en la medida de potencia será (usando el shunt seleccionado) cuando la tensión vale 100 V y la corriente 10 A, o sea, que la incertidumbre expandida asociada a la medida de potencia en el peor caso con un nivel de confianza del 95 % será $U_{P,worst} = 1,2$ W.

Cada vez que se mide una curva *I–V*, se miden la irradiancia y la temperatura del módulo. Así que también es necesario estimar las incertidumbres asociadas a estas medidas. Siguiendo el trabajo de Kratzenberg et al. [11], y las especificaciones [12] y [13] se llega a la siguiente expresión que da una estimación de la incertidumbre expandida con un nivel de confianza del 95 % asociada a la medida de irradiancia:

$$U_G(\mathrm{W/m^2}) = 2 \cdot \sqrt{\left(\frac{e_{DR}^2}{3} + 6.5 \cdot 10^{-5}\right) \cdot G^2 + 4.4 \cdot 10^{-3} \cdot G + 1.7 \cdot 10^2}$$

donde U_{DR} es la incertidumbre asociada al error direccional del piranómetro, cuyo valor da el fabricante en función del ángulo de incidencia (AOI). En incidencia normal y con una irradiancia igual a 1000 W/m^2, la incertidumbre expandida con un nivel de confianza del 95 % tiene un valor de 30 W/m^2 (3 %).

La incertidumbre asociada a la medida de temperatura de módulo es estimada teniendo en cuenta las especificaciones del módulo de medida de sensores RTD del FieldPoint [14] y la norma IEC 60751 [15] (especificaciones correspondientes a un sensor Pt100 de clase B). Así que la incertidumbre expandida asociada a la medida de temperatura de módulo con un nivel de confianza del 95 %,

$$U_T(\mathrm{W/m^2}) = 2 \cdot \sqrt{\left(\frac{T_{max} - T_{min}}{2^n \cdot \sqrt{12}}\right)^2 + \left(\frac{e_{T_{FP}}}{\sqrt{3}}\right)^2 + \left(\frac{U_T^C}{2}\right)^2 + \left(\frac{e_{Pt_{100}}}{\sqrt{3}}\right)^2 + \left(\frac{e_{TCO}}{\sqrt{3}}\right)^2}$$

$$= 2 \cdot \sqrt{\left(\frac{850 - (-200)}{2^{16} \cdot \sqrt{12}}\right)^2 + \left(\frac{0.25}{\sqrt{3}}\right)^2 + \left(\frac{0.25}{4 \cdot 2}\right)^2 + \left(\frac{e_{Pt_{100}}}{\sqrt{3}}\right)^2 + \left(\frac{1}{\sqrt{3}}\right)^2}$$

$$= 2 \cdot \sqrt{8.3 \cdot 10^{-6} \cdot T_M^2 + 1.1 \cdot 10^{-3} \cdot |T_M| + 3.9 \cdot 10^{-1}}$$

Así que una lectura de temperatura de módulo en torno a los 50 °C tendrá una incertidumbre expandida de $1,4$ °C.

B.1.5 Estimación de los parámetros eléctricos

Además de los puntos de la curva *I–V*, es necesario estimar los principales parámetros eléctricos del modulo en el momento de la medida: la corriente de cortocircuito (I_{SC}), la tensión de circuito abierto (V_{OC}), el valor de máxima potencia (P_{M}), el valor de corriente en el punto de máxima potencia (I_{M}) y el valor de tensión en el punto de máxima potencia (V_{M}). Estos valores pueden ser luego usados para calcular otros parámetros derivados como por ejemplo el fill factor (FF). Normalmente el valor de la corriente de cortocircuito (I_{SC}) se suele calcular mediante interpolación lineal de los dos puntos más cercanos

al eje de tensión cero (se coge un punto anterior y otro posterior al eje). De acuerdo con Emery [16], una regresión lineal usando más de dos puntos reduciría la incertidumbre, pero esta opción es rechazada porque al hay cierto riesgo de tomar puntos de zonas afectadas por los diodos de *bypass*. De igual forma, la tensión de circuito abierto (V_{OC}) se obtiene mediante la interpolación lineal de los dos puntos más cercanos al eje de corriente cero. Aunque la curva I–V es claramente no lineal en las proximidades de V_{OC}, la interpolación lineal es una buena aproximación siempre que la densidad de puntos alrededor del eje sea suficiente, y esto es posible de configurar mediante el programa de control. Sean ($V-$, $I-$) y ($V+$, $I+$) los puntos más cercanos al eje de tensión cero. Entonces, la incertidumbre expandida asociada a la medida de I_{SC} con un nivel de confianza del 95 % sería:

$$U_{I_{\mathrm{SC}}}(\mathrm{A}) = 2 \cdot \sqrt{\begin{array}{l}\left(\dfrac{\partial I_{\mathrm{SC}}}{\partial I^-}\right)^2 \cdot \left(\dfrac{U_I^-}{2}\right)^2 + \left(\dfrac{\partial I_{\mathrm{SC}}}{\partial I^+}\right)^2 \cdot \left(\dfrac{U_I^+}{2}\right)^2 + \\ + \left(\dfrac{\partial I_{\mathrm{SC}}}{\partial V^-}\right)^2 \cdot \left(\dfrac{U_V^-}{2}\right)^2 + \left(\dfrac{\partial I_{\mathrm{SC}}}{\partial V^+}\right)^2 \cdot \left(\dfrac{U_V^+}{2}\right)^2\end{array}}$$

$$= 2 \cdot \sqrt{\begin{array}{l}\left(\dfrac{V^+}{V^+ - V^-}\right)^2 \cdot \left(\dfrac{U_I^-}{2}\right)^2 + \left(\dfrac{V^-}{V^+ - V^-}\right)^2 \cdot \left(\dfrac{U_I^+}{2}\right)^2 + \\ + \left(\dfrac{(I^+ - I^-)V^+}{(V^+ - V^-)^2}\right)^2 \cdot \left(\dfrac{U_V^-}{2}\right)^2 + \left(\dfrac{(I^+ - I^-)V^-}{(V^+ - V^-)^2}\right)^2 \cdot \left(\dfrac{U_V^+}{2}\right)^2\end{array}}$$

La estimación de V_{OC} y su incertidumbre expandida se hace de forma análoga. El valor de potencia máxima (P_{M}) se suele tomar como el máximo de los valores de potencia ($\overline{P}_{\mathrm{M}}$) de la colección de puntos discretos que forman la curva I–V medida (V_{M} y I_{M} también se toman como los valores de tensión $\overline{V}_{\mathrm{M}}$ y corriente $\overline{I}_{\mathrm{M}}$ asociados a dicho punto discreto con mayor potencia). Sin embargo, ya que este valor se toma de una muestra discreta, es una subestimación del verdadero valor de máxima potencia. Emery [16] sugiere el uso de métodos más precisos, como por ejemplo un ajuste de los puntos de la curva P–V (curva tensión–potencia) con un polinomio de cuarto grado o superior. En nuestro sistema, tenemos la opción de configurar la aplicación para capturar los puntos del codo con una densidad suficiente, de forma que la diferencia en potencia entre dos puntos consecutivos esté en el mismo orden de magnitud que la incertidumbre asociada a la medida. En consecuencia, nosotros proponemos dar como punto de máxima potencia el punto discreto medido que maximiza el producto $I \times V$. El fill factor se define como,

$$\mathrm{FF}\ (\%) = \frac{P_{\mathrm{M}}}{I_{\mathrm{SC}} \cdot V_{\mathrm{OC}}} \cdot 100$$

En consecuencia, la incertidumbre expandida asociada al valor de fill factor de la curva I–V se puede estimar usando la siguiente expresión,

$$\begin{aligned} \mathrm{U_{FF}} &= 2 \cdot \sqrt{\left(\frac{\partial \mathrm{FF}}{\partial P_{\mathrm{M}}}\right)^2 \cdot \left(\frac{U_{P_{\mathrm{M}}}}{2}\right)^2 + \left(\frac{\partial \mathrm{FF}}{\partial I_{\mathrm{SC}}}\right)^2 \cdot \left(\frac{U_{I_{\mathrm{SC}}}}{2}\right)^2 + \left(\frac{\partial \mathrm{FF}}{\partial V_{\mathrm{OC}}}\right)^2 \cdot \left(\frac{U_{V_{\mathrm{OC}}}}{2}\right)^2} \\ &= 2 \cdot \frac{100}{I_{\mathrm{SC}} \cdot V_{\mathrm{OC}}} \cdot \sqrt{\left(\frac{U_{P_{\mathrm{M}}}}{2}\right)^2 + \left(\frac{P_{\mathrm{M}}}{I_{\mathrm{SC}}}\right)^2 \cdot \left(\frac{U_{I_{\mathrm{SC}}}}{2}\right)^2 + \left(\frac{P_{\mathrm{M}}}{V_{\mathrm{OC}}}\right)^2 \cdot \left(\frac{U_{V_{\mathrm{OC}}}}{2}\right)^2} \end{aligned}$$

B.1.6 Resultados experimentales

En la Figura 2.12 se muestran dos curvas I–V de un modulo de prueba obtenidas usando el sistema experimental propuesto en esta tesis.

En la Tabla 2.8 se da la estimación de los principales parámetros eléctricos de las curvas de la Figura 2.12 y las incertidumbres asociadas a cada uno de los valores. En la tabla también se muestran los valores de irradiancia y de temperatura como también las incertidumbres de dichos valores.

Varias medidas en exteriores se han llevado a cabo de forma consecutiva para ilustrar la precisión del sistema experimental propuesto. Todas las medidas se han tomado bajo la misma irradiancia y temperatura de módulo. Los resultados de estas medidas pueden verse en la Figura 2.13. En la Tabla 2.9 se proporcionan la media, el máximo, el mínimo y la varianza de cada uno de los parámetros.

B.2 Formato para el intercambio de curvas *I–V*

En esta tesis se define un formato de fichero para almacenar e intercambiar medidas de las curvas I–V de dispositivos fotovoltaicos, tales como células, módulos y strings. El objetivo es proporcionar una metodología unificada y aceptada que facilite el intercambio de datos entre diferentes laboratorios de investigación y empresas del sector y evitar que cada uno use su propio formato, ahorrando tiempo a la hora de comparar medidas, permitiendo así el desarrollo de programas estandarizados para procesar esta información con el mínimo esfuerzo. Esta propuesta está basada en el lenguaje XML que ya ha sido utilizado en otros campos con una finalidad parecida [17], [18], [19].

Existe un intento previo de desarrollar un formato de datos basado en XML orientado a almacenar y controlar la información de las plantas fotovoltaicas. En Kolodenny et al. [20], un esquema de datos llamado PVML se propone para modelar sistemas fotovoltaicos de cualquier tipo y tamaño con el fin de detectar fallos y disminuciones del rendimiento. En un segundo trabajo [21], se describen las entidades del formato. La estructura propuesta en esta tesis está muy relacionada con estos trabajos, pero se centra fundamentalmente en el almacenamiento y la translación de curvas *I–V* en lugar de en una instalación fotovoltaica completa. Además, en esta tesis, las incertidumbres de los valores medidos y calculados se tienen en cuenta.

XML (siglas de eXtensible Markup Language) fue desarrollado para superar las limitaciones de HTML y está basado en el concepto de marca. Estas marcas integradas en el mismo documento que almacena la información sirven para su interpretación y tratamiento automático. El usuario define sus propias marcas según sus necesidades, sin tener que ampliar el lenguaje. XML se utiliza ampliamente como un formato para el intercambio de datos entre aplicaciones y es fácil de leer por los programas y aplicaciones existiendo librerías con tal fin.

En el pasado, los DTD (*Document Type Definition*) proporcionaban un mecanismo para describir el contenido y la estructura de un archivo XML. Sin embargo, actualmente se utiliza el formato XSD (*XML Schema*) que supera los problemas de los DTDs. Esta tesis propone un XSD para definir la estructura de archivos XML válidos para almacenar curvas *I–V*. La idea consiste en ofrecer este XSD a la comunidad fotovoltaica con el objetivo de que sea utilizado para intercambiar medidas o como formato de entrada de las aplicaciones de medida y de tratamiento de curvas *I–V* que se desarrollen.

Teniendo en cuenta todos los requisitos de información que se detallan en la sección 3.3, se enumeran una por una cada una de las definiciones de las entidades necesarias y que se incluyen en el fichero XSD que define el formato. En primer lugar, y de acuerdo con ISO–GUM [8], cada medida debe darse con su incertidumbre asociada, dando también el factor de cobertura y el nivel de confianza. Por lo tanto, se define un tipo complejo XML llamado *measurement–type*. Cada punto de una curva *I–V* se modela usando entidades del tipo *iv-par-type*, y la curva *I–V* completa se modela como una entidad llamada *iv-array-type*, que no es más que una lista ordenada de entidades del tipo anterior. Con el tipo *measurement-list* se pretende modelar una lista de valores para almacenar los parámetros meteorológicos de cada una de las campañas que se definen. Por otra parte, también es necesario definir una entidad para almacenar los puntos del espectro solar, como *spectrum-point-type* y otra entidad para almacenar el espectro completo *spectrum-type* (también como una lista ordenada de puntos). Además, es necesario un tipo

de datos que nos permita almacenar los principales parámetros eléctricos que podemos calcular a partir de los puntos de la curvas I–V: I_{SC}, V_{OC}, P_M, I_M, V_M, la eficiencia de la muestra, el factor de idealidad y las resistencias en serie y en paralelo. Por último, en las entidades del tipo *iv-curve-type* se pretende almacenar una curva I–V y todas las traslaciones que se hagan sobre dicha curva medida. Además de las entidades anteriores, pensadas para almacenar medidas, existen otras entidades cuya finalidad es simplemente descriptiva, ya sea bien para almacenar las especificaciones del módulo o célula fotovoltaica, o bien para almacenar información referente al laboratorio que efectúa las medidas.

B.3 Estimación de los parámetros solares

En esta sección vamos a analizar los distintos algoritmos utilizados para calcular una serie de parámetros relacionados con la posición del Sol y con la radiación que llega del mismo a la superficie del módulo fotovoltaico. Algunos de estos parámetros se usarán luego como entradas de los modelos que se proponen en esta tesis. En concreto, se calculan los ángulos solares (altura, azimut y ángulo de incidencia), el factor de masa de aire (airmass factor) y el índice de transparencia. Además, se incluye el procedimiento para determinar el APE (energía promedio del fotón) a partir de la medida del espectro solar.

El cálculo de estos parámetros se basa en la determinación de la posición del Sol en la bóveda celeste. En la literatura previa se han propuesto fórmulas que permiten estimar dicha posición, como las propuestas por Spencer [22], Michalsky [23] y Blanco–Muriel et al. [24]. Sin embargo, existen algoritmos más precisos basados en tablas astronómicas como el propuesto por Meeus [25], que recientemente ha sido adaptado para aplicaciones solares por Reda y Andreas [26]. Este último trabajo, que es el que se sigue en esta tesis, incluye el cálculo del ángulo de incidencia para una superficie inclinada en cualquier dirección utilizando las fórmulas dadas por Iqbal [27].

El algoritmo utilizado requiere como entrada la fecha y hora determinada en *milenios julianos* utilizando el sistema de tiempo conocido como *terrestrial time* `TT`, que es la forma de contar el tiempo que se usa en astronomía. Así que primero se describe cómo convertir la hora `UTC` a este otro sistema.

Luego se introducen los distintos cálculos astronómicos para determinar la posición del Sol en la esfera celeste. Primero se calcula la posición de la Tierra con respecto al Sol utilizando una serie de desarrollos de Fourier y se termina determinando la elevación solar (o su complementario, el ángulo cenital), el ángulo azimutal y el ángulo de incidencia. En estos cálculos se

tienen en cuenta una serie de correcciones por diversos factores: la influencia de la Luna sobre la rotación de la Tierra, correcciones por aberración y por parallax, por la refracción de los rayos solares en la atmósfera...

A continuación introducimos el concepto de radiación solar extraterrestre, que es la que alcanzaría la superficie de la Tierra si no hubiera atmósfera y los rayos solares no sufrieran ningún tipo de desviación. Esta viene dada por la constante solar y la distancia al Sol en un instante determinado. En esta tesis se toma como constante solar el valor de 1366.1 W/m^2 dado por Gueymard [28]. Este valor es la potencia solar por unidad de superficie que se recibe cuando la distancia del Sol a la Tierra igual a 1 AU, o sea, su valor medio.

Otro de los conceptos que se introducen es el factor de la masa de aire (airmass) que es la longitud del camino óptico de la luz cuando el Sol está a una altura determinada dividido por la longitud del camino óptico cuando el Sol está en el cénit. Kasten y Young [29] presentan una fórmula que aproxima este valor. Sin embargo, este valor previo puede ser corregido por presión usando la expresión propuesta por Bird y Riordan [30].

Liu y Jordan [31] definen el coeficiente de transmisión como el cociente entre la irradiancia global medida en una superficie horizontal y la radiación solar extraterrestre. Woyte et al. [32] renombran este concepto como índice de transparencia y amplían su definición a cualquier ángulo de incidencia sobre una superficie arbitrariamente orientada. Según Pérez et al. [33] este valor puede normalizarse utilizando el valor de masa de aire previamente presentado.

Finalmente, introducimos el concepto conocido como energía promedio del fotón (APE), como un intento de caracterizar la forma del espectro con un único valor numérico. El APE es un valor instantáneo que se define como el cociente entre la irradiancia total del espectro y la densidad del flujo de fotones. Minemoto et al. [34] dan una expresión para calcular dicho valor a partir de la integral de la distribución espectral entre dos límites de integración determinados. En lugar de evaluar el valor de APE a lo largo de un rango único, se propone su cálculo a lo largo de varios intervalos contiguos de integración, de forma que así obtendremos varios valores de APE que pueden utilizarse como entrada de los modelos basados en redes neuronales que se proponen en esta tesis.

B.4 Redes neuronales para simular módulos fotovoltaicos

B.4.1 Introducción

En esta tesis se propone una metodología basada en redes neuronales como alternativa a los métodos algebraicos y numéricos para estimar la curva característica de módulos fotovoltaicos a diferentes condiciones de irradiancia y temperatura. Es posible encontrar en la literatura métodos algebraicos para trasladar punto a punto una curva I–V a otras condiciones de irradiancia y temperatura distintas de aquellas a las que el módulo ha sido medido. Algunas de ellas aparecen en la norma IEC 60891 [35]. Sin embargo, estos métodos no tienen en cuenta la distribución de la radiación incidente. Si se conoce dicha distribución espectral y la respuesta espectral del módulo es posible realizar una corrección para obtener la característica del módulo bajo otra distribución espectral mediante el procedimiento descrito por la norma IEC 60904–7 [36].

Además de los métodos algebraicos, existen métodos más complejos basados en la física de los semiconductores, en los que los dispositivos fotovoltaicos se modelan mediante sus circuitos equivalentes: la relación entre corriente y tensión viene dada por una expresión que depende de varios parámetros, algunos de los cuales dependen de la irradiancia y la temperatura (los parámetros intrínsecos del dispositivo fotovoltaico se determinan mediante algún procedimiento numérico). Domínguez et al. [37] describen un modelo de este tipo, que además de la irradiancia y la temperatura, tiene en cuenta la distribución espectral de la luz.

Por último, existen algunos trabajos en la literatura en los que se aborda el problema mediante el uso de redes de neuronas artificiales, como por ejemplo, Patra [38], Karatepe et al. [39], Di Piazza et al. [40], Hontoria et al. [41], Almonacid et al. [42], Almonacid et al. [43], Almonacid et al. [44] y Zárate et al. [45]. Las redes neuronales se utilizan para reconstruir la curva I–V de un módulo fotovoltaico a partir de los valores de irradiancia y temperatura. Sin embargo, en estos casos la distribución espectral de la radiación incidente no se tiene en cuenta. Una de las contribuciones más importantes de esta tesis es la incorporación como entrada a la red de información relativa a la distribución espectral de la radiación incidente en el módulo. También se incorporan ciertos parámetros calculados a partir de la posición del Sol en la bóveda celeste, como el ángulo de incidencia (AOI) y el índice de transparencia normalizado (K_T').

La principal ventaja de las redes neuronales proviene de su capacidad de

generalización, siendo capaces de reproducir la curva I–V con gran fidelidad incluso para condiciones de irradiancia y temperatura de célula no contempladas durante la fase de entrenamiento de la red.

Además, en lugar de hacer una selección aleatoria de los patrones de entrenamiento, se realiza una selección basada en una clasificación mediante un mapa auto–organizado de Kohonen. Gracias a este mecanismo de selección se consigue una mejora sustancial del rendimiento en comparación con una red neuronal entrenada sin información espectral.

Las medidas para entrenar la red neuronal se han realizado en la terraza del laboratorio de fotovoltaica de la Universidad de Málaga. La campaña de medidas comenzó el 1 de febrero de 2011 y finalizó el 22 de mayo de 2011, tomándose medidas cada 5 minutos. El tiempo de medida de la curva I–V se fijó en 1 segundo. La temperatura del módulo se toma usando un sensor RTD Pt100 adherido a la parte posterior del módulo y la irradiancia incidente en la superficie del módulo se mide mediante un piranómetro en el mismo plano. Estas señales se miden antes y después de tomar una curva I–V. Por último, un espectrorradiómetro EKO MS–710 (con un rango espectral desde 350 nm a 1050 nm) se ha instalado en el mismo plano del módulo.

B.4.2 Representación de las curvas tensión–corriente

Mientras que el aprendizaje de un valor escalar, como por ejemplo I_{SC} o V_{OC} es inmediato, el aprendizaje de un conjunto de puntos, como la curva I–V, es más complicado. En esta tesis se resuelve el problema de la misma forma en la que lo hace Zárate et al. [45]. Se añade una neurona ficticia a la capa de entrada de la red para representar la componente en tensión de cada punto de la curva I–V, de forma que en la capa de salida sólo hay una neurona que representa la componente en corriente de cada punto de la curva. Así que por cada medida original se van a generar tantos patrones de entrenamiento como puntos tenga la curva I–V. Formalmente, la función Ψ se transforma en otra función Γ más fácil de representar:

$$\Psi : \mathcal{R}^m \rightarrow \mathcal{R}^{Px2} \qquad \Psi(G, T, \dots) = \{(V_i, I_i)\}_{i=1}^{P}$$

$$\Gamma : \mathcal{R}^{m+1} \rightarrow \mathcal{R} \qquad \Gamma(G, T, \dots, V) = I$$

B.4.3 Ángulo de incidencia e índice de transparencia

En primer lugar vamos a describir y detallar los resultados obtenidos cuando incorporamos como entradas a la red el ángulo de incidencia y el índice de transparencia.

Tenemos que distinguir dos conjuntos de entrenamiento distintos. Por un lado tenemos 5822 medidas con únicamente irradiancia y temperatura de módulo (conjunto A). Por otra parte debemos considerar 5822 medidas con irradiancia, temperatura de módulo, ángulo de incidencia e índice de transparencia (conjunto B). En primer lugar, seleccionamos aleatoriamente 100 de estas medidas para entrenar la red, de forma que las 5722 medidas restantes quedan para hacer el correspondiente test para medir la capacidad de generalización de la red. Esto en realidad hay que hacerlo con los dos conjuntos iniciales de 5822 medidas.

El siguiente paso consiste en obtener de cada medida tantos patrones de entrenamiento como puntos tenga la curva I–V asociada a dicha medida. Así que cada patrón de entrada tendrá una medida de irradiancia, otra de temperatura de módulo, el valor del ángulo de incidencia, el valor del índice de transparencia, y finalmente el valor de la componente de tensión de cada punto de la curva I–V. Este proceso debe hacerse tanto para el conjunto A como para el conjunto B. Así que tenemos 2 conjuntos de entrenamiento y dos conjuntos de test.

No hay ninguna regla para determinar de forma previa el número óptimo de neuronas en la capa oculta. Así que tenemos que experimentar y realizar varios entrenamientos con cada alternativa. Finalmente hay que determinar el error cuadrático medio de cada posible variante y adoptar el número de neuronas ocultas correspondiente a la red que tenga menor error (ver Figura 5.1).

Sea $\mathrm{MLP_{GT}}$ la red entrenada con sólo irradiancia y temperatura con la que se obtienen mejores resultados y $\mathrm{MLP_{ALL}}$ la red entrenada con todos los parámetros (irradiancia, temperatura, ángulo de incidencia e índice de transparencia) con la que se obtienen mejores resultados. Se comparan los resultados individuales de cada red neuronal sobre el conjunto de test, o sea, los 5722 patrones que no han sido usados para entrenar la red.

La red neuronal $\mathrm{MLP_{ALL}}$ obtiene resultados más próximos a la curva I–V medida que la red $\mathrm{MLP_{GT}}$ en un total de 2889 ejemplos (50,5 %), mientras que en los 2833 ejemplos restantes (49,5 %), la red $\mathrm{MLP_{GT}}$ es mejor. Aunque el error cuadrático medio MSE es mejor en el caso del la red entrenada usando AOI y K_T', si estudiamos el error curva a curva, los resultados no implican ninguna mejora sobre la red que no utiliza esta información adicional. Sin embargo, si únicamente tenemos en cuenta medidas por debajo de 400 $\mathrm{W/m^2}$, entonces el porcentaje de ejemplos en los que $\mathrm{MLP_{ALL}}$ gana a $\mathrm{MLP_{GT}}$ se eleva al 66.3 % de los casos.

En las figuras 5.2, 5.3, 5.4 y 5.5 pueden verse ejemplos en los que se muestran las curvas medidas y las aproximaciones dadas por cada red neuronal en cada uno de los casos.

El ángulo de incidencia tiene mucho peso cuando la fracción de radiación directa es considerable, pero sin embargo no tiene apenas importancia cuando la mayor parte de la radiación es difusa. Por ello, es posible que se obtengan mejores resultados si en lugar de considerar todas las medidas de la base de datos, tenemos en cuenta únicamente medidas correspondientes a días con el cielo totalmente despejado. Tras una selección de este tipo de días, los conjuntos a considerar son: A' (3156 medidas de curva I–V con sólo irradiancia y temperatura de módulo) y B' (3156 medidas de curva I–V con irradiancia, temperatura de módulo, ángulo de incidencia e índice de transparencia).

De nuevo, seleccionamos aleatoriamente las 100 medidas que usaremos para el entrenamiento de forma que quedan 3056 medidas para calcular el error de generalización de las redes entrenadas. Usando sólo medidas de días despejados la red con información extra $\mathrm{MLP}'_{\mathrm{ALL}}$ arroja mejores resultados que la red $\mathrm{MLP}'_{\mathrm{GT}}$ en un total de un 64,5 % de los casos. Si consideramos únicamente medidas con bajo valor de irradiancia (< 500 W/m^2) el porcentaje aumenta hasta el 76,2 % de los casos.

B.4.4 Incorporación de la distribución espectral

Para representar la distribución espectral de la radiación incidente necesitamos una representación adecuada, ya que no estamos hablando de simples valores escalares que se puedan incorporar como entrada de la red neuronal sin más. En teoría, el espectro es una función que asigna a cada valor de longitud de onda (nm) un valor de irradiancia espectral (Wm^{-2}/nm). Cuando utilizamos un espectrorradiómetro para medir el espectro, este nos devuelve una tabla con valores de irradiancia a distintos valores de longitud de onda prefijados de antemano. Cada espectrorradiómetro mide estos valores a distintos valores de longitud de onda, de forma que la tabla que devuelve cada modelo no es comparable directamente con la tabla que devuelve otro modelo. Esto plantea una serie de problemas, ya que la misma distribución espectral tiene distintas representaciones dependiendo del modelo de espectrorradiómetro utilizado. Además, la cantidad de información que devuelve el espectrorradiómetro es enorme, de forma que su procesamiento directo afectaría negativamente al tiempo de entrenamiento de la red.

Una posible solución sería el uso del concepto llamado *energía promedio del fotón*(APE), un intento de caracterizar la forma del espectro usando un único valor. El APE se define como el cociente de la irradiancia total sobre todo el espectro y la densidad del flujo de fotones. Sin embargo, ya que los espectrorradiómetros no cubren todo el rango espectral de la radiación solar, esta definición normalmente se refiere a un intervalo finito de integración [46]:

$$APE_{\lambda_a}^{\lambda_b} = \frac{\int_{\lambda_a}^{\lambda_b} G_\lambda(\lambda) d\lambda}{\int_{\lambda_a}^{\lambda_b} \Phi_\lambda(\lambda) d\lambda}$$

Existen estudios estadísticos [34] que apoyan la idea de que el valor de APE caracteriza de forma única la forma del espectro solar. Sin embargo, en lugar de evaluar el APE en todo un intervalo, es posible su evaluación en varios pequeños intervalos contiguos. En esta tesis se trabaja con los valores de APE correspondientes a los 7 intervalos de 100 nm que hay entre los 350 nm y los 1050 nm:

$$APE_{350nm}^{450nm},\ APE_{450nm}^{550nm}, , \ldots, APE_{950nm}^{1050nm}$$

La Figura 5.6 muestra tres medidas típicas de espectro mientras que en la Figura 5.7 se muestra el espectro AM1.5 tal y como se define en la norma IEC 60904–3 [47]. Para cada espectro anterior la Tabla 5.7 muestra los valores de fecha, hora, irradiancia y los valores de APE en distintos intervalos.

Durante la campaña de medidas se han almacenado miles de curvas *I–V* en la base de datos. De todas ellas, solamente aquellas con un valor de irradiancia por encima de 200 W/m^2 se han tenido en cuenta. Además, se han descartado todas aquellas curvas *I–V* en las que la irradiancia antes y después de medir la curva difiere en más de un 1 %.

En lugar de hacer una selección aleatoria, es posible hacer una clasificación previa de las medidas de espectro en 100 clases, para entonces seleccionar aquel elemento de cada clase más parecido al prototipo de cada clase. La clasificación puede llevarse a cabo utilizando un mapa auto–organizado de Kohonen, un tipo especial de red neuronal con aprendizaje no supervisado, que es capaz de encontrar por sí misma correlaciones y patrones de regularidad en los ejemplos de entrada [48]. La idea de utilizar una red de Kohonen en la etapa de preparación del perceptrón multicapa no es nueva, ver como ejemplo Boznar y Mlakar [49]. En nuestro caso queremos clasificar las medidas teniendo en cuenta el valor de APE en los 7 intervalos de 100 nm que hay entre 350 nm y 1050 nm. La capa de salida del la red de Kohonen se dispone como una matriz de 10 filas y 10 columnas. La Tabla 5.8 muestra el número de patrones de entrada que se clasifican en cada una de las clases.

Por un lado, como queremos estudiar la mejora del rendimiento al incorporar información espectral, tendremos que tener en cuenta dos conjuntos de medidas distintas: GT (5822 medidas de curva *I–V* con únicamente irradiancia y temperatura de módulo) y SP (5822 medidas de curva *I–V* con irradiancia, temperatura de módulo y espectro). Por otra parte, mediante la red de Kohonen cada conjunto anterior se divide en dos subconjuntos: el

conjunto de entrenamiento (100 medidas para entrenar la red) y el *conjunto de test* (5722 medidas para calcular el error de generalización). Sin embargo, para ilustrar las ventajas de usar la selección mediante la red de Kohonen frente a una simple selección aleatoria, GT y SP también han sido divididos en dos grupos de 100 y 5722 medidas usando selección aleatoria. La Tabla 5.9 resume los distintos conjuntos que se han generado.

Para cada combinación de conjunto de entrenamiento (GT_Ra, GT_Ka, SP_Ra or SP_Ka) y distinto número de neuronas en la capa oculta ($h = 2, \ldots, 8$) hemos calculado el máximo, mínimo y el valor medio del MSE correspondiente (ver Tabla 5.10) . El valor medio para cada posible combinación se muestra en la Figura 5.11.

Según los resultados, únicamente cuando se hace una selección previa de los patrones de entrenamiento utilizando el mapa auto–organizado de Kohonen, los resultados de la red neuronal que incorpora información espectral son mejores que los que arroja la red neuronal sin información espectral.

Sea MLP_{GT} la mejor de todas las redes entrenadas sin información espectral y sea MLP_{SP} la mejor de todas las redes entrenadas con información espectral. Resulta que en un 59,8 % de los casos los resultados de MLP_{SP} son mejores que los de MLP_{GT}. Este porcentaje se eleva hasta el 89 % de los casos cuando únicamente tenemos en cuenta medidas con una irradiancia inferior a 500 W/m^2.

Las diferencias espectrales entre distintos días cuando la irradiancia es alta y el cielo está despejado son muy pequeñas (hay poca diferencia entre el cielo de dos días despejados). Sin embargo, en dos días nublados distintos sí que puede haber diferencias significativas del espectro, ya que existen distintos tipos de nubes, a distintas altitudes, con distintos patrones ...

En las Figuras 5.12, 5.13, 5.14, 5.15 y 5.16 pueden verse algunos ejemplos en los que se muestran curvas medidas junto con las aproximaciones dadas tanto por MLP_{GT} como por MLP_{SP}.

Bibliografía

[1] W. Durisch, J. Urban, and G. Smestad. Characterisation of solar cells and modules under actual operating conditions. *Renewable Energy*, 8 (1–4):359–366, 1996. doi: 10.1016/0960-1481(96)88878-1.

[2] E. Durán, M. Piliougine, M. Sidrach–de–Cardona, J. Galán, and J.M. Andújar. Different methods to obtain the I–V curve of PV modules: A review. In *33rd IEEE Photovoltaic Specialists Conference*, pages 1–6, San Diego (CA, USA), 2008. doi: 10.1109/PVSC.2008.4922578.

[3] L.A. Hecktheuer, A. Krenzinger, and C. W. M. Prieb. Methodology for photovoltaic modules characterization and shading effects analysis. *Journal of the Brazilian Society of Mechanical Sciences*, 24(1):26–32, 2002. doi: 10.1590/S0100-73862002000100004.

[4] M. A. De Blas, J. L. Torres, E. Prieto, and A. García. Selecting a suitable model for characterizing photovoltaic devices. *Renewable Energy*, 25(3): 371–380, 2002. doi: 10.1016/S0960-1481(01)00056-8.

[5] A.Q. Malik and S.J.B.H. Damit. Outdoor testing of single crystal silicon solar cells. *Renewable Energy*, 28(9):1433–1445, 2003. doi: 10.1016/S0960-1481(02)00255-0.

[6] F. Granek and T. Zdanowicz. Advanced system for calibration and characterization of solar cells. *Opto Electronics Review*, 12(1):57–67, 2004.

[7] J. Fernández–Reche, I. Cañadas, M. Sánchez, J. Ballestrín, L. Yebra, R. Monterreal, J. Rodríguez, G. García, M. Alonso, and F. Chenlo. PSA Solar furnace: A facility for testing PV cells under concentrated solar radiation. *Solar Energy Materials and Solar Cells*, 90(15):2480–2488, 2006. doi: 10.1016/j.solmat.2006.03.030.

[8] ISO–GUM. *Guide 98–3, Evaluation of measurement data – Part 3: Guide to the expression of uncertainty in measurement*. 2008.

[9] K. Whitfield and C.R. Osterwald. Procedure for determining the uncertainty of photovoltaic module outdoor electrical performance. *Progress in Photovoltaics: Research and Applications*, 9(2):87–102, 2001. doi: 10.1002/pip.356.

[10] *Agilent 34410A/11A 6 1/2 Digit Multimeter User's Manual*. Agilent Technologies, Santa Clara (CA, USA), 4th edition, 2007.

[11] M.G. Kratzenberg, H.G. Beyer, S. Colle, and A. Albertazzi. Uncertainty calculations in pyranometer measurements and applications. In *ASME International Solar Energy Conference*, pages 689–699, Denver (CO, USA), 2006.

[12] *CMA series albedometer and CMP series pyranometer. Instruction Manual*. Zipp & Zonen, Delft (The Netherlands), 2006.

[13] *FP–AI–112 and cFP–AI–112, FieldPoint Operating Instructions*. National Instruments Corporation, Austin (TX, USA), 2004.

[14] *FP–RTD–124 and cFP–RTD–124, FieldPoint Operating Instructions*. National Instruments Corporation, Austin (TX, USA), 2002.

[15] IEC 60751. *Industrial platinum resistance thermometers and platinum temperature sensors*. International Electrotechnical Commission, Geneva (Switzerland), 2nd edition, 2008. ISBN 978-2-8318-9849-0.

[16] K.A. Emery. Measurement and characterization of solar cells and modules. In A. Luque and S. Hegedus, editors, *Handbook of Photovoltaic Science and Engineering*, chapter 16, pages 701–747. Wiley, New York (NY, USA), 2003. ISBN 978-0-471-49196-5.

[17] D.N. Sormaz, J. Arumugam, R.S. Harihara, C. Patel, and N. Neerukonda. Integration of product design, process planning, scheduling, and FMS control using XML data representation. *Robotics and Computer–Integrated Manufacturing*, 26(6):583–595, 2010. doi: 10.1016/j.rcim.2010.07.014.

[18] D. Schorlemmer, F. Euchner, P. Kaestli, J. Saul Joachim, and QuakeML Working Grp. QuakeML: status of the XML–based seismological data exchange format. *Annals of Geophysics*, 54(1):59–65, 2011. doi: 10.4401/ag-4874.

[19] M.E. Poorazizi and A.A. Alesheikh. Monitoring real–time environmental information using Web 2.0 and GIServices technology. *International Journal of Civil Engineering*, 9(1):63–70, 2011.

[20] W. Kolodenny, M. Prorok, T. Zdanowicz, N. Pearsall, and R. Gottschalg. Applying modern informatics technologies to monitoring photovoltaic (PV) modules and systems. In *33rd IEEE Photovoltaic Specialists Conference*, pages 1–5, San Diego (CA, USA), 2008. doi: 10.1109/PVSC.2008.4922829.

[21] M. Prorok, W. Kolodenny, T. Zdanowicz, R. Gottschalg, and D. Stellbogen. PVML – photovoltaic markup language: Toward universal structure for collection and exchange of data acquired during PV monitoring process. In *23rd European Photovoltaic Solar Energy Conference and Exhibition*, pages 3452–3456, Valencia (Spain), 2008. doi: 10.4229/23rdEUPVSEC2008-5BV.2.30.

[22] J.W. Spencer. Fourier series representation of the position of the sun. *Search*, 2(5):172–177, 1971.

[23] J. Michalsky. The astronomical Almanac's algorithm for approximate solar position (1950–2050). *Solar Energy*, 40(3):227–235, 1988. doi: 10.1016/0038-092X(88)90045-X.

[24] M. Blanco–Muriel, D.C. Alarcón–Padilla, T. López–Moratalla, and M. Lara–Coira. Computing the solar vector. *Solar Energy*, 70(5):431–441, 2001. doi: 10.1016/S0038-092X(00)00156-0.

[25] J. Meeus. *Astronomical Algorithms*. Willmann–Bell Inc., 1991. ISBN 978-0-943396-35-4.

[26] I. Reda and A. Andreas. Solar position algorithm for solar radiation applications. Technical Report NREL/TP–560–34302, National Renewable Energy Laboratory (NREL), Golden (CO, USA), 2008.

[27] M. Iqbal. *An Introduction to Solar Radiation*. Academic Press, New York (NY, USA), 1983. ISBN 978-0-12-373752-6.

[28] C.A. Gueymard. The Sun's total and spectral irradiance for solar energy applications and solar radiation models. *Solar Energy*, 76(4):423–453, 2004. doi: 10.1016/j.solener.2003.08.039.

[29] F. Kasten and A. Young. Revised optical air mass tables and approximation formula. *Applied Optics*, 28(22):4735–4738, 1989. doi: 10.1364/AO.28.004735.

[30] R.E. Bird and C. Riordan. Simple solar spectral model for direct and diffuse irradiance on horizontal and tilted planes at the

earth's surface for cloudless atmospheres. *Journal of Climate and Applied Meteorology*, 25(1):87–97, 1986. doi: 10.1175/1520-0450(1986)025<0087:SSSMFD>2.0.CO;2.

[31] B.Y.H. Liu and R.C. Jordan. The interrelationship and characteristic distribution of direct, diffuse and total solar radiation. *Solar Energy*, 4 (3):1–19, 1960. doi: 10.1016/0038-092X(60)90062-1.

[32] A. Woyte, R. Belmans, and J. Nijs. Fluctuations in instantaneous clearness index: Analysis and statistics. *Solar Energy*, 81(2):195–206, 2007. doi: 10.1016/j.solener.2006.03.001.

[33] R. Pérez, P. Ineichen, R. Seals, and A. Zelenka. Making full use of the clearness index for parameterizing hourly insolation conditions. *Solar Energy*, 45(2):111–114, 1990. doi: 10.1016/0038-092X(90)90036-C.

[34] T. Minemoto, Y. Nakada, H. Takahashi, and H. Takakura. Uniqueness verification of solar spectrum index of average photon energy for evaluating outdoor performance of photovoltaic modules. *Solar Energy*, 83 (8):1294–1299, 2009. doi: 10.1016/j.solener.2009.03.004.

[35] IEC 60891. *Procedures for temperature and irradiance corrections to measure I–V characteristics of crystalline silicon photovoltaic devices.* International Electrotechnical Commission, Geneva (Switzerland), 2nd edition, 2009. ISBN 978-2-88910-316-4.

[36] IEC 60904–7. *Photovoltaic devices – Part 7: Computation of the spectral mismatch correction for measurements of photovoltaic devices.* International Electrotechnical Commission, Geneva (Switzerland), 3rd edition, 2008. ISBN 978-2-88910-324-9.

[37] C. Domínguez, I. Antón, and G. Sala. Multijunction solar cell model for translating *I–V* characteristics as a function of irradiance, spectrum, and cell temperature. *Progress in Photovoltaics: Research and Applications*, 18(4):272–284, 2010. doi: 1010.1002/pip.965.

[38] J.C. Patra. Neural network–based model for dual–junction solar cells. *Progress in Photovoltaics: Research and Applications*, 19(1):33–44, 2011. doi: 10.1002/pip.985.

[39] E. Karatepe, M. Boztepe, and M. Colak. Neural network based solar cell model. *Energy Conversion & Management*, 47(9–10):1159–1178, 2006. doi: 10.1016/j.enconman.2005.07.007.

[40] M.C. Di Piazza, M. Pucci, A. Ragusa, and G. Vitale. Analytical versus neural Real–Time simulation of a photovoltaic generator based on a DC–DC converter. *IEEE Transactions on Industry Applications*, 46 (10):2501–2510, 2010. doi: 10.1109/TIA.2010.2072975.

[41] L. Hontoria, J. Aguilera, F. Almonacid, G. Nofuentes, and P. Zufiria. Artificial neural networks applied in PV systems and solar radiation. In S. Kalogirou, editor, *Artificial Intelligence in Energy and Renewable Energy Systems*, chapter 5, pages 163–200. Nova Science Publishers Inc, UK, 2006. ISBN 978-1-60021-261-1.

[42] F. Almonacid, C. Rus, L. Hontoria, M. Fuentes, and G. Nofuentes. Characterisation of Si–crystalline PV modules by artificial neural networks. *Renewable Energy*, 34(4):941–949, 2009. doi: 10.1016/j.renene.2008.06.010.

[43] F. Almonacid, C. Rus, P.J. Pérez, and L. Hontoria. Estimation of the energy of a PV generator using artificial neural network. *Renewable Energy*, 34(12):2743–2750, 2009. doi: 10.1016/j.renene.2009.05.020.

[44] F. Almonacid, C. Rus, L. Hontoria, and F.J. Muñoz. Characterisation of PV CIS module by artificial neural networks. A comparative study with other methods. *Renewable Energy*, 35(5):973–980, 2010. doi: 10.1016/j.renene.2009.11.018.

[45] L.E. Zárate, L.V.B.M. Neto, D.A. Soares, and F.R. Bittencout. Artificial neural networks applied for representation of curves Current–Voltage of photovoltaic modules. In *IEEE International Conference on Industrial Informatics*, pages 1644–1649, Daejeon (Korea), 2008. doi: 10.1109/INDIN.2008.4618367.

[46] T. Minemoto, S. Nagae, and H. Takakura. Impact of spectral irradiance distribution and temperature on the outdoor performance of amorphous Si photovoltaic modules. *Solar Energy Materials & Solar Cells*, 91(10): 919–923, 2007. doi: 10.1016/j.solmat.2007.02.012.

[47] IEC 60904–3. *Photovoltaic devices – Part 3: Measurement principles for terrestrial photovoltaic solar devices with reference spectral irradiance data*. International Electrotechnical Commission, Geneva (Switzerland), 2nd edition, 2008. ISBN 978-2-8318-9705-9.

[48] T. Kohonen. The self–organizing map. *Proceedings of the IEEE*, 78(9): 1464–1480, 1990. doi: 10.1109/5.58325.

[49] M.Z. Boznar and P. Mlakar. Use of neural networks in the field of air pollution modeling. *Air Pollution Modeling and Its Application XV*, pages 375–383, 2002.